6-27-2022 12:00 PM

Automation through Deep-Learning to Quantify Ventilation Defects in Lungs from High-Resolution Isotropic Hyperpolarized 129Xe Magnetic Resonance Imaging

Tuneesh Kaur Ranota, *The University of Western Ontario*

Supervisor: Ouriadov, Alexei, *The University of Western Ontario*
A thesis submitted in partial fulfillment of the requirements for the Master of Engineering Science degree in Biomedical Engineering
© Tuneesh Kaur Ranota 2022

Recommended Citation

Abstract

Obstructive lung diseases are characterized by heterogenous ventilation. Hyperpolarized ^{129}Xe gas lung magnetic resonance imaging (MRI) can examine lung ventilation heterogeneity by acquiring isotropic images. The current gold standard of semi-automated (SA) segmentation can be used to quantify non-isotropic ^{129}Xe lung images to generate ventilation defect percent (VDP), however, this method is not suitable for analysis of isotropic voxel ^{129}Xe images due to the large number of slices. Therefore, we used a fully automated deep learning-based (DL) lung algorithm to calculate VDP from isotropic images. SNR, SA and DL-based VDP were calculated, showing a strong positive linear correlation with a zero intercept and close to unity slope. This study demonstrates the feasibility of using DL-based segmentation methods to quantify ventilation defects, which has potential for clinical translation of ^{129}Xe MRI as a tool for treatment and monitoring for patients with pulmonary diseases.

Keywords

Summary for Lay Audience

Obstructive lung diseases affect millions of individuals and include symptoms such as chronic cough, shortness of breath and frequent respiratory infections. There is currently no cure for many obstructive lung diseases, however, patient treatment focuses on reducing symptoms and hospitalizations, as these diseases place a significant burden on healthcare across Canada. More recent lung diseases such as COVID-19, directly affects the lungs by damaging and destroying its cells. This is similar to other obstructive lung diseases, which result in lungs becoming inflamed and failure of gas exchange and respiratory function, which can lead to organ failure. Spirometry is widely available and is commonly used to diagnose obstructive lung disease, however, it only provides global lung function information.

Medical imaging techniques such as computed tomography (CT) and hyperpolarized gas magnetic resonance imaging (MRI) are used to study pulmonary diseases, as they provide regional lung information which spirometry cannot. Chest CT images can provide structural changes within the lungs, mainly in tissues and airways. Hyperpolarized gas MRI allows for visualization of lung structure as well as function, as it can detect unventilated regions of the lung, known as ventilation defects. Ventilation defects are quantified by the ventilation defect percent (VDP), which is calculated as the total ventilation defect volume (VDV) to the total thoracic cavity volume (TCV). Semi-automated (SA) segmentation methods are typically used for calculating VDP from lung images, however, this technique is difficult for analyzing VDP from isotropic images as it is a time-consuming task. Recently, deep learning (DL) methods have demonstrated numerous successes in medical image analysis tasks.

In this study, we acquired isotropic 3D ^{129}Xe data from participants with ventilation defects and calculated the VDP using a DL-based algorithm in comparison with a SA approach as the reference gold standard. We observed a strong linear correlation between the two types of VDP estimates. This study suggests that ^{129}Xe MRI coupled with the DL-based lung segmentation can be used to rapidly quantify ventilation defects across a wide range of disease.

Co-Authorship Statement

The following thesis contains one manuscript that has been submitted for publication. As the first author of this manuscript, I was a significant contributor to all aspects of the study as well as the manuscript preparation and submission. I was responsible for image analysis, data acquisition, statistical analysis, interpretation of the data, drafting and final approval of the manuscript. Dr. Alexei Ouriadov, as the Principal Investigator and Supervisor, provided continuous guidance and support and was responsible for study conception and experimental design, data analysis and interpretation, MRI acquisition, drafting and approval of final manuscripts. Dr. Grace Parraga and her team were responsible for patient visits, acquisition of MRI and pulmonary function data, and polarization of hyperpolarized gas.

Chapter 2 is an original research article entitled "The Use of 3D Isotropic Hyperpolarized ^{129}Xe Lung MRI for Deep-Learning-Based Automated Quantification of Ventilation Defects and Heterogeneity" and is submitted to the "Journal of Magnetic Resonance Imaging". The manuscript was co-authored by Fumin Guo, Ramtin Babaeipour, Tingting Wu, Matthew S Fox, David G McCormack, Grace Parraga, and Alexei Ouriadov. As first author, I was responsible for data analysis and interpretation, VDP calculation, statistical analysis, and manuscript revisions. Dr. Fumin Guo assisted in the designing and creation of the deep-learning-based algorithm, provided DL-based images, data analysis and manuscript revisions. Ramtin Babaeipour assisted with data analysis and interpretation, and manuscript revisions focused on DL. Tingting Wu assisted in VDP calculations and data interpretations. Dr. Matthew S Fox and Dr. David McCormack assisted in data interpretation and manuscript revisions. Dr. Grace Parraga provided patient pulmonary function data and assisted in manuscript revisions.

The appendix contains one manuscript completed within my MSc that I was first author for, which are complementary, yet not directly related to the objective and hypothesis of this thesis. As first author I was responsible for data acquisition, statistical analysis and manuscript preparation and submission. Appendix A is a peer-reviewed original research article entitled "Feasibility of Dynamic Inhaled Gas MRI-based Measurements using Acceleration Combined with the Stretched Exponential Model" and was originally submitted to the journal *NMR in Biomedicine* on March 19th, 2021 and has been resubmitted to MAGMA on June 4th 2022. The manuscript was co-authored by Dr. Matthew S Fox, Tanya Jaiswal, Elise Woodward, Dr. Marcus Couch, Dr. Tao Li, Dr. Iain Ball and Dr. Alexei Ouriadov.

Acknowledgments

I would first like to thank my supervisor, Dr. Alexei Ouriadov. You have provided me with incredible opportunities throughout my degree that have contributed to my professional and personal growth. I am incredibly grateful for all the support that you have provided me with, you were always approachable and sincere. I appreciate your encouragement and drive that has pushed me to accomplish things that I could not have done alone.

I would also like to thank members of my advisory committee: Dr. Grace Parraga and Dr. Fumin Guo. I appreciate that time that you have taken to provide me with valuable feedback, direction and guidance that has overall strengthened my understanding of my research.

To all the other members of the Medical Physics Lab team members, thank you for your support. To Raman, thank you for having the kindest heart and smile, I knew I could always count on you. To Samuel, thank you for your help and for always being there to put up with my questions. To Lexie, for helping with research tasks and someone I could rely on for support. To Ramtin, thank you for collaborating on my projects and providing insight. Thank you to all my professors at Western who have given me the knowledge needed to complete this degree. Thank you to all my mentors and everything you have taught me throughout this experience.

And finally, a special thank you goes towards my close family and friends. Thank you to my parents for being there for me whenever I needed them. To my sister, Puneet, who I would be lost in life without. You are always someone I can talk or vent to that would understand best. To my childhood friends, Neha, Harjas and Ragavi, thank you for sticking by my side and making my days brighter. Times with you guys are always filled with laughter and fun. To my close friends, Connie and Meghla, I am so lucky to have met you both. Thank you for your positivity, compassion, and encouragement. Thank you to all other individuals who have helped shaped me into the person I am today. I can't put into words how much gratitude I have for you all supporting me not only throughout my degree but also my entire life.

Table of Contents

List of Tables

List of Figures

List of Appendices

List of Abbreviations

^{129}Xe	Xenon-129
^{1}H	Proton
^{3}He	Helium-3
COPD	Chronic Obstructive Pulmonary Disease
CT	Computed Tomography
DL	Deep-Learning
DL_{CO}	Diffusing Capacity of the Lung for Carbon Monoxide
FEV_1	Forced Expiratory Volume in 1 Second
FGRE	Fast-Spoiled Gradient Recalled Echo
FRC	Functional Residual Capacity
FVC	Forced Vital Capacity
HU	Hounsfield Unit
MRI	Magnetic Resonance Imaging
PCR	Polymerase Chain Reaction
RV	Residual Volume
SA	Semi-Automated
SARS-CoV-2	Severe Acute Respiratory Syndrome Coronavirus-2
TE	Echo Time
TR	Repetition time
VDP	Ventilation Defect Percent

CHAPTER 1

1   INTRODUCTION

Hyperpolarized gas magnetic resonance imaging (MRI) produces images that allow for visualization of lung structure and function and can be used to assess characteristics of obstructive pulmonary diseases and calculate the ventilation defect percent (VDP), a sensitive indicator of lung ventilation abnormalities. In this thesis, the development of isotropic ^{129}Xe images and the quantification of ventilation defects in the lungs was investigated.

1.1   Motivation and Rationale

Obstructive lung disease affects individual on a global scale, which include chronic obstructive pulmonary disease (COPD), asthma and cystic fibrosis (CF). Chronic obstructive pulmonary disease (COPD) is a progressive lung disease that is the third leading cause of death worldwide and was responsible for 3.23 million deaths in 2019[1] and 495,000 deaths due to asthma in 2017.[2] Obstructive lung diseases affect the airways of the lungs and can disrupt ventilation and gas exchange processes. More recently, Coronavirus Disease 19 (COVID-19) is a respiratory disease caused by SARS-CoV-2 that has influenced a pandemic of respiratory illness. COVID-19 has affected individuals all around the world with particular severe course in males, patients with cardiovascular comorbidities, and the elderly.[3,4]

Obstructive lung disease places a significant burden on health care across Canada, as COPD is one of the leading causes of hospitalization due to frequent exacerbation.[5] Exacerbation is when symptoms worsen and become more severe, it is also known as a flare-up. In 2010, the Conference Board of Canada estimated that the economic burden of chronic lung diseases was approximately $12 billion, and is estimating a rise of $24.1 billion by 2030.[6] A study found that in Ontario, overall annual cost per moderate COPD exacerbation was approximately $641 and for a severe COPD exacerbation, $9557.[7] It is difficult for physicians to predict whether patients are at risk for exacerbations, which can lead to extended hospital visits, stays and increased risk of mobirdity or death. Obstructive lung diseases are commonly diagnosed and monitored using pulmonary function tests; however, these tests do not allow for aetiological diagnosis or information on defects in the lungs.

COVID-19 has tested Ontario's already burdened health-care system. In 2021, peak periods of positive-testing COVID-19 individuals who were hospitalized (daily) was over 2,300. Due to the new delta-variant, the daily hospitalization rate has increased to over 4,000 in 2022. It has been reported that approx 50% of hospital admissions were COVID-19 related and the number of ICU admissions for COVID-19 was around 76%.[8] Currently, the most common diagnositic method of COVID-19 is through a polymerase chain reaction (PCR) testing of a nasopharyngeal swab, however, it can give false positives. Imaging methods may be used to interpret how the lungs are affected by COVID-19.[9]

Current diagnostic techniques using x-ray computed tomography (CT) are unable to provide sensitive regional heterogeneity of disease progression. For example, for COVID-19, it has been found that approximately 15% of chest CT imaging findings can be normal.[10] However, emerging imaging modalities such as inhaled noble gas magnetic resonance imaging (MRI) can provide sensitive and unique structural and functional information for common obstrucitve lung diseases such as COPD, asthma and CF, but also for newer and emerging diseases such as COVID-19.[11,12] The lungs cannot be visualized with conventional proton MRI due to the low tissue density of the lungs and short signal lifetime. Inhaled hyperpolarized gas MRI has been used to collect regional information from the lungs such as functionality measurements, which can allow for the quantification of ventilation abnormalities. Specifically, the feasibility of hyperpolarized ^{129}Xe MRI provides a way to investigate and assess pulmonary diseases as it allows for visualization of lungs.[13-15]

This chapter provides relevant background knowledge to understand the motivation and rationale of this thesis, lung structure and function and ventilation (1.1). In section 1.2 we will discuss the pathophysiology of obstructive lung diseases in 1.3. The different clinical measurements of lung function (1.4) will be discussed. Imaging measurements of lung structure and function will be introduced in section 1.5. Lastly, the specific hypotheses and objectives of the thesis are introduced (1.6).

1.1.1   Structure and Function of the Lung

The respiratory system primarily facilitates gas exchange processes, as it transports oxygen into the bloodstream and removes carbon dioxide. The structure of the lungs consists of the airways, parenchyma tissue and vasculature.

1.1.2   Airways

The network of airways in adult lungs is where inhaled gas travels, the structure of these airways is shown in Figure 1-1, where the lungs can be divided into the conducting zone and the respiratory zone. Gas first enters in through nasal or oral cavities and makes it way down the trachea, a 4-inch-long tube that divides into two smaller tubes called bronchi, one for each side of the lung. Each bronchus transports gas throughout the lungs and further branches into smaller tubes called bronchioles.   These bronchioles are no longer surrounded by cartilage and begin peripheral airways. Bronchioles continue to branch out into alveolar ducts and eventually alveolar sacs. As we move down the airways, the structures are surrounded by more alveoli, which are small sac structures that begin gas exchange processes.[16]   The alveolar sacs have the smallest diameter but have a large cross-sectional area due to the high number of alveoli, thus maximizing surface area that is available for gas exchange. The majority of the lung volume is taken up by the respiratory zone of the lungs due to the increase in total cross-sectional area.[17]
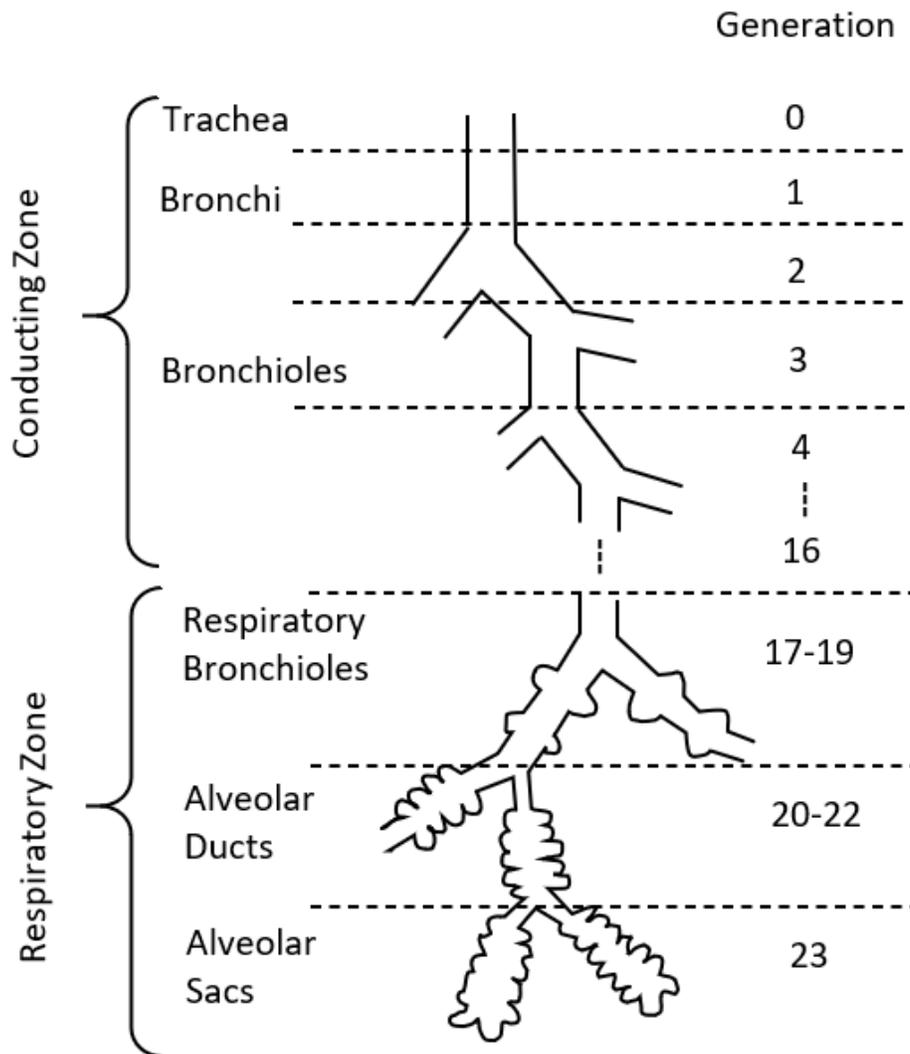
Figure 1-1: Weibel Model of Human Airways.
The generation (Z) of branches from 1 to 16 are part of the conducting zone and the generations branching from 17 to 23 are in the respiratory zone. The conducting zone does not take part in gas exchange because they do not have any alveoli. The respiratory zone is where gas processes occur as alveoli begin to appear on respiratory bronchioles. Adapted from West, JB, Respiratory Physiology: The Essentials (2012).[16]

1.1.3   Ventilation

Ventilation is the circulation and exchange of gases in and out of the alveoli of the lungs through breathing. Inspiration (air entering the lungs) and expiration (air leaving the lungs) depend on differences in pressure in the atmosphere and the lungs. During inspiration, the diaphragm and the external intercostal muscles are used. During inhalation, the diaphragm,

and external intercostal muscles contract, expanding the thoracic cavity. This increase in volume of the thoracic cavity, decreases the pressure and allows for gas into the airways.[18] Exhalation is passive, where energy is not required. It allows for the relaxation of the diaphragm and external intercostal muscles, causing the lungs to recoil and pushes air out. Ventilation and gas exchange processes depend on the airways and obstruction can be caused by various conditions such as COPD and COVID-19.

1.2   Pathophysiology of Obstructive Lung Disease

Chronic respiratory and lung diseases are characterized by airflow limitation in and out of the lungs due to abnormalities in airways. Lung diseases such as COPD vary in terms of disease phenotype, as it can be seen through parenchymal air sac destruction (emphysema) or inflammation in airways leading to chronic cough (chronic bronchitis).[19] Figure 1-2 shows the comparison of a healthy lungs vs COPD lungs. Obstructive lung diseases can progress gradually and can be a result of various risk factors such as tobacco smoke exposure, allergens, unhealthy diet, or air pollution.
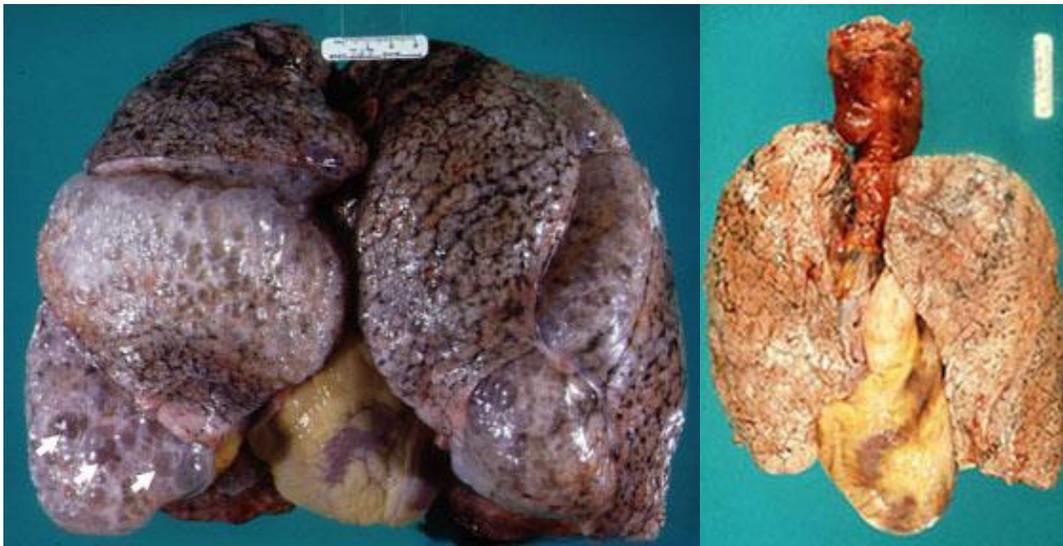
Figure 1-2: Comparison of Healthy Lungs vs COPD Lungs

These two images show lungs of an individual with COPD (left) compared to lungs of a healthy individual (right). We are able to see that both lungs are enlarged and clusters of dilated air spaces in the lower lobes of both lungs. This figure was adapted from http://www.stritch.luc.edu/lumen/MedEd/Radio/curriculum/Medicine/emphysema.htm

1.2.1   Emphysema

Pulmonary emphysema is characterized by the destruction of lung parenchyma, the region of the lungs involved in gas exchange.[20] It encompasses irreversible destruction of lung tissue which results in enlargement of alveolar airspaces, loss of surface area for gas exchange and severe flow limitation.[21] Emphysema can be classified into three types, dependent on lobular anatomy: centrilobular, panlobular and paraseptal emphysema.[22] A comparison between lung tissue histology of normal and emphysema patients can be seen in Figure 1-3.
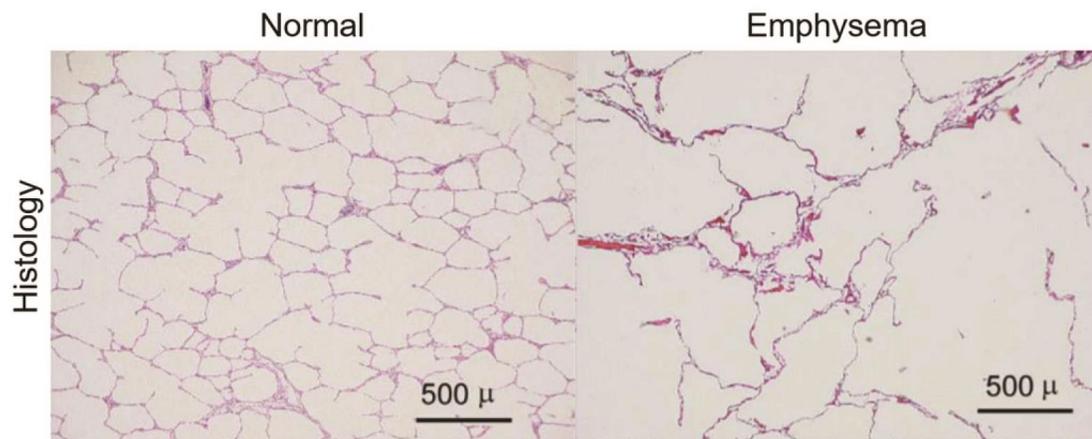
Figure 1-3: Lung Tissue Histology
This panel shows histology slides for normal and COPD patient and scalar bar is 500 µm. This image shows visualization of tissue destruction for patients with emphysema and a reduction in surface area-to-volume ratio. Adapted from Woods et al. 2006 Mag Reson Med.[23] Permission to reproduce provided in Appendix B.

1.2.2   Chronic Bronchitis

Chronic bronchitis is defined as cough and sputum production for at least 3 months of a year for a minimum of a two-year period.[24] The pathological foundation of chronic bronchitis is mucous metaplasia, the overproduction of mucus in response to inflammatory signals.[25] Mucous metaplasia in the small airways lead to worsened airflow obstruction.[26] Studies have connected mucus overproduction and hypersecretion because of cigarette smoke exposure.[27,28]

1.3   Pathophysiology of COVID-19

COVID-19 is a disease that is caused by the most novel coronavirus, which has been named as the severe acute respiratory syndrome coronavirus-2 (SARS-CoV-2) due to its similarities with SARS-CoV. In 2002, SARS-CoV caused acute respiratory distress syndrome (ARDS) and high mortality rates.[29] SARS-CoV-2 primarily affects the respiratory system and includes acute symptoms such as fever, dry cough and dyspnea.[30] The severity of respiratory symptoms from COVID-19 vary from little symptoms to significant hypoxia with ARDS.[31] Individuals can still present symptoms even after infection and recovery from COVID-19 or have ongoing symptoms for many weeks, acute post-COVID symptoms, or months, commonly known as "Long COVID".[32] COVID-19 is frequently spread through respiratory droplets from close face-to-face contact.[9] Epidemiological studies show that mortality rates in elderly populations are much higher than for children.[33] In severe cases, thrombosis and pulmonary embolism may occur in addition to respiratory symptoms. The endothelium is an important function in thrombotic regulation, as it promotes vasodilation, fibrinolysis, and anti-aggregation.[30,34] Endothelial cells represent one third of lung cells and patients with severe disease are likely to indicate significant endothelial injury, which can facilitate viral invasion.[30]

1.4 Clinical Measurements of Lung Function

To diagnose, assess and monitor lung disease, pulmonary function testing (PFT) is used as a gold standard. These tests provide information about lung health and function and can be used to quantify the progression of disease. Pulmonary function tests include spirometry, plethysmography, and the diffusing capacity of the lung for carbon monoxide (DL_{co}). Pulmonary function tests can be expressed as a percent predicted (%pred), which are based on the patient's age, sex, height, and ethnicity.[35]

1.4.1 Spirometry

Spirometry is a simple and common pulmonary function test that can be performed using a handheld device shown in Figure 1-4. The patient is asked to perform multiple normal breaths at the mouthpiece then to inhale until they reach total lung capacity (TLC).[36] Then, they are asked to forcefully perform exhalation until no more air can be expelled. The volume of air the patient expels from TLC in 1 second allows for the forced expiratory volume in one second (FEV_1) to be calculated, as seen in Figure 1-5. The forced vital capacity (FVC) is also calculated as this is the total volume of air that an individual expires from TLC. The FEV_1/FVC ratio is a measure of airflow obstruction.[17]

Figure 1-4 Pulmonary Function Testing Devices
Above are two devices used for PFT: a handheld spirometer (left) and whole body
plethsmograph (right).

1.4.2   Plethsmography

Plethysmography calculates lung volumes such as functional residual capacity (FRC),
residual volume (RV) and total lung capacity (TLC) using Boyle's Law,[37] and a
plethysmograph is shown in Figure 1-4. The patient is asked to perform breathing
procedures such as forced inspiration and forced expiration. The volume and temperature
of the sealed chamber is constant and the volume changes are estimated based on pressure
changes.[38] FRC is the volume present in the lungs after normal exhalation, RV is the
volume of air present in the lungs after maximum exhalation and TLC is the maximum
volume reached by the lungs at full inspiration.
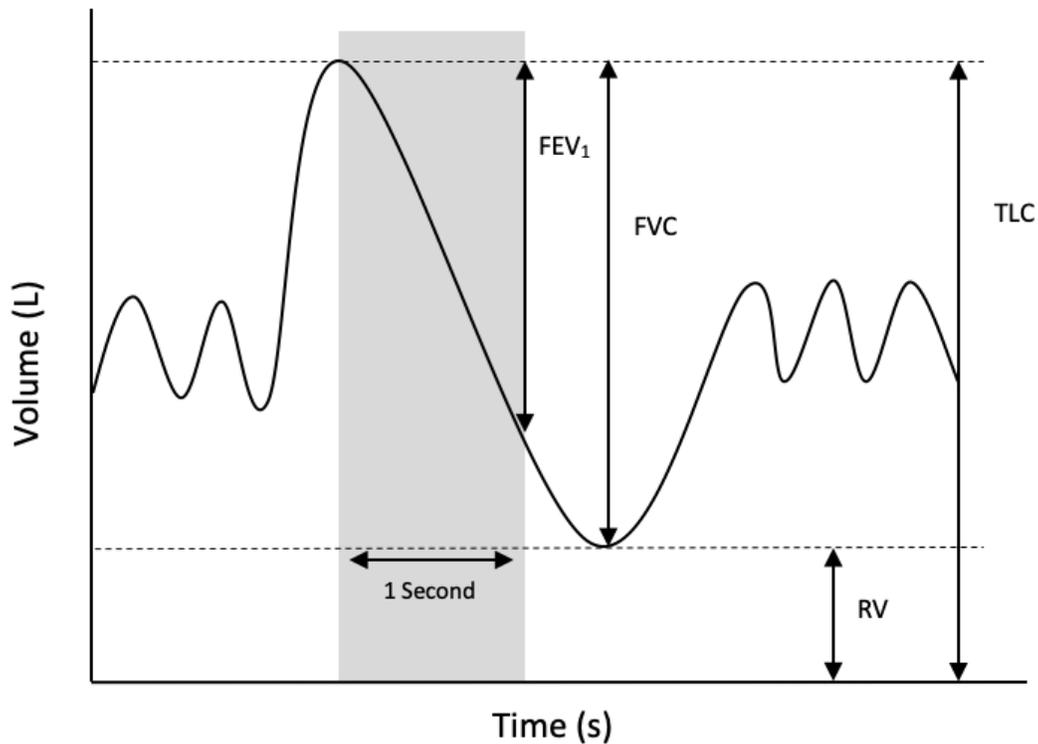
Figure 1-5: Graph of Lung Volume Measurements.
These measurements are seen during tidal breathing and show the forced expiratory volume in 1 second (FEV$_1$), the forced vital capacity (FVC), residual volume (RV) and total lung capacity (TLC).

1.4.3   Diffusing Capacity of the Lung

The diffusing capacity of the lung for carbon monoxide (DL$_{co}$) determines the lungs' ability to diffuse oxygen into the bloodstream and can be used to investigate the gas exchange of the alveoli for patients with emphysema.[39,40] Inhaled CO has high affinity for hemoglobin when compared to oxygen. The patient is asked to inhale a gas mixture of 0.3% carbon monoxide, hold their breath for approximately 10 seconds, then exhale. During the breath-hold, the CO diffuses into the bloodstream. The difference between CO concentration of the exhaled gas and inhaled gas is used to determine the amount of CO diffused into the blood.[41] Patients with emphysema will show lower DL$_{co}$ values due to alveolar destruction and limited surface area for gas exchange.

1.5   Imaging Measurements of Lung Structure and Function

Pulmonary imaging provides structural and functional information of the lungs and the ability to view regional areas of the lungs that may be affected by disease. In this thesis we will discuss methods of x-ray imaging, computed tomography (CT), proton magnetic resonance imaging (MRI) and hyperpolarized gas MRI.

X-ray Imaging

The most common imaging modality for chest imaging is plain radiograph or planar x-ray. Plain x-rays are medical images that are created through radiation which is absorbed by different structures or parts in the body. High-density structures such as bone, absorb higher percentage of the x-ray beam thus appearing light grey, whereas low-density structures appear dark grey because they absorb a small percent.[42] This allows for a two-dimensional image of structures, such as Figure 1-6. The benefits of x-rays are that they are widely available, provide good image resolution and can be useful for diagnosing injuries such as fractures, blockages, and collapsed lungs.[42]
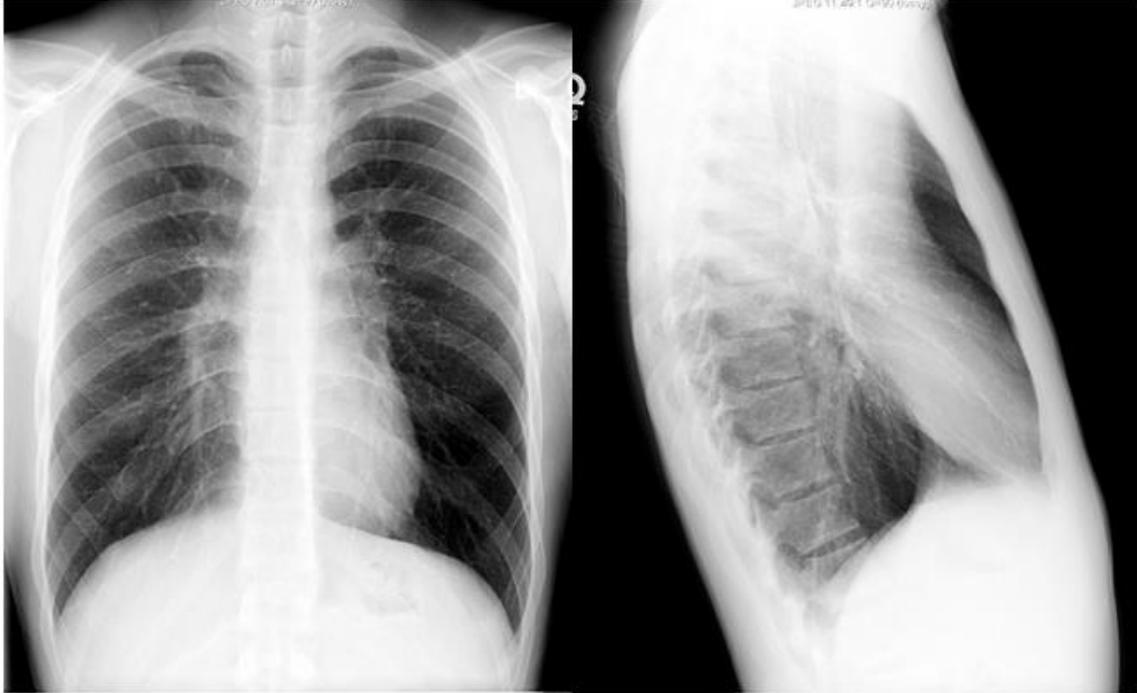
Figure 1-6: Chest X-Ray of Patient with COPD
These two X-Ray images shows hyperinflation, a common occurrence in asthma, emphysema, and chronic bronchitis. This image was adapted from
http://www.stritch.luc.edu/lumen/MedEd/Radio/curriculum/Medicine/emphysema.htm.

Computed Tomography

CT has been widely used since the 1970s for imaging pulmonary diseases. Thoracic CT can be acquired under breath hold conditions and can provide a three-dimensional volume from collection of multiple x-ray images at difference angles. Tissue density can be measured using Hounsfield units (HU), where -1000 HU indicates presence of air (possible tissue destruction), and 0 HU indicates presence of water. Most tissues have HU between 20 and 100. These measurements can be used to measure emphysema which has low density of lung tissue; thus, the most common threshold of -950 HU is used to identify destruction of tissue.[43] These measurements can provide quantification on the extent of emphysema in the lungs.

CT imaging provides much higher resolution and contrast images than planar x-ray. This allows for the visualization of tissue that may be affected by lung disease, as shown in Figure 1-7. The ability to quantify and measure parts of the lung is an important tool for the diagnosis and monitoring of lung disease. Studies have used quantitative CT analysis to investigate COPD[44,45], thus becoming an important application in clinical settings.[46] A limitation of using CT imaging is the radiation dose required, which raises concerns about using CT imaging for longitudinal monitoring. In addition, for COVID-19, chest CT imaging findings are not specific as they overlap with other infections, thus limiting the diagnostic value for COVID-19. Studies have found that some patients admitted to the hospital with confirmed SARS-CoV-2 infection display normal CT imaging findings.[47,48] In response to these limitations, the field has taken an interest in magnetic resonance imaging (MRI) and using MRI for lung imaging, which can provide different or complementary information to CT.
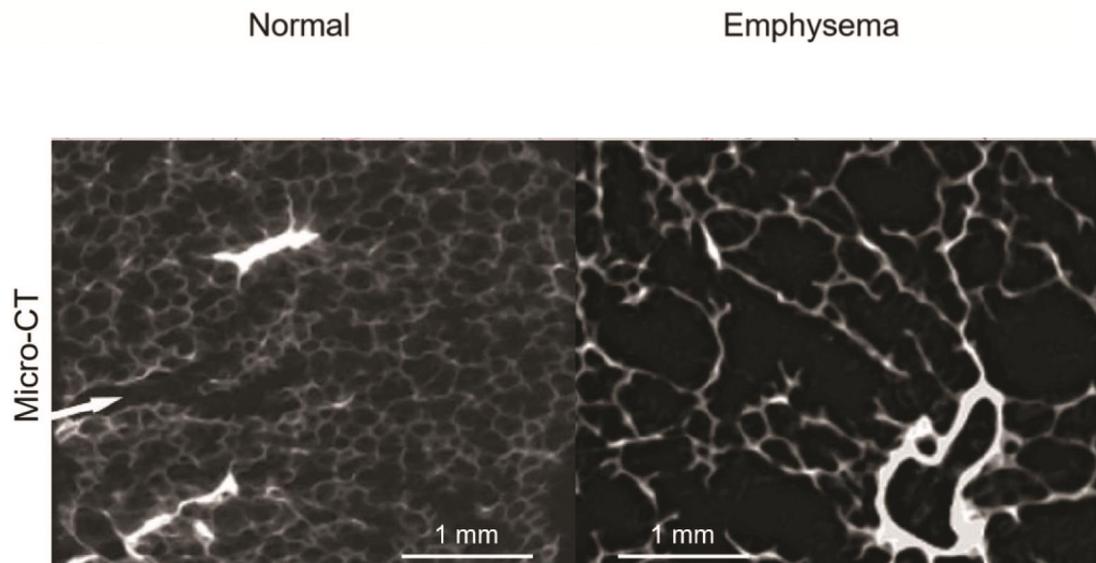
Figure 1-7: Lung Tissue Histology and Micro-CT Images
The panel shows micro-CT images for normal and emphysematous tissue with scalar bar 1mm. The normal lung parenchyma (left) shows a respiratory bronchiole dividing into two alveolar ducts, the emphysema image (right) shows destruction of the lung parenchyma as alveoli are enlarged. Image adapted from Watz et al. 2005 Radiology.[49] Permission to reproduce provided in Appendix B.

Proton Magnetic Resonance Imaging

CT can provide structural measurements of the lungs, however, the radiation dose to patients is the main limitation of its use. Magnetic Resonance Imaging (MRI) is a powerful non-invasive imaging technique that uses strong magnets to produce three dimensional images of organs in the body. The magnets produce a magnetic field where half-integer spins (for example, hydrogen, or simply protons, which are a part of many human body molecules have spin ½) can align. Radiofrequency (RF) current stimulates the protons, and they pull away from the magnetic field. When the RF is turned off, the protons realign with the magnetic field and MRI sensors are able to capture images by detecting the energy released by the protons.[50] Acquiring proton lung images can be challenging due to rapid signal decay following the RF pulse due to the B_0 field inhomogeneity caused by the many solid-liquid-gas interfaces leading to significant image SNR degradation. However, techniques such as ultra-short echo time (UTE)[51,52] have been developed to achieve similar CT structural information. MRI allows for lung imaging without the use of radiation, but the low tissue density of the lung presents as a challenge. In healthy lungs, the tissue density is approximately tenfold lower than adjacent tissues, such as the trachea, and MR signal is directly proportional to tissue proton density, thus MR signals of the lungs are ten-times weaker.[53] It is difficult to acquire images with adequate signal when there is tissue destruction and less tissue due to certain lung diseases. Proton lung MR imaging is demonstrated in Figure 1-8.

Figure 1-8: Coronal View of the Non-Isotropic ^{1}H MRI Slice
Image shows a non-isotropic, 3x3x15mm^3 slice captured by proton MR imaging.

Hyperpolarized Gas Magnetic Resonance Imaging

To overcome the limitations of proton MRI, hyperpolarized gas allows for the visualization of functional lung regions through the inhalation of polarized gas. Gases such as helium-3 (^{3}He) and xenon-129 (^{129}Xe) are stable isotopes that can be hyperpolarized using the spin exchange optical pumping method[54] and increase net magnetization, thus increasing MR signal and signal-to-noise ratio (SNR).[51,52] These hyperpolarized gas images can be acquired during a single breath-hold and are well tolerated by patients with lung disease.[55-58] Hyperpolarized gas imaging initially began in the early 1990s, where ^{129}Xe was used in mouse lungs.[59] This evolved to be used in human studies and then switched to ^{3}He imaging; both gases have been shown to be safe.[55,56,60] The use of ^{3}He provides greater signal-to-noise ratio in imaging, however, the field switched back to ^{129}Xe due to the high abundance and lower cost compared to ^{3}He.[51]

15

Hyperpolarized gas MRI imitates the movement of air into the lungs from the use of inhalation of polarized gas. This imaging captures the gas inhaled by the patient opposed to the lung tissue, which allows for the visualization of functional lung regions. Figure 1-9 shows representative ^{1}H and ^{129}Xe and CT lung images. To acquire the images, a single breath-hold method is used, where a patient inhales a 1.0L volume of gas (a mixture of 50% hyperpolarized noble gas (^{3}He or ^{129}Xe) and 50% Helium-4 gas) and holds their breath for 10 to 16 seconds as the images are captured.[61] The inhaled gas mixture will be distributed to all ventilated regions of the lungs; thus imaging will capture bright areas for regions filled with gas and dark areas which represent poorly ventilated regions or areas with ventilation defects.[56] Currently, companies such as Polarean Imaging plc, NC, USA,[62] are able to provide high quantity xenon-129 polarizers and have received approval to be used in clinical studies.[63]
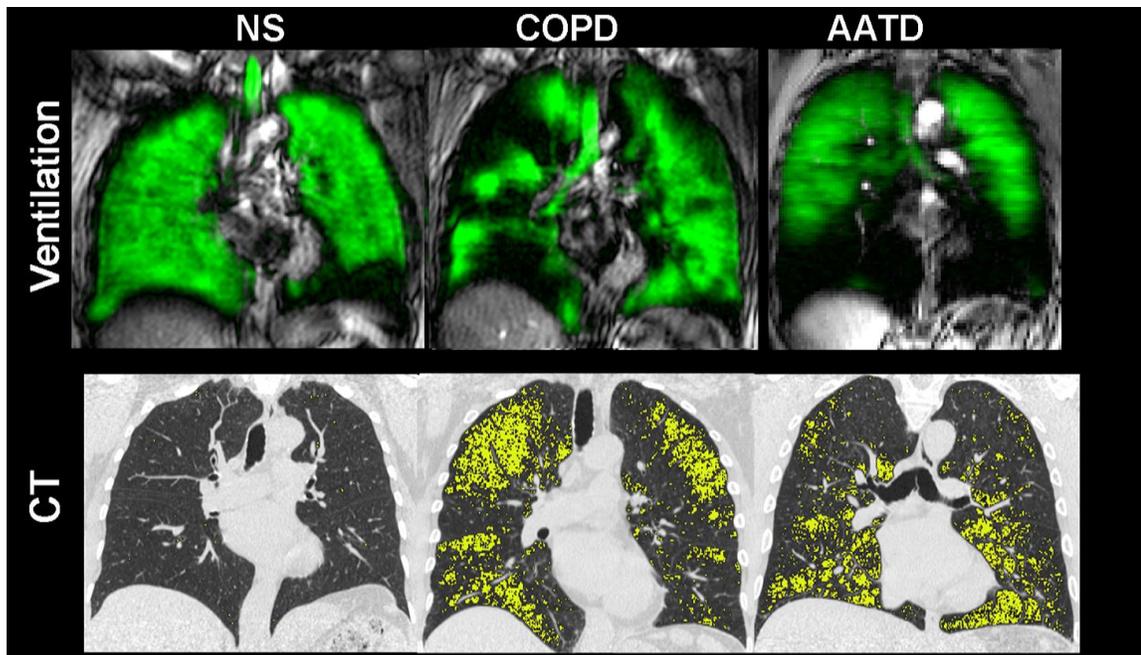
Figure 1-9: Representative CT and ^{1}H MRI and ^{129}Xe MRI Lung Images

Figure top panel (ventilation) shows overlapping ^{1}H MRI and ^{129}Xe MRI lung images (green) showing the regions where ventilation of inhaled gas occurs, and darker regions indicate the unventilated areas . Figure bottom panel (CT) shows CT images with areas oh -950HU (yellow), indicating areas of dead tissue and possible emphysema. NS=Elderly never-smoker, FEV_1=105%$_{pred}$, DL_{CO}=94%$_{pred}$, RA_{950}=0.14%, VDP=3.92%; COPD=Ex-smoker with COPD, FEV_1=59%$_{pred}$, DL_{CO}=43%$_{pred,}$ RA_{950}=12%, VDP=15%; AATD=alpha-one antitrypsin deficiency, FEV_1=58%$_{pred}$, DL_{CO}=50%$_{pred}$, RA_{950}=19%, VDP=27%. Figure adapted from Westcott et al. (2019).[61] Permission to reproduce granted by supervisor (co-author).

There are many methods for hyperpolarized gas MRI segmentations in the field. For example, a study compared differences between histogram-based and image-based algorithms for segmentation of hyperpolarized gas lung images. Image-based convolutional neural networks were used and allowed mitigation of issues presented in histogram-bases segmentation such as loss of important spatial information.[64] Additionally, a study compared two quantification methods for ^{129}Xe ventilation MRI: histogram rescaling and binning approach with the K-means algorithm. This study showed VDP values for both methods to be in close agreement, however, they did not agree closely for higher ventilation bins and determining a preferred method is challenging.[65] Many studies focus on quantifying the ventilation defect percent (VDP), however one study focused on investigating pulmonary ventilation distribution. It combines image histogram characterization and linear binning maps to map and quantify pulmonary ventilation. This allowed for a more comprehensive analysis on ventilation distribution and to detect ventilation abnormalities under various conditions.[66]

To quantify ventilation abnormalities, a semi-automated[67] and fully automated deep learning-based approach was used. Both segmentation methods co-registered the ventilation images to the anatomical proton image. For semi-automated segmentation, a k-means clustering algorithm is used to divide the ventilation of the lungs into five clusters. The clusters ranged from 1 to 5, gradually increasing in signal intensity, from no signal (cluster 1), hypointense signal (cluster 2) to hyperintense signal (cluster 5).[67] Cluster 1 was used to identify ventilation defects as the lowest ventilation cluster and corresponds to the background signal intensity. For the deep-learning based method, a 3D k-means clustering

method was used to cluster all the slices at the same time and save the cluster map in a file to visualize images. With semi-automation, the first step is to manually segment the xenon MRI images to remove major airways (Figure 1-10). The deep-learning-based method gets rid of these major airways automatically using a trained network. The second step for semi-automation involves doing the same segmentation to proton images, then manually selecting landmarks across the lungs (Figure 1-10). The deep-learning algorithm is able to do this step automatically for each patient. These landmarks aid in step 3, where overlapping of both segmented images occurs (Figure 1-10). For the deep-learning-based method, a *NiftyReg* package (http://cmictig.cs.ucl.ac.uk/wiki/index.php/NiftyReg) allowed for registration of the ^{1}H MR images on the ^{129}Xe volumes, creating lung masks. *NiftyReg* allows for rigid, affine, and non-linear registrations of 3D images. The k-means clustering method is applied to calculate VDP, which remains similar for both semi and fully automated techniques. Overall, the deep-learning based method has automated several parts of the semi-automated method.
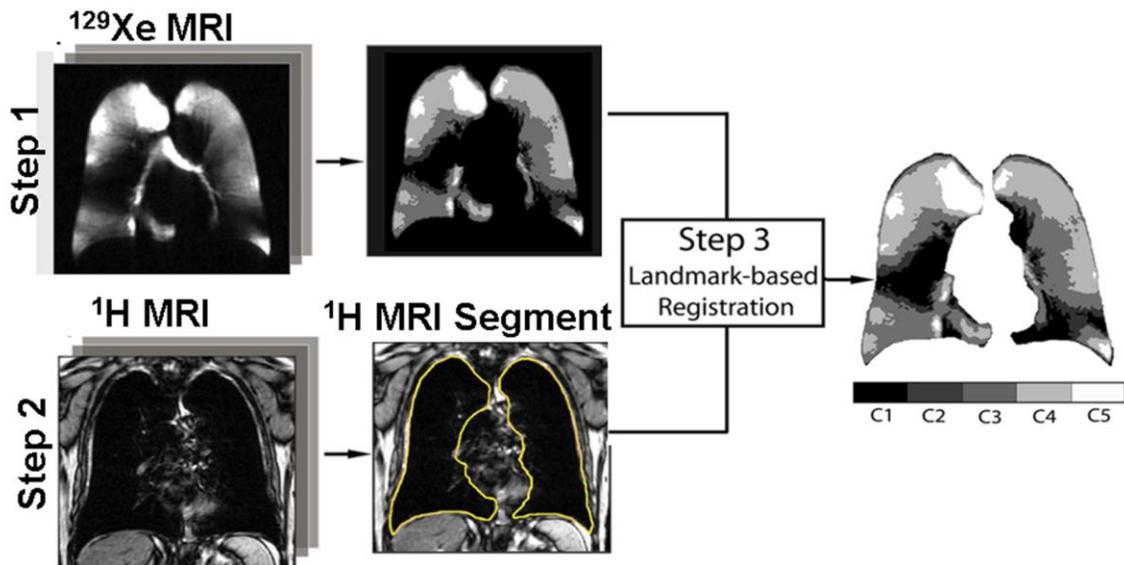
Figure 1-10 K-means Clustering Classification Method
A three-step methodology for semi-automated segmentation of hyperpolarized xenon-129. ^{129}Xe MRI manual segmentation (step 1) and ^{1}H MRI images manual segmentation (step 2) and then overlap the images using landmarks (step 3) to visualize ventilation defects. Image adapted from Kirby et al. (2012).[67] Permission to reproduce provided in Appendix B.

The ventilation defect percent (VDP) is used to quantify defects in the whole lung and is calculated as the total ventilation defect volume (VDV) to the total thoracic cavity volume (TCV) as shown in Equation 1 below.[56] VDV is the total volume of voxels calculated from the proton image (lung cavity).

$$VDP = \left(\frac{VDV}{TCV}\right) \times 100\% \qquad [1]$$

This measurement has been used for quantification of ventilation defects for patients with asthma[68] and COPD.[69] Currently, the aetiology and clinical understanding of ventilation defects is very limited and requires further research.[70] However, hyperpolarized MRI has been useful for indication of treatment response in obstructive lung disease.[71,72] Although hyperpolarized gas is a promising measure for quantification of lung structure and function, it is limited due to high costs, specialized equipment and hardware and clinical approval.

Overall, various imaging techniques provide their own advantages and disadvantageous. However, they provide important functional information of the lungs, which allow for a deeper understanding of ventilation defects and abnormalities.

1.6   Thesis Objectives and Hypotheses

The first objective of this thesis is to generate isotropic 3D static-ventilation lung images from hyperpolarized noble xenon-129 gas MRI. To do this, we obtained both traditional anisotropic (voxel size = 3x3x15mm^3) and isotropic (voxel size = 3x3x3mm^3) 3D ^{129}Xe data from a single 16 second breath-hold using interpolation with signal-free k-space data. The second objective of this thesis is to evaluate the use of a fully automated DL-based lung segmentation to quantify abnormal ventilation. To do this, we created a fully automated deep-learning based network and compared the VDP values to the semi-automated-based VDP values. We hypothesize that DL-based algorithms can be used for

calculation of the VDP estimates from isotropic-voxel ^{129}Xe lung images and can provide precise assessment of abnormal ventilation in the lungs.

CHAPTER 2

2 DEEP-LEARNING-BASED AUTOMATED QUANTIFICATION OF 3D ISOTROPIC HYPERPOLARIZED ^{129}XE LUNG MRI VENTILATION DEFECTS

2.1 Introduction

Hyperpolarized ^{129}Xe MRI is an established research tool pending the final stage of the Food and Drug Administration (FDA) approval that has provided sensitive and unique structural and functional information in the lungs for observation and therapy guidance/assessment for patients with pulmonary diseases such as chronic obstructive pulmonary disease (COPD),[11,12] asthma,[73] and Cystic Fibrosis.[74,75] A number of recent studies have demonstrated that improved ^{129}Xe polarization techniques have allowed for high spatial and temporal resolution pulmonary images[12,76] which can be used for the quantification of ventilation abnormalities as the ventilation defect percent[72] (VDP) in patients with pulmonary diseases such as COPD and asthma.

Recently, a new emerging respiratory disease caused by SARS-CoV-2, Coronavirus Disease 19 (COVID-19),[30,77] has influenced a pandemic of respiratory illness all around the world with particular severe course in the elderly population.[4] Symptoms of COVID-19 infection involve the upper respiratory tract and can vary from mild, such as the common cold, to severe, such as pneumonia.[78] A recent study highlighted the importance of using xenon MRI to evaluate pulmonary function damage and microstructural parameters in COVID-19 patients, by finding higher rates of ventilation defect percent (VDP) compared with healthy individuals.[79] In addition, studies have used hyperpolarized xenon-129 to identify long-term symptoms following COVID-19 infection which computed tomography (CT) scans were unable to detect.[80] One study used ^{129}Xe MRI to detect COVID-19-related chronic pulmonary injury and found results which indicate compromised gas exchange in the lungs, providing explanation for patient symptoms that could not be explained by other

imaging techniques.[81] Another study found objective impairment in gas transfer in the lungs of COVID-19 patients with normal CT scans using ^{129}Xe MRI.[82] These studies conclude that the use of ^{129}Xe MRI in COVID studies will allow for an increased understanding of the causes and diagnosis of symptoms after COVID-19, as it provides evidence of lung abnormalities that are not detected with conventional imaging.[81,82] Furthermore, studies are continuing to investigate the extent and consequences of long-term symptoms of COVID-19 through the use of ^{129}Xe MRI to mitigate lung disease progression.[83]

Many studies quantifying ventilation defects in patients with pulmonary disease by calculating VDP have predominately used non-isotropic voxel scans (voxel size = 5x5x15cm^3) ^{129}Xe MRI datasets.[12,56,61] The development of isotropic voxel ^{129}Xe imaging faces a number of obstacles such as insufficient (<5[84] Signal-to Noise Ratio (SNR),[68,85] which do not allow for an accurate generation of the VDP estimates [86] and MRI scan time. Another limitation is due to the relatively short breath-hold durations, which are needed to acquire the 3D isotropic-voxel ^{129}Xe MRI static ventilation images. The ^{129}Xe MRI modality has been found to be well tolerated by patients with lung diseases in general,[55-58] but the breath-hold should be limited to approximately to 16-seconds. This allows for the acquisition of sixteen 15mm slices collecting the non-isotropic voxel static ventilation images. Isotropic datasets include approximately 80 slices, thus requiring 80-seconds of breath-hold which is not physically possible from patients. Other methods besides breath-hold that mitigate breathing motion artefacts include parallel imaging and compressed sensing. We do not possess the specific hardware required for parallel imaging and compressed sensing would require an acceleration factor of 5, which will not allow for the reconstruction of isotropic data. For proton lung imaging we can use free breathing and respiratory gating methods, however these are not feasible for hyperpolarized gas MRI.

Efforts have been made to overcome the non-isotropic voxel problem, where isotropic-voxel 3D ^{129}Xe static-ventilation images were collected in a single 16sec breath-hold from asthma subjects using Fast Gradient Recalled Echo (FGRE).[68,86-88] Isotropic ^{129}Xe imaging

is important as it should permit more accurate assessment of disease-progression, estimation of the treatment effect, and improvement of our understanding of ventilation defects and abnormalities.

The quantification of the isotropic-voxel datasets can be challenging for several reasons. Presently used semi-automated segmentation[67] permits to quantify 3D non-isotropic [129]Xe lung images to generate the ventilation-defect-percent estimates. Previous methods to quantify ventilation abnormalities include manual and semi-automated segmentation[67], the latter being the current gold standard. Algorithms to segment thoracic cavity images include seeded region-growing, [67] clustering, [89] and model-based techniques.[90] However, this method is not optimal for isotropic-voxel 3D [129]Xe MRI analysis, due to the requirement for user input, which is not feasible for the large number of slices (~80), thus creating a very time-consuming task. Deep learning (DL) is a subset of machine learning and is a way to mimic human neurons. It is based on optimization algorithms and artificial neural networks that mirrors the way humans think and learn. Neural networks include multiple layers of nodes which create a Deep Neutral Network architecture that is very similar to the human brain. Two main factors that affect the power of DL models are data and the computing power. In recent years with the advancements in available data, computational power of computers, and graphic processors, DL has improved by a result of deeper neural networks. DL-based methods utilizing convolutional neural networks (CNNs) have become widespread in numerous medical imaging applications, including image segmentation.[91] The main goal behind CNNs is to learn the feature maps of an image and use them for image classification. But in image segmentation, the goal is to reconstruct an image from the feature map and to assign a classification to every pixel.

Recently, deep learning (DL) methods have demonstrated numerous successes in medical image analysis tasks[92] due to their efficiency and accuracy, such as brain tumor segmentation,[93] lung segmentation in CT images,[94] breast cancer radiotherapy[95] and lung segmentation for tracking potential pulmonary perfusion biomarkers in COPD.[96] Segmentation models based on convolutional neural networks,[97] U-Net[98] and U-Net++,[14]

show potential to be used for VDP calculation. U-Net++ was introduced to overcome some problems of U-Net, such as the unknown optimal depth of encoder-decoder in each specific task and the restrictive design of skip connections. In this network, the main encoder and decoder architecture are maintained with the addition of some up-sampling and skip connections in between to introduce a U-Net of varying depths. The main idea behind redesigned skip connection was to reduce the semantic gap between the contracting and expanding pathway to ease the optimization. Moreover, the concept of deep supervision is added to the U-Net++, so that the model complexity can be adjusted to create a balance between speed and performance.

The use of deep learning methods with convolutional neural networks (CNN) has greatly impacted pulmonary functional imaging by improving functional imaging quality, decreasing acquisition time and improve image segmentation and reconstruction.[99-101] Studies have used machine-learning algorithms in hyperpolarized gas MRI to predict lung ventilation heterogeneity in COPD patients[102] and to reconstruct human lung gas MRI from k-space data.[101] We hypothesize that DL-based algorithms can be used for accurate generation of the VDP estimates from isotropic voxel size images and can provide accurate assessment of lung structure and function. In this study, we acquired 3D ^{129}Xe static-ventilation data from ten COVID-19 survivors assuming that this lung disease causes ventilation defects.[103] The isotropic voxel datasets were acquired by using a interpolation with signal-free k-space data method.[85] The VDP estimates from the isotropic voxel data were generated using a DL-based algorithm in comparison with a semi-automated approach[67] as the reference gold standard and/or ground truth.

2.2   Materials and Methods

Study Participants

Ten COVID-19 Survivors (CS) and established ventilation heterogeneity were enrolled and provided written informed consent provided to an ethics board approved study protocol.

Pulmonary Function Tests

Spirometry, plethysmography, and the diffusing-capacity-of-the-lung-for-carbon-monoxide (DL_{co}) were performed according to American Thoracic Society (ATS) guidelines[36] using a plethysmograph and attached gas analyzer (MedGraphics Corporation. St. Paul, MN USA) to obtain the FEV_1, forced vital capacity, residual volume, and total lung capacity.

^{129}Xe and ^{1}He MRI Acquisition

^{129}Xe MR imaging was performed at 3.0T (MR750, GEHC, WI) using whole-body-gradients (G_{max}=5 G/cm, slew rate=200 mTm^{-1}s^{-1}), as previously described,[104] and a commercial ^{129}Xe quadrature-flex RF coil (MR Solutions, USA). The ^{129}Xe gas was polarized to 35% and was obtained from a turn-key, spin-exchange polarizer system (Polarean-9810 ^{129}Xe-polarizer, Polarean Inc, USA).[105] All subjects inhaled 1L of a 30/70 by volume ^{129}Xe/^{4}He mixture from functional residual capacity (FRC) during a 16 second breath-hold. Non-isotropic voxel xenon-static-ventilation images were acquired using a coronal-plane 3D FGRE sequence, TE/TR=1.5ms/5.1ms, reconstructed matrix size=128x128x16, initial flip angle=1.3^o, FOV=40x40x24cm^3, and voxel-size=3x3x15mm^3, as previously described.[72]

To acquire the isotropic datasets with 80 slices, we used interpolation with signal-free k-space data. It can be very useful for cases when one needs to acquire an isotropic 3D dataset during limited scan time, as in the case of hyperpolarized gas lung MRI, which is normally conducted during a 16sec breath-hold. Presently, the traditional anisotropic voxel (3x3x15mm^3) ^{129}Xe lung MRI can be acquired in 12 seconds, thus one needs a 60sec breath-hold to acquire the isotropic voxel (3x3x3mm^3) 3D dataset, which is not physically possible. This technique is done by zero filling and applying 3D Fast Fourier

Transform (FFT) starting with the z-direction to obtain the 3D isotropic voxel ^{129}Xe lung images with 3x3x3mm^3 voxel-size.[106] ^{1}H MRI (multi-slice 2D FGRE, TE/TR=1.0ms/4.7ms, reconstructed matrix size=128x128x16, flip angle=10°, FOV=40x40x24cm^3, and voxel-size=3x3x15mm^3) was performed before ^{129}Xe MR imaging and images were acquired from subjects inhaling 1L of ultra-high purity medical grade nitrogen 2 (N$_2$) (Messer Canada Inc) during a 16 second breath-hold. A whole-body RF coil was used and ^{1}H fast spoiled gradient-recalled echo sequence as previously described.[69] 2D multi-slice ^{1}H MRI data was transformed to the 3D k-space dataset, and then used interpolation with signal-free k-space data to generate the isotropic voxel proton images with 3x3x3mm^3 voxel size, similar to the ^{129}Xe case.

2.2.1   Image Analysis

SNR Calculations

^{129}Xe SNR was calculated for three central slices in a coronal-view, using a 15x15 voxel square region of interest inside a lung region of homogeneous signal and using the same 15x15 voxel square region of interest outside the lung in an area of no lung signal.[13]

VDP Calculation using a Semi-Automated method

Ventilation defects were identified using a k-means clustering approach, and both semi-automated and fully automated deep learning-based VDP was calculated as the total ventilation defect volume normalized to the thoracic cavity volume. For semi-automated segmentation, a k-means clustering algorithm previously described was used for SA VDP calculations.[67,88] Two trained observers calculated the SA-based VDP calculations, taking approximately 45-mins to 1-hour for each patient (80 slices each).   Thus, taking approximately 10 hours per observer to obtain SA VDP values.

In this research, we used a semantic segmentation task to segment the ^{1}H MR images.[107] Semantic segmentation is the task of labeling each pixel of an image with a class. In our research we had two classes: 1- pixels belonging to the lung 2- pixels that do not belong to the lung area. U-Net is a commonly used DL segmentation network which allows for fast and precise segmentation of images and has outperformed previous convolutional networks.[97] In this work, we used an adaptation of U-Net (Figure 2-2a) named U-Net++[14] (Figure 2-2b). This network was composed of two pathways. First, an encoder down-sampled the input images of proton lung MR images while extracting the features using convolution and pooling layers. The goal here was to capture the context of the input image, in our research, this step extracts features of proton lung MR images to recognize these images. Secondly, a decoder up-sampled the information from the encoder which resulted in an accurate localization. Meanwhile, the isotropic contextual information from the encoder was passed to the decoder via skip connection to help with localization. Skip connections allow the network to retrieve spatial information that may have been lost from the down-sampling path. Finally, the contextual information from the encoder path was combined with the localization in the decoder to restore the size of the image and produce the segmented ground truth. The output images produced are the segmented lung masks of the proton MR images, shown in Figure 2-3. In U-Net++, the redesigned skip connections are added to reduce the semantic gap between the contracting and expanding pathway compared to the original U-Net architecture, thus being more favourable to use.
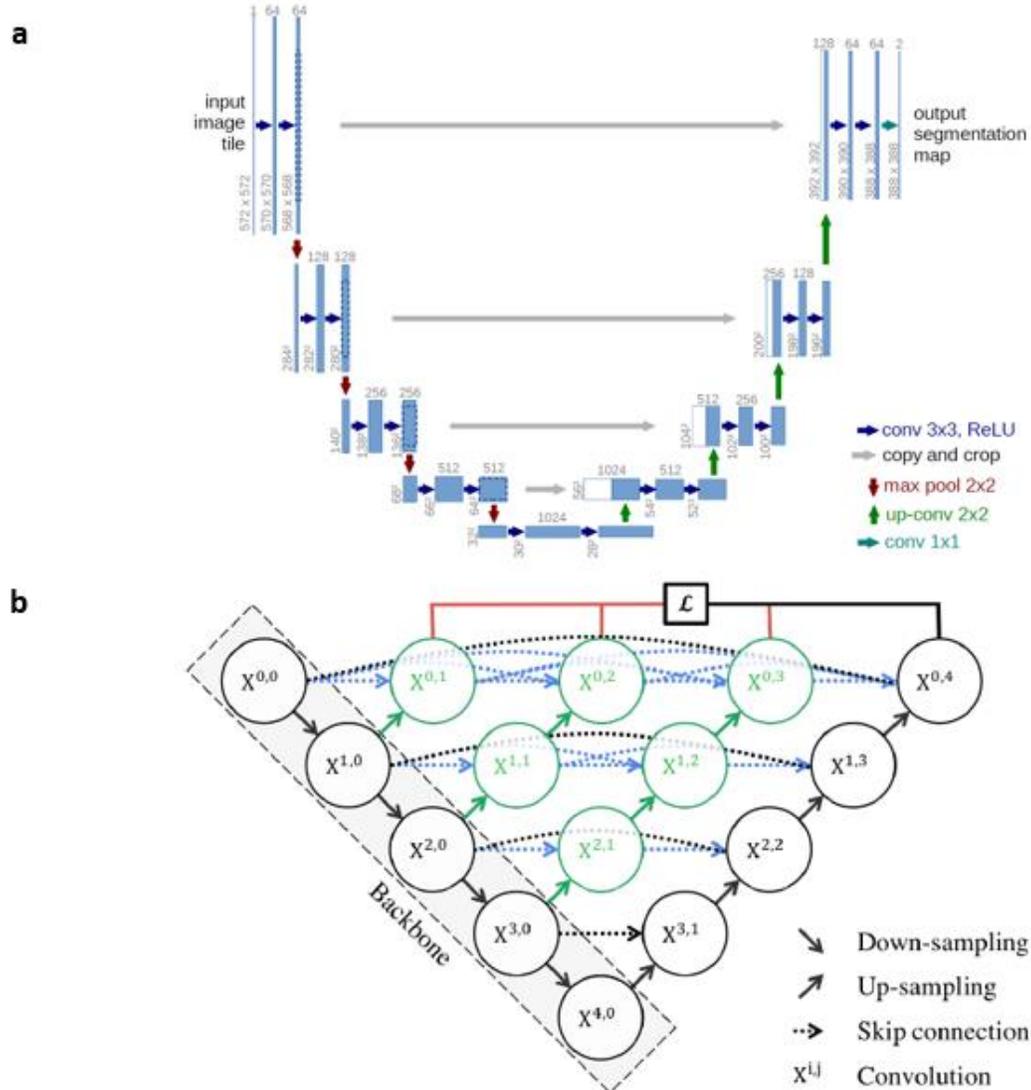
Figure 2-1: U-Net and U-Net++ Architecture.
(a) U-Net architecture (b) U-Net++ architecture. Resnet 152 is used as the backbone in the U-Net++. The redesigned skip connections are added to reduce the semantic gap between the contracting and expanding pathway compared to the original U-Net architecture. Image adapted from Ronneberger et al. (2015)[98] and Zhou et al. (2018)[14]. Permission to reproduce provided in Appendix B.

Since training a convolutional neural network with randomly initialized weights requires a large amount of data, we used transfer learning[108] in our architecture. We used a pre-

trained version of ResNet 152 that was trained on the ImageNet [109] dataset. In Deep Neural Networks as the backpropagation takes place to update the network, the partial derivative will get either very small or very large, resulting in the vanishing/exploding gradient problem.[110,111] To overcome this challenge, ResNet[112] was proposed in 2015, introducing the concept of Residual Blocks combined with skip connection. Considering the advantages of this network, we used a configuration of ResNet with 152 layers as the backbone of implementing the U-Net++ architecture. Then, the pre-trained version of ResNet 152 speeded up the training process and resulted in faster convergence.

To improve the robustness of the model and pre-process the dataset, we applied some data augmentation [113] techniques. To make our model invariant to translation (moving the image along the X or Y axis) we applied [-20 20] pixel translation in the X direction and the same in the Y direction. Additionally, we applied [-30∘ 30∘] rotation in both directions to our input images to increase the robustness of our model in case the input images have some rotations. Moreover, to make the model size invariance we performed [0.8 1.2] size and intensity scaling. Finally, elastic deformation, which has proved very useful in image segmentation tasks,[98] was applied.

The training dataset consisted of 18 image sets of lung MR images from 18 subjects. The test dataset consisted of 10 lung MR image sets from 10 subjects. To train the model, the Adam[114] optimizer was selected as the optimization algorithm. To measure how far the model predictions were from the ground truths, one took advantage of cross-entropy loss for training, Eqn. [2]:

$$E(W,b) = -\sum_{i=1}^{m} \hat{y_i} \log p_i \qquad [2]$$

where y is the target probability, p is the predicted probability, and m is the number of classes.

Finally, the network parameters were optimized for 200 epochs, each with 100 updates, and for each update in each epoch, only 20 2D slices from the entire training dataset were used to update the network weights. The learning rate of 0.0001 was used as the step size and a batch size of 20 was used to speed up the learning process.

The network was implemented with Keras 2.2.4 and Python 2.7 platforms on an NVIDIA Tesla P100 (NVIDIA Corp., Santa Clara, CA, USA) Graphics Processing Unit (GPU) provided by Canada Computers (https://www.canadacomputers.com).

The deep-learning based algorithm used a U-Net++ network[14] trained on 15 isotropic ^{1}H MRI datasets. This trained-network was used to segment the lung in the isotropic proton-lung images for each participant. An affine and deformable registration from the NiftyReg package (http://cmictig.cs.ucl.ac.uk/wiki/index.php/NiftyReg) was used to register the ^{1}H MR images to the ^{129}Xe volumes. The lung-segmentation was warped and the ^{129}Xe image-signal within the warped-lung-masks were automatically segmented into 5-clusters using a 3D k-means-clustering-approach. VDP was calculated by normalizing ^{129}Xe ventilation-defects represented by the 1st cluster to the warped lung-masks.[15]

Texture analysis is a quantitative post-processing method which characterizes regions of an image based on their texture which can be used to identify heterogeneity. Recently studies have combined the use of texture analysis with machine learning for imaging applications.[115,116] Registration is required to determine the ground truth for texture analysis and previous methods include ^{3}He MRI co-registered with computed tomography (CT) using rigid,[117] affine,[118] and deformable[119] techniques. More recently, an automated approach has been developed by registering both CT and ^{3}He MRI to ^{1}H MRI using *NiftyReg* affine and deformable registration tools.[15]

Figure 2-3 shows the overall workflow of the Deep Learning based segmentation framework. First, input images are pre-processed in order to make the inputs ready for the network. Then, the model starts training. After each epoch, the model's hyperparameter

are updated to reduce the model loss. At the end the segmentation masks are provided as the output of the network. These segmentation masks are able to be compared to segmentation masks created by other methods, such as semi-automated and manual segmentation.

Inputs

Pre-processing

$\mathcal{L}$

$X^{0,0}$ $X^{0,1}$ $X^{0,2}$ $X^{9,3}$ $X^{0,4}$

$X^{1,0}$ $X^{1,1}$ $X^{1,2}$ $X^{1,3}$

$X^{2,0}$ $X^{2,1}$ $X^{2,2}$

$X^{3,0}$ $X^{3,1}$

$X^{4,0}$

Backbone

↘ Down-sampling
↗ Up-sampling
⇢ Skip connection
$X^{i,j}$ Convolution

Model evaluation and Hyperparameter

Perform Inference

Outputs
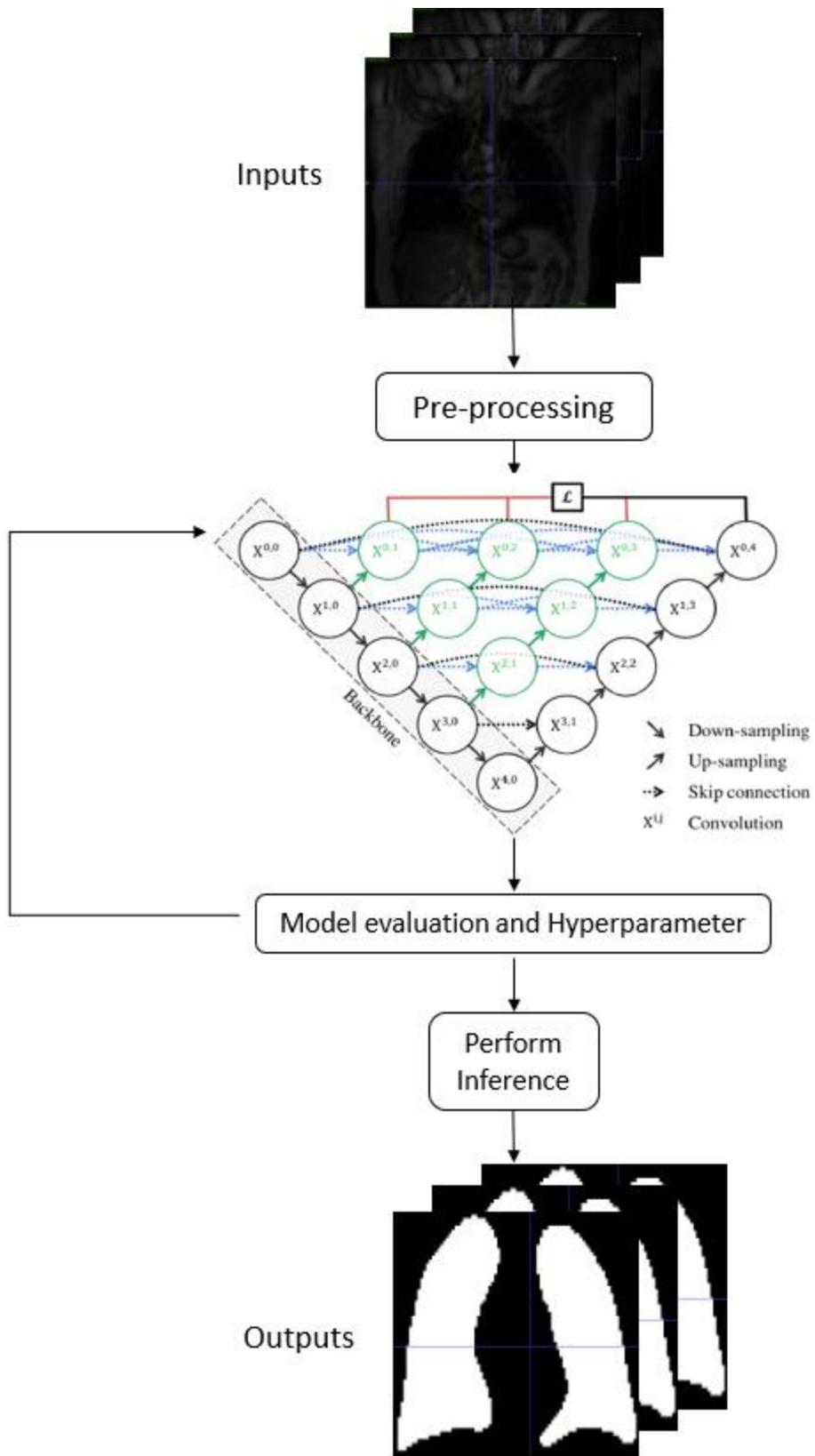
Figure 2-2: Deep-Learning-Based Segmentation Workflow.
First, input images are pre-processed in order to make the inputs ready for the network. Then, the model starts training. After each epoch, the model's hyperparameter are updated to reduce the model loss. At the end the segmentation masks are provided as the output of the network. Image adapted from Ronneberger et al. (2015) [98]. Permission to reproduce provided in Appendix B.

Statistics Analysis

Pearson correlation coefficient was used to determine the relationship between SA and DL-based VDP values. T-tests were performed using SPSS Statistics, V26.0 (SPSS Inc., Chicago, IL). Results were considered significant when the probability of two-tailed type I error (α) was less than 5% (p<.05). Bland-Altman (BA) was conducted for both SA and DL-based VDP estimates. The Sørensen-Dice (similarity) coefficient (DSC) was used for validation:

$$Dice = 2x \ \frac{y \cap y\_pred}{y + y\_pred} \qquad\qquad [3]$$

where y is the ground truth image and y_pred is the prediction of our model.

The model's performance was also tested with Dice Similarity Coefficient (DSC). DSC values can vary from 0 to 100%, 0% indicating that there is no spatial overlap between the ground truth segmentation mask and the predicted mask, and 100% indicating there is a complete overlap. DSCs were calculated for three posterior, central and anterior slices, totalling 9 slices.

2.3 Results

Table 1 summarizes demographic information and pulmonary function tests for all participants. Participant's age ranged from 29 to 76, mean FEV_1 =79 and mean FVC = 81. The DL_{co} ranged from 63% to 91% and the RV from 73% to 116% for five participants.

Table 1: Demographics and ^{129}Xe MRI Results

	P1	P2	P3	P4	P5	P6	P7	P8	P9	P10
Age	74F	76M	69M	29F	47F	61F	63F	52F	36M	55M
BMI (kg/m²)	33.6	36.6	41.1	19.2	20.8	38.4	33.4	28.4	32.0	29.0
FEV₁ %	71	78	70	67	75	117	89	61	76	82
FVC %	91	73	66	92	60	111	88	66	73	94
RV %						73	95	95	116	115
DL$_{CO}$%						83	66	90	91	63
SA VDP %	2.3	2.9	1.9	0.5	0.3	3.9	2.5	0.6	0.8	0.9
DL VDP %	2.6	2.3	1.1	0.3	0.3	3.4	3.9	0.4	0.7	0.8
SNR-1	12.5	14.8	14	40	24.2	28.6	6.8	19.3	24.6	26.3
SNR-2	11.9	16	13.3	42.1	28.4	30.1	5.7	21.8	22.7	24.6
SNR-3	12.7	13.2	16	35.4	34.8	33.2	6.1	21.3	26.2	19.7
DC-A %	72	74	88	64	0	82	85	54	61	84
DC-A %	84	58	87	87	90	90	86	81	79	82
DC-A %	85	57	90	92	94	93	89	91	88	90
DC-C %	91	95	92	94	93	95	92	96	94	95
DC-C %	91	92	92	92	92	94	93	96	92	95
DC-C %	96	89	93	93	94	96	95	94	94	93
DC-P %	86	88	93	92	88	96	86	95	94	95
DC-P %	83	87	95	0	0	94	80	87	71	92
DC-P %	87	78	86	-	-	75	78	0	0	87

P=participant; BMI=body mass index; FEV$_1$=forced expiratory volume in 1 second; FVC=forced vital capacity; RV=residual volume; DL$_{CO}$=diffusing capacity for carbon monoxide; ^{129}Xe MRI-based VDP=ventilation defect percent, SNR=signal to noise ratio, SA= Semi-Automated, DL=Deep Learning, DSC= Dice Similarity Coefficient (A=anterior slices, C=central slices, P=posterior slices). Zero values represent images that have no segmentation from the DL algorithm and very little segmentation from manual segmentation. This is commonly seen in slices very close to anterior and posterior imaging of the lungs. DSC with no values indicate no lung segmentation from either method.

Figure 2-4 shows coronal view for the non-isotropic voxel (3x3x15 mm^3) ^{129}Xe MRI static-ventilation slices from anterior to posterior for a representative COVID-19 participant. Images visualize ventilation defects in the lungs. The calculated mean SNR values of the 3 central slices from all participants ranged from 13 to 106.
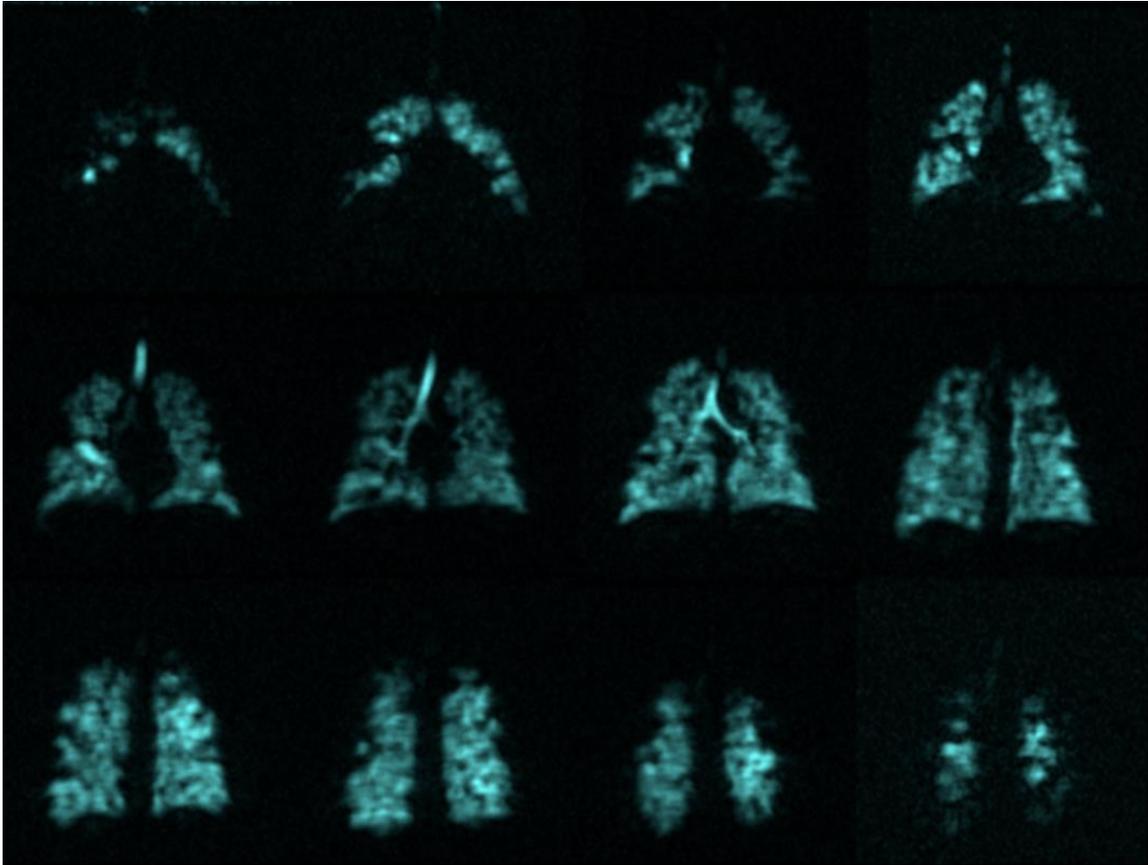
Figure 2-3: Coronal View of the Non-Isotropic (3x3x15mm^3) ^{129}Xe MRI Static-Ventilation Slices.
From anterior to posterior for the representative participant. Areas with ventilation defects can be visualized by the dark regions seen within the lungs.

Figures 2-5 and 2-6 show coronal and axial view slices for the isotropic voxel (3x3x3mm^3) ^{129}Xe MRI static-ventilation for same COVID-19 participant, respectively. Images show ventilation defects in the lungs. The calculated mean SNR values of the 3 central slices from all participants ranged from 6 to 39 (Table 1).
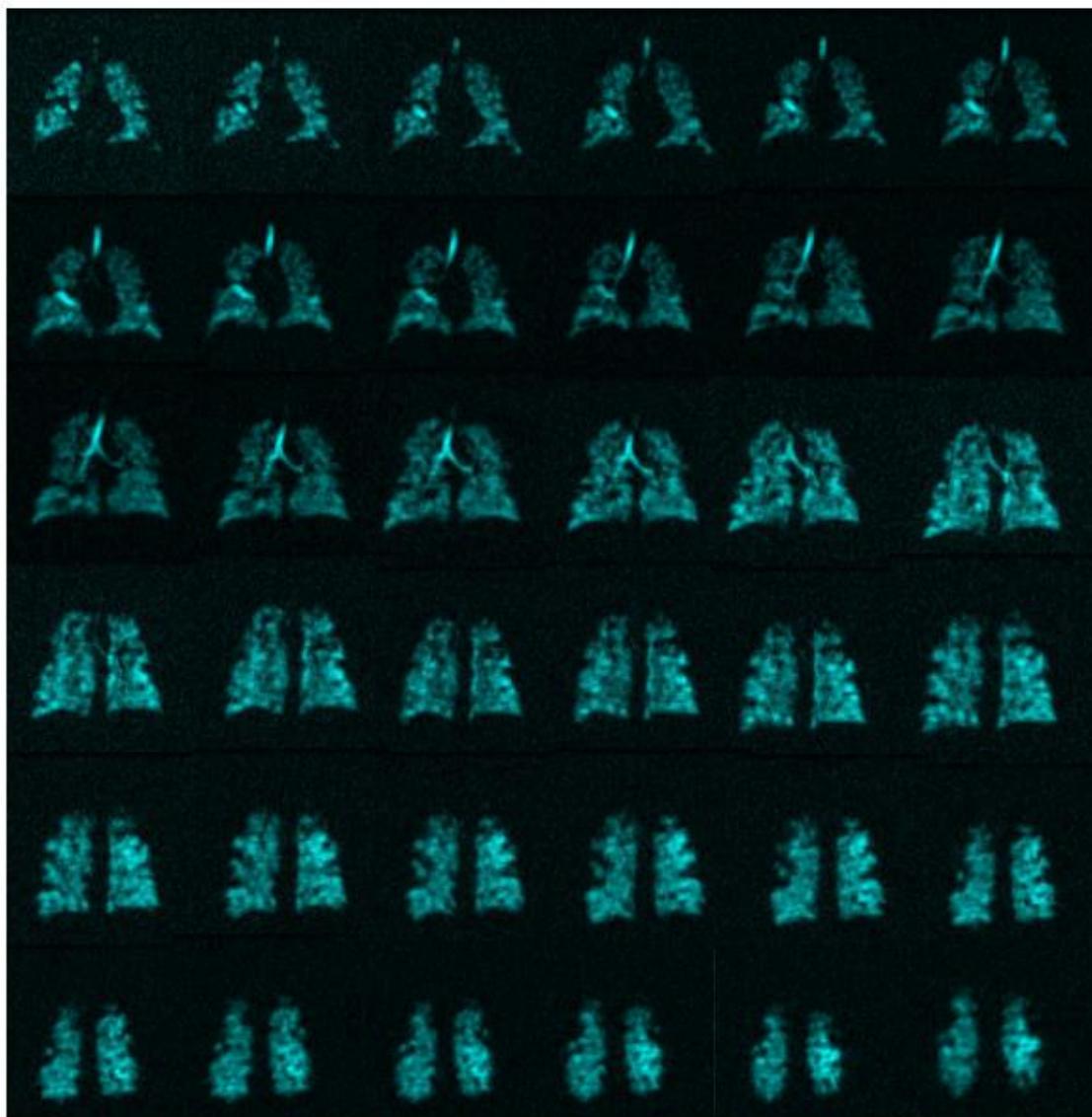
Figure 2-4: Coronal view of the isotropic pixel (3x3x3mm³) ^{129}Xe MRI static-ventilation slices.
From anterior to posterior for the representative participant. The dark regions within the lung images show the ventilation defects.
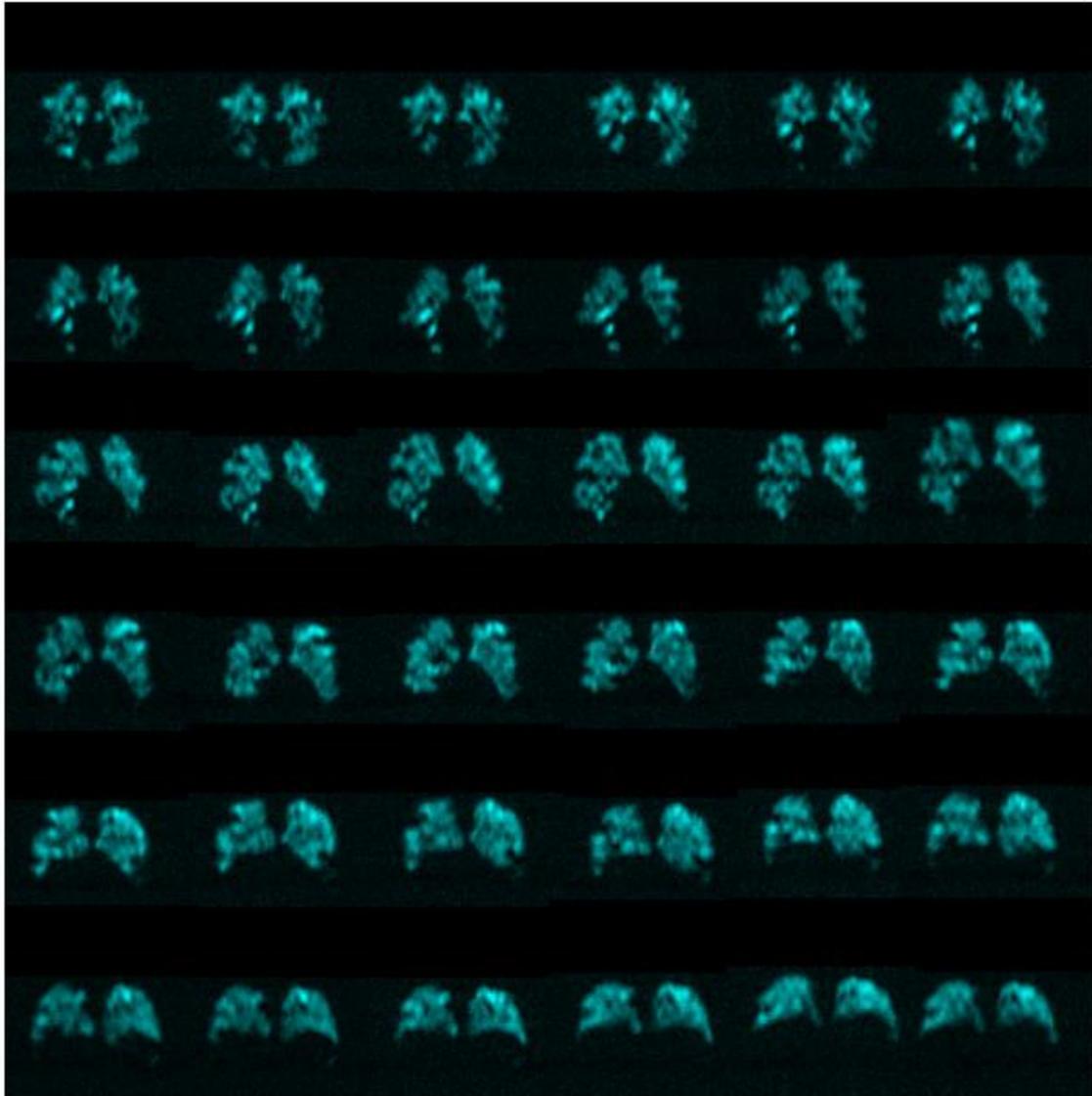
Figure 2-5: Axial view of the isotropic pixel (3x3x3mm^3) ^{129}Xe MRI static-ventilation slices.
From superior to inferior for the representative participant. The dark regions within the lung images show the ventilation defects.

Figure 2-7 (top panel) shows proton lung segmentation obtained from the DL-based automated lung segmentation algorithm in coronal, axial and sagittal views. Figure 2-7 (bottom panel) displays the xenon lung segmentation obtained from the DL-based automated lung segmentation algorithm in coronal, axial and sagittal views after applying the k-means clustering approach in all three views.
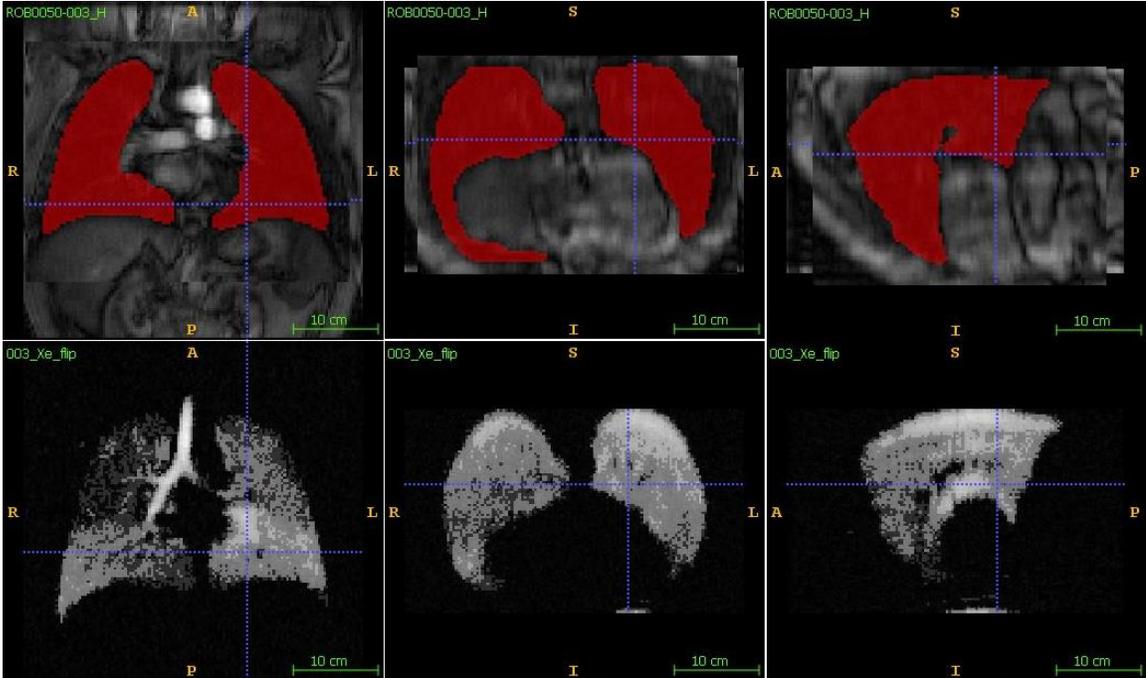
Figure 2-6: Representative Proton and Xenon Lung Images.
Representative proton lung segmentation obtained with the DL-based automated-lung-segmentation-algorithm for the coronal, axial, and sagittal views (top panel).
Representative xenon clustering lung images obtained using a 3D k-means-clustering-approach for the coronal, axial, and sagittal views (bottom panel).

The VDP values for the semi-automated segmentation method were 2.3%, 2.9%, 1.9%, 0.5%, 0.3%, 3.9%, 2.5%, 0.6%, 0.8%, 0.9% for participants 1 to 10, respectively (Table 1). The overall SA VDP mean value was 1.7±0.72 (at 95% confidence interval). The VDP values for the deep-learning based segmentation method were 2.6%, 2.3%, 1.1%, 0.3%, 0.3%, 3.4%, 3.9%, 0.4%, 0.7%, 0.8% for participants 1 to 10, respectively (Table 1). The overall mean DL VDP value was 1.6±0.80 (at 95% confidence interval). Both semi-automated and deep learning based VDP calculations were provided and the largest disagreement between two VDP estimates was found for P7, SA VDP = 2.5% and DL VDP = 3.9%. This participant also showed the smallest SNR values.

SA VDP values took approximately 45-mins to 1-hour for each participant, totalling about 10 hours for the entire dataset. DL VDP values took approximately 10-mins for each participant, totalling about 1.5 hours for the entire dataset.

Figure 2-8 shows the relationship between the SA-based VDP values with the DL-based fully automated VDP values obtained from 10 participants, intercept=-0.06±0.18, slope=0.88±0.09, and r=0.89. Participant 7 showed the largest disagreement between the two types of VDP estimates and lowest SNR values.
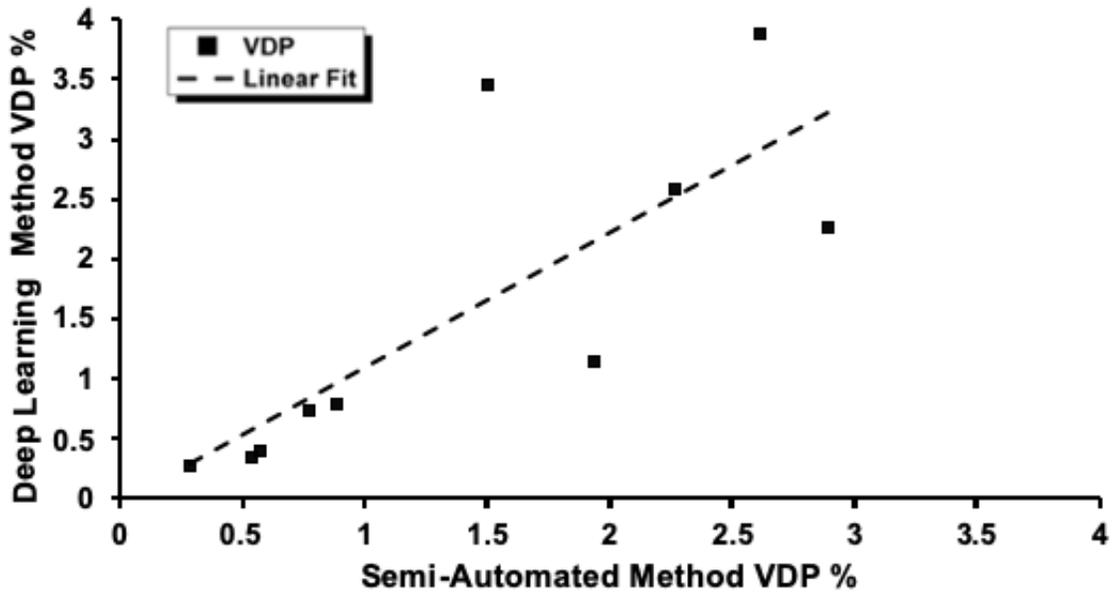
Figure 2-7: Relationship Between SA and DL VDP Values.
Relationship for semi-automated based VDP values with Deep-Learning-based fully automated VDP values obtained from nine participants. Intercept = -0.03, Slope = 1.1, R=0.89. Plot shows a strong correlation between two types of VDP.

Ventilation defect percentage for SA and DL methods both showed a significant positive correlation with FEV_1% (r = 0.72, P = 0.02 and r = 0.68, P = 0.3, respectively). Both SA and DL-based VDP values did not correlate significantly with FVC%, RV% and DL_{co}%.

Figure 2-9 shows the BA analysis for the SA and DL-based VDP estimates, and plot shows the mean of the two VDPs (solid line) and the 95% limits of agreement (dotted lines). Participants = 10, mean = -1.48±0.83, std. error mean = 0.26, r=0.51, R^2=0.26, lower limit = -0.75 and upper limit = 0.45.

Figure 2-8: Bland-Altman Analysis.
For semi-automated and deep-learning-based VDP estimates for nine participants.
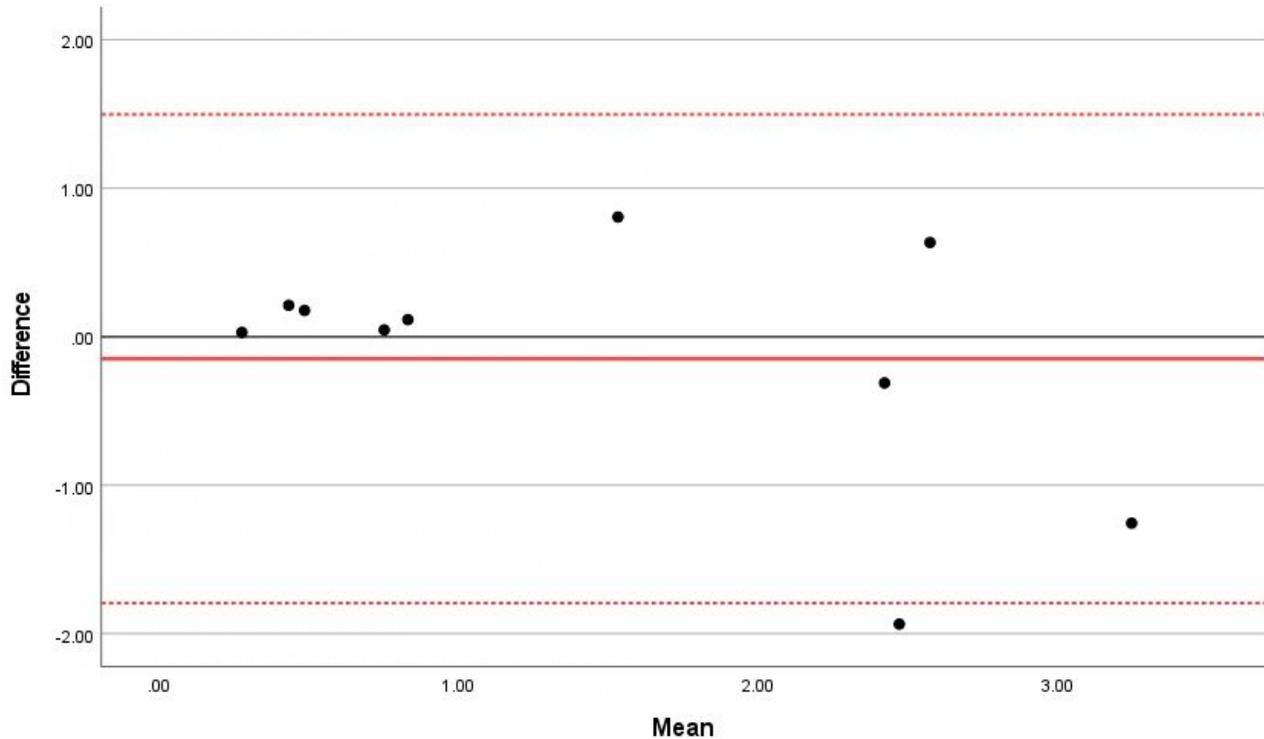
Analysis indicates negligible bias between the two types of VDPs.

DSCs calculated for segmented thoracic cavity volumes for three central slices ranged from 91% to 96% (Table 1), the overall mean values were 94±1.0%, 93±1.0% and 94±1.2% for each slice. DSCs calculated for three anterior slices ranged from 54% to 93%, excluding 0 values, and overall mean values were 66.4±7.8%, 82.4±2.8% and 86.9±3.2%, for each slice. The DSCs calculated for three posterior slices ranged from 71% to 96%, excluding 0 values, and overall mean values were 91.3±1.2%, 68.9±11.1%, and 61.38±12.6%, for each slice.

2.4 Discussion

In this proof-of-concept study, we demonstrated the possibility of generation of the isotropic voxel ^{129}Xe lung images (Figures 2-5 and 2-6) using traditional resolution images (Figure 2-4) for interpolation with signal-free k-space data. The method clearly permitted to overcome the breath-hold limitation and generate the 3D isotropic voxel size lung images. Thus, the originally acquired coronal view was extended to the axial, coronal, and sagittal views without a need for the long breath-hold and extra ^{129}Xe doses. We strongly believe that the achieved voxel size ($3x3x3mm^3$) is reasonably close to the CT scan resolution ($2x2x2mm^3$), so the quantitative analysis of the ^{129}Xe lung images should be more accurate and therefore, more reliable for disease progression observation, or therapy assessment. This is important to consider in light of the coming FDA approval of ^{129}Xe MRI.

Ventilation defect percentage for SA and DL methods showed a significant positive correlation with FEV_1% (r = 0.7232, P = 0.01809 and r = 0.6821, P = 0.02978, respectively). Both SA and DL-based VDP values did not correlate significantly with FVC%, RV% and DL_{co}%. These results are expected as previous literature using ^{129}Xe MRI has found similar significant correlations between SA VDP results and FEV_1%, but no significant correlations with FVC and DL_{co} for patients with asthma. [68] Another study found stronger correlations between FEV_1% and ^{129}Xe MRI-based VDP compared to phase resolved functional lung MRI in patients with CF.[120] Thus, it can be concluded that our correlation to FEV_1% and VDP estimates are similar to previously reported literature.

SNR was calculated for both non-isotropic voxel (original data) and isotropic voxel (generated data) ^{129}Xe MRI static-ventilation slices and were all above the Rose criteria of SNR=5.[84] The SNR-estimates for the isotropic-voxel images were approximately half of the non-isotropic images, but with voxel-size five times smaller (Table 1). The smallest SNR value for both non-isotropic and isotropic-voxel images was found for P7, with SNR between 11 to 13 and 5.7 to 6.8, respectively. This participant had the largest gap between

the two VDP values, suggesting that SNR well above 5 should be required for precise VDP calculation. In addition, this result demonstrates that the used interpolation with signal-free k-space data method permitted to generate the sufficient quality 3D isotropic-voxel lung images, so the quantitative analysis of the generated ^{129}Xe lung images was possible.

The second goal of this work was to use of deep-learning based algorithms on isotropic-voxel acquisition in a single breath-hold to evaluate ventilation defects on the lungs. The semi-automated lung segmentation method takes quite long (~45min to an hour per study subject) and should be replaced with more efficient approach to analyze the isotropic-voxel data obtained from potentially larger study participant studies.

The sufficient SNR values of the isotropic-voxel images permitted to conduct quantitative analysis and specifically, the semi-automated[67] and deep-learning-based VDP calculations for each study participant. We used the current gold standard method (semi-automated segmentation) to validate the deep learning-based approach conducting the lung segmentation and then the VDP estimate calculation utilizing the k-mean clustering method. To our knowledge this is the first report of the VDP estimates obtained from the isotropic-voxel ^{129}Xe lung images. The isotropic-voxel ^{129}Xe MRI-based VDP values have been previously measured in asthma patients and the mean VDP values we reported for both SA and DL methods were consistent with these results.[68] This further supports our hypothesis that DL-based algorithms can provide accurate VDP estimates and therefore will be able to provide accurate assessment of lung function. A strong linear correlation between SA and DL-based VDP values was found with a Pearson correlation coefficient of r=0.89 (the intercept was close to zero and slope close to unity, Figure 2-8) suggesting the reasonable accurateness of the VDP estimates obtained with the DL-based approach. Participant 7 demonstrated the largest disagreement between the two VDP estimates obtained with wo different approaches. This discrepancy may have resulted from low SNR values, suggesting that SNR values well above the Rose criteria (SNR=5)[84] should be used for accurate VDP estimation.

Further, Bland Altman analysis indicated a negligible bias between the two types of VDPs. The significance for the t-score test was not statistically significant, Sig = 0.369, suggesting that there is no proportional bias. Bland Altman analysis aids in the assessment of the degree of agreement between two methods of measurement,[121] thus we can conclude from these results that SA and DL-based VDP calculations are reliable.

The overall mean DSC values for slice 1 was $94 \pm 1.0\%$, slice 2 was $93 \pm 1.0\%$ and slice 3 was $94 \pm 1.2\%$ (at 95% confidence intervals). DSCs acquired from SA and DL based VDP values are at a range of good reproducibility and indicate high spatial overlap between the two segmentation results.[122] Thus, suggesting a good match between the ground truth (SA) and DL segmentations and further supporting the accuracy of DL-based VDP calculations.

In this pilot study, we acknowledge several study limitations including low SNR-based errors, small number of study subjects, did not validate the interpolation method used for generating isotropic-voxel images, small dataset used for the network training, and using two different semi-automated segmentation methods for the data generation for the training network and ground truth. SNR that is less than or around the Rose criteria is considered a limitation any quantitate analysis and therefore, for the VDP calculations. However, newer polarization methods with increased ^{129}Xe polarization levels (~50% polarization of a 400ml volume in 15-20 minutes) can improve SNR and image quality. Further development of MRI hardware such as a rigid and more homogenous coil[104,123] combined with a phased-receive-array[124] could drastically improve isotropic-voxel image quality and potentially replacing the isotopically-enriched ^{129}Xe with natural-abundant xenon,[125] and consequently, reducing the cost of ^{129}Xe MRI for patients without compromising the image quality.

In addition, this study was limited by sample sizes of the participants, as only 10 participants with recent infection of COVID-19 were examined. However, the goals of this study were generation of the isotropic voxel ^{129}Xe lung images and calculation of the VDP estimates using two different methods. We strongly believe that for these purposes

ten study participants should be sufficient and the number of study subjects cannot change the conclusion of this work.

We should also acknowledge that the side-by-side comparison between the generated isotropic-voxel lung images and acquired isotropic-voxel lung images was not done. To our knowledge there are no other Cartesian sampling methods (like FGRE) permitting the acquisition of the isotropic-voxel lung images in the 16sec breath-hold. The comparison between FGRE used in this work and non-Cartesian sampling method permitting the similar voxel size[86] may not be accurate due to a number of reasons and consequently is not conclusive.

Finally, it's worth mentioning that to create a more solid Deep Learning based segmentation framework for the VDP calculation, it's better to test different segmentation architectures and compare them to select the best one that suits our data. To be more specific, by testing different neural network architecture, we will be able to better overcome the common challenge of overfitting[126] in Deep Learning. Consequently, in the future works we would like to test other Deep Learning segmentation models on our dataset. Additionally, in this research study we took an approach that decided to use a manual segmentation dataset to train the neural network. Although we did use the SA segmentation method as the ground truth, we did not train the DL architecture with SA segmentation. Since the semi-automated segmentation is the current gold standard and we are comparing the final results with that method, we are going to use the semi-automated segmentation outputs as the training data for our future work.

2.5   Conclusion

The semi-automated-lung-segmentation-method[67] is widely used for hyperpolarized-gas lung image segmentation and the VDP calculation. However, isotropic voxel data requires a significant observer time (~45min to an hour per 80slices). By acquiring VDP estimates

using deep-learning-based algorithms, we increase time efficiency and reduce possibilities of human error. In this work we showed that deep-learning based algorithms on ^{129}Xe isotropic-voxel static-ventilation imaging provides a way to calculate time-efficient VDP estimates, which allows for rapid evaluation of ventilation defects. This means that fully-automated methods can be used as an alternative to semi-automated segmentation methods.

CHAPTER 3

3   CONCLUSIONS AND FUTURE DIRECTIONS

In this final chapter, an overview of the findings and the conclusions presented in Chapter 2 are summarized. Limitations related to this study are provided as well as potential solutions. Finally, the chapter concludes by discussing the future directions that can be explored and the impact and significance of this work

3.1   Overview and Research Objectives

Hyperpolarized gas MRI has been an excellent tool to provide novel insights into pulmonary diseases such as COPD and COVID-19, however, the expensive cost associated with this technique continues to pose as a challenge for application use. The overarching objective of this thesis was to employ a deep-learning-based segmentation method that can be used to quantify ventilation defects in the lungs from isotropic ^{129}Xe images and calculate accurate VDP values. The specific objectives were first to obtain isotropic voxel 3D static-ventilation lung images using an interpolation with signal-free k-space data technique, and second to use a fully-automated DL-based lung segmentation method to obtain VDP values comparable to semi-automated VDP values.

3.2   Summary and Conclusion

In Chapter 1, we discussed the motivation and rationale behind pulmonary disease studies, specifically COPD and COVID-19. We discussed the various pulmonary imaging techniques and current gaps of knowledge, as well as pathophysiology of the lungs. Then, clinical testing measures were discussed such as pulmonary function tests and to conclude, the thesis aims, and hypotheses were stated.

In Chapter 2, we were able to calculate ventilation defects, VDP, by using a fully-automated deep-learning-based lung segmentation algorithm from isotropic static-ventilation lung xenon MR images.

We found that semi-automated and deep-learning VDP values had a strong linear correlation, and both require an SNR value well above 5 to be precise. We concluded that deep-learning-based lung segmentation algorithms can be used to calculate VDP for isotropic datasets at a more efficient rate than semi-automated segmentation.

3.3   Limitations

In this section, significant limitations from Chapter 2 will be discussed. It should be noted that these limitations are also present in the Discussion section of Chapter 2.

In Chapter 2, I evaluated 10 patients with lung ventilation heterogeneity using hyperpolarized ^{129}Xe MRI to calculate ventilation defect percent. All 10 of these participants were COVID-19 survivors, this study could have been improved by including a larger number of COVID-19 survivors with ventilation defects to study differences in lung structure and function across a larger sample size. However, the aim for this study was to acquire isotropic-voxel ^{129}Xe lung images and calculate VDP estimates using two different methods. In addition, I did not evaluate other obstructive pulmonary disease patients. This study could therefore be improved by the inclusion of more patients with pulmonary diseases such as COPD to study the effects that COVID-19 may have on the lungs compared with other pulmonary diseases. Other limitations addressed in further detail in the discussion section of Chapter 2 are low SNR-based errors, validation of the method used to generate isotropic-voxel images, small dataset used for the network training, and using two different segmentation methods for the data generation for the training network and ground truth.

3.4   Future Directions

3.4.1   Longitudinal Study of Lung Defects in COVID-19 Survivors

As mentioned in the limitations, future work must be done to apply the method developed in Chapter 2 to longitudinal data. By investigating ventilation defects in the lungs of COVID-19 survivors over time, we can see potential disease progression, such as symptoms and visualization of defects from ^{129}Xe MRI. Previous work has observed

changes in pulmonary disease overtime using MR imaging and the semi-automated segmentation method, such as COPD.[127] Therefore, the method used in this thesis can easily be employed long-term to provide similar results.

3.5 Significance and Impact

Obstructive lung disease such as COPD has affected millions of individuals and is responsible for millions of deaths every year.[1] New emerging pulmonary diseases such as COVID-19 will continue to affect individuals on a global scale thus signifying the importance of lung observation methodology. Hyperpolarized gas MRI has allowed this field to gain a better understanding of ventilation defects across pulmonary diseases, however, some observations such as structural-function relationships are still not fully understood. The current gold standard to calculate VDP values is a semi-automated[67] method which is not suitable for isotropic dataset analyses due to the large number of slices and high amount of observer time.

Many studies[67,69,73] have used hyperpolarized gas MRI to measure structure and function of the lungs and semi-automated segmentation methods to calculate VDP values. However, these studies have not focused on using a fully-automated deep-learning based segmentation method for hyperpolarized gas imaging. To our knowledge this is the first report of the VDP estimates obtained from the isotropic-voxel COVID-19 Survivals ^{129}Xe lung images. In this thesis, I evaluated 10 COVID-19 survivors using hyperpolarized ^{129}Xe MRI using both semi-automated and fully-automated deep-learning based method. This study provided strong evidence that VDP estimates calculated using a deep-learning-based approach is similar to semi-automated VDP values, and importantly, provides opportunity for faster quantification of ventilation defects and abnormalities. These results provide strong support for clinical translation of hyperpolarized gas MRI for pulmonary diseases and wider application of this technique may be used to possibly identify treatment and monitoring for COVID-19 survivors.

References

1   Organization, W. H. *Chronic obstructive pulmonary disease (COPD)*,
        <https://www.who.int/news-room/fact-sheets/detail/chronic-obstructive-
        pulmonary-disease-(copd)> (2021).
2   Viegi, G., Maio, S., Fasola, S. & Baldacci, S. Global burden of chronic
        respiratory diseases. *Journal of Aerosol Medicine and Pulmonary Drug Delivery*
        33, 171-177 (2020).
3   Center, J. H. C. R. <https://coronavirus.jhu.edu/data> (
4   Wu, Z. & McGoogan, J. M. Characteristics of and Important Lessons From the
        Coronavirus Disease 2019 (COVID-19) Outbreak in China: Summary of a Report
        of 72 314 Cases From the Chinese Center for Disease Control and Prevention.
        Jama **323**, 1239-1242, doi:10.1001/jama.2020.2648 (2020).
5   Evans, J., Chen, Y., Camp, P. G., Bowie, D. M. & McRae, L. Estimating the
        prevalence of COPD in Canada: Reported diagnosis versus measured airflow
        obstruction. *Health reports* **25**, 3-11 (2014).
6   Canada, T. C. B. o. *Cost Risk Analysis for Chronic Lung Disease in Canada*,
        <https://www.conferenceboard.ca/temp/70339ec1-0a5f-4a7b-bbb9-
        c1fac0e4d639/12-114_CostRiskAnalysisv4.pdf> (
7   Mittmann, N. *et al.* The cost of moderate and severe COPD exacerbations to the
        Canadian healthcare system. *Respir Med* **102**, 413-421,
        doi:10.1016/j.rmed.2007.10.010 (2008).
8   Ontario, G. o. *Hospitalizations*, <https://covid-
        19.ontario.ca/data/hospitalizations> (2022).
9   Wiersinga, W. J., Rhodes, A., Cheng, A. C., Peacock, S. J. & Prescott, H. C.
        Pathophysiology, Transmission, Diagnosis, and Treatment of Coronavirus
        Disease 2019 (COVID-19): A Review. *Jama* **324**, 782-793,
        doi:10.1001/jama.2020.12839 (2020).
10   Guan, W. J. *et al.* Clinical Characteristics of Coronavirus Disease 2019 in China.
        N Engl J Med **382**, 1708-1720, doi:10.1056/NEJMoa2002032 (2020).
11   Kirby, M. *et al.* COPD: Do Imaging Measurements of Emphysema and Airway
        Disease Explain Symptoms and Exercise Capacity? *Radiology* **277**, 872-880,
        doi:10.1148/radiol.2015150037 (2015).
12   Kirby, M. *et al.* Hyperpolarized 3He and 129Xe MR imaging in healthy
        volunteers and patients with chronic obstructive pulmonary disease. *Radiology*
        265, 600-610, doi:10.1148/radiol.12120485 (2012).
13   Dominguez-Viqueira, W., Ouriadov, A., O'Halloran, R., Fain, S. B. & Santyr, G.
        E. Signal-to-noise ratio for hyperpolarized (3)He MR imaging of human lungs: a
        1.5 T and 3 T comparison. *Magn Reson Med* **66**, 1400-1404,
        doi:10.1002/mrm.22920 (2011).
14   Zhou, Z., Siddiquee, M. M. R., Tajbakhsh, N. & Liang, J. UNet++: Redesigning
        Skip Connections to Exploit Multiscale Features in Image Segmentation. *IEEE
        Trans Med Imaging* **39**, 1856-1867, doi:10.1109/TMI.2019.2959609 (2020).

15   Guo, F. *et al.* Thoracic CT-MRI coregistration for regional pulmonary structure-function measurements of obstructive lung disease. *Med Phys* **44**, 1718-1733, doi:10.1002/mp.12160 (2017).

16   West, J. B. *Respiratory physiology: the essentials*. (Lippincott Williams & Wilkins, 2012).

17   West, J. B. & Luks, A. M. *West's Respiratory Physiology*. (Lippincott Williams & Wilkins, 2020).

18   Comroe, J. H. The lung. *Scientific American* **214**, 56-71 (1966).

19   Vogelmeier, C. F. *et al.* Global strategy for the diagnosis, management, and prevention of chronic obstructive lung disease 2017 report. GOLD executive summary. *American journal of respiratory and critical care medicine* **195**, 557-582 (2017).

20   Standards for the diagnosis and care of patients with chronic obstructive pulmonary disease. American Thoracic Society. *American journal of respiratory and critical care medicine* **152**, S77-121 (1995).

21   Ingenito, E. P., Tsai, L. W., Majumdar, A. & Suki, B. On the role of surface tension in the pathophysiology of emphysema. *American journal of respiratory and critical care medicine* **171**, 300-304, doi:10.1164/rccm.200406-770PP (2005).

22   Takahashi, M. *et al.* Imaging of pulmonary emphysema: a pictorial review. *Int J Chron Obstruct Pulmon Dis* **3**, 193-204, doi:http://dx.doi.org/10.2147/COPD.S2639 (2008).

23   Woods, J. C. *et al.* Hyperpolarized 3He diffusion MRI and histology in pulmonary emphysema. *Magn Reson Med* **56**, 1293-1300, doi:10.1002/mrm.21076 (2006).

24   Eisner, M. D. *et al.* An official American Thoracic Society public policy statement: Novel risk factors and the global burden of chronic obstructive pulmonary disease. *American journal of respiratory and critical care medicine* **182**, 693-718, doi:10.1164/rccm.200811-1757ST (2010).

25   Kim, V. & Criner, G. J. Chronic bronchitis and chronic obstructive pulmonary disease. *American journal of respiratory and critical care medicine* **187**, 228-237, doi:10.1164/rccm.201210-1843CI (2013).

26   Kim, V. *et al.* Small airway mucous metaplasia and inflammation in chronic obstructive pulmonary disease. *Copd* **5**, 329-338, doi:10.1080/15412550802522445 (2008).

27   Ebert, R. V. & Terracio, M. J. The bronchiolar epithelium in cigarette smokers. Observations with the scanning electron microscope. *The American review of respiratory disease* **111**, 4-11, doi:10.1164/arrd.1975.111.1.4 (1975).

28   Deshmukh, H. S. *et al.* Metalloproteinases mediate mucin 5AC expression by epidermal growth factor receptor activation. *American journal of respiratory and critical care medicine* **171**, 305-314, doi:10.1164/rccm.200408-1003OC (2005).

29   Ksiazek, T. G. *et al.* A novel coronavirus associated with severe acute respiratory syndrome. *N Engl J Med* **348**, 1953-1966, doi:10.1056/NEJMoa030781 (2003).

30   Yuki, K., Fujiogi, M. & Koutsogiannaki, S. COVID-19 pathophysiology: A review. *Clinical immunology (Orlando, Fla.)* **215**, 108427, doi:10.1016/j.clim.2020.108427 (2020).

31   Yuki, K., Fujiogi, M. & Koutsogiannaki, S. J. C. i. COVID-19 pathophysiology: A review. **215**, 108427 (2020).

32   Fernández-de-Las-Peñas, C. *et al.* Defining post-COVID symptoms (post-acute COVID, long COVID, persistent post-COVID): an integrative classification. **18**, 2621 (2021).

33   Zhou, F. *et al.* Clinical course and risk factors for mortality of adult inpatients with COVID-19 in Wuhan, China: a retrospective cohort study. *Lancet* **395**, 1054-1062, doi:10.1016/s0140-6736(20)30566-3 (2020).

34   Wang, M., Hao, H., Leeper, N. J. & Zhu, L. Thrombotic Regulation From the Endothelial Cell Perspectives. *Arteriosclerosis, thrombosis, and vascular biology* **38**, e90-e95, doi:10.1161/atvbaha.118.310367 (2018).

35   Quanjer, P. H. *et al.* Multi-ethnic reference values for spirometry for the 3-95-yr age range: the global lung function 2012 equations. *The European respiratory journal* **40**, 1324-1343, doi:10.1183/09031936.00080312 (2012).

36   Miller, M. R. *et al.* Standardisation of spirometry. *The European respiratory journal* **26**, 319-338, doi:10.1183/09031936.05.00034805 (2005).

37   Coates, A., Peslin, R., Rodenstein, D. & Stocks, J. Measurement of lung volumes by plethysmography. *European Respiratory Journal* **10**, 1415-1427 (1997).

38   Criée, C. *et al.* Body plethysmography–its principles and clinical use. *Respiratory medicine* **105**, 959-971 (2011).

39   Modi, P. & Cascella, M. Diffusing capacity of the lungs for carbon monoxide. (2020).

40   Frans, A., Nemery, B., Veriter, C., Lacquet, L. & Francis, C. Effect of alveolar volume on the interpretation of single breath DLCO. *Respiratory medicine* **91**, 263-273 (1997).

41   Graham, B. L. *et al.* Executive Summary: 2017 ERS/ATS standards for single-breath carbon monoxide uptake in the lung. *European Respiratory Journal* **49** (2017).

42   Goergen, B. O. S. S. *Insider Radiology: Plain Radiograph/X-ray*, <https://www.insideradiology.com.au/plain-radiograph-x-ray/> (

43   Gevenois, P. A. *et al.* Comparison of computed density and microscopic morphometry in pulmonary emphysema. *American journal of respiratory and critical care medicine* **154**, 187-192, doi:10.1164/ajrccm.154.1.8680679 (1996).

44   Kirby, M. *et al.* Total Airway Count on Computed Tomography and the Risk of Chronic Obstructive Pulmonary Disease Progression. Findings from a Population-based Study. *American journal of respiratory and critical care medicine* **197**, 56-65, doi:10.1164/rccm.201704-0692OC (2018).

45   Park, J. *et al.* Subtyping COPD by Using Visual and Quantitative CT Imaging Features. *Chest* **157**, 47-60, doi:10.1016/j.chest.2019.06.015 (2020).

46   Herth, F. J. F. *et al.* The Modern Art of Reading Computed Tomography Images of the Lungs: Quantitative CT. *Respiration; international review of thoracic diseases* **95**, 8-17, doi:10.1159/000480435 (2018).

47   Shi, H. *et al.* Radiological findings from 81 patients with COVID-19 pneumonia in Wuhan, China: a descriptive study. *The Lancet. Infectious diseases* **20**, 425-434, doi:10.1016/s1473-3099(20)30086-4 (2020).

48   Bernheim, A. *et al.* Chest CT Findings in Coronavirus Disease-19 (COVID-19): Relationship to Duration of Infection. *Radiology* **295**, 200463, doi:10.1148/radiol.2020200463 (2020).

49   Watz, H., Breithecker, A., Rau, W. S. & Kriete, A. Micro-CT of the human lung: imaging of alveoli and virtual endoscopy of an alveolar duct in a normal lung and in a lung with centrilobular emphysema--initial observations. *Radiology* **236**, 1053-1058, doi:10.1148/radiol.2363041142 (2005).

50   Health, U. D. o. & Services, H.   (National Institute of Biomedical Imaging and Bioengineering. https://www …).

51   Fain, S., Schiebler, M. L., McCormack, D. G. & Parraga, G. Imaging of lung function using hyperpolarized helium-3 magnetic resonance imaging: Review of current and emerging translational methods and applications. *Journal of magnetic resonance imaging : JMRI* **32**, 1398-1408, doi:10.1002/jmri.22375 (2010).

52   Leawoods, J. C., Yablonskiy, D. A., Saam, B., Gierada, D. S. & Conradi, M. S. J. C. i. M. R. A. E. J. Hyperpolarized 3He gas production and MR imaging of the lung. **13**, 277-293 (2001).

53   Wild, J. M. *et al.* MRI of the lung (1/3): methods. *Insights into imaging* **3**, 345-353 (2012).

54   Grover, B. Noble-gas NMR detection through noble-gas-rubidium hyperfine contact interaction. *Physical Review Letters* **40**, 391 (1978).

55   Driehuys, B. *et al.* Chronic obstructive pulmonary disease: safety and tolerability of hyperpolarized 129Xe MR imaging in healthy volunteers and patients. *Radiology* **262**, 279-289, doi:10.1148/radiol.11102172 (2012).

56   Parraga, G. *et al.* Hyperpolarized 3He ventilation defects and apparent diffusion coefficients in chronic obstructive pulmonary disease: preliminary results at 3.0 Tesla. *Invest Radiol* **42**, 384-391, doi:10.1097/01.rli.0000262571.81771.66 (2007).

57   Shukla, Y. *et al.* Hyperpolarized 129Xe magnetic resonance imaging: tolerability in healthy volunteers and subjects with pulmonary disease. *Academic radiology* **19**, 941-951, doi:10.1016/j.acra.2012.03.018 (2012).

58   Lutey, B. A. *et al.* Hyperpolarized 3He MR imaging: physiologic monitoring observations and safety considerations in 100 consecutive subjects. *Radiology* **248**, 655-661, doi:10.1148/radiol.2482071838 (2008).

59   Albert, M. S. *et al.* Biological magnetic resonance imaging using laser-polarized 129Xe. *Nature* **370**, 199-201 (1994).

60   Mugler, J. P. *et al.* MR imaging and spectroscopy using hyperpolarized129Xe gas: Preliminary human results. *Magnetic Resonance in Medicine* **37**, 809-815, doi:10.1002/mrm.1910370602 (1997).

61   Westcott, A., Guo, F., Parraga, G. & Ouriadov, A. Rapid single-breath hyperpolarized noble gas MRI-based biomarkers of airspace enlargement. *Journal of magnetic resonance imaging : JMRI* **49**, 1713-1722, doi:10.1002/jmri.26574 (2019).

62   Kaushik, S. S. *et al.* Single-breath clinical imaging of hyperpolarized (129)Xe in the airspaces, barrier, and red blood cells using an interleaved 3D radial 1-point Dixon acquisition. *Magn Reson Med* **75**, 1434-1443, doi:10.1002/mrm.25675 (2016).

63   Bartel, S.-E. T. *et al.* Role of collateral paths in long-range diffusion in lungs. *Journal of applied physiology* **104**, 1495-1503 (2008).

64   Tustison, N. J. *et al.* Image-versus histogram-based considerations in semantic segmentation of pulmonary hyperpolarized gas images. **86**, 2822-2836 (2021).

65   He, M. *et al.* A Comparison of Two Hyperpolarized (129)Xe MRI Ventilation Quantification Pipelines: The Effect of Signal to Noise Ratio. *Academic radiology* **26**, 949-959, doi:10.1016/j.acra.2018.08.015 (2019).

66   He, M., Driehuys, B., Que, L. G. & Huang, Y. T. Using Hyperpolarized (129)Xe MRI to Quantify the Pulmonary Ventilation Distribution. *Academic radiology* **23**, 1521-1531, doi:10.1016/j.acra.2016.07.014 (2016).

67   Kirby, M. *et al.* Hyperpolarized 3He magnetic resonance functional imaging semiautomated segmentation. *Academic radiology* **19**, 141-152, doi:10.1016/j.acra.2011.10.007 (2012).

68   Barker, A. L. *et al.* Feasibility of Single Breath-hold Isotropic Voxel 129Xe MRI in Patients. *ISMRM 19th Annual Meeting, Paris, France* (2019).

69   Kirby, M., Pike, D., Coxson, H. O., McCormack, D. G. & Parraga, G. Hyperpolarized (3)He ventilation defects used to predict pulmonary exacerbations in mild to moderate chronic obstructive pulmonary disease. *Radiology* **273**, 887-896, doi:10.1148/radiol.14140161 (2014).

70   Svenningsen, S. *et al.* What are ventilation defects in asthma? *Thorax* **69**, 63-71, doi:10.1136/thoraxjnl-2013-203711 (2014).

71   Kirby, M. *et al.* Chronic obstructive pulmonary disease: quantification of bronchodilator effects by using hyperpolarized He MR imaging. **261**, 283-292 (2011).

72   Svenningsen, S. *et al.* Hyperpolarized (3) He and (129) Xe MRI: differences in asthma before bronchodilation. *Journal of magnetic resonance imaging : JMRI* **38**, 1521-1530, doi:10.1002/jmri.24111 (2013).

73   Svenningsen, S. *et al.* Sputum Eosinophilia and Magnetic Resonance Imaging Ventilation Heterogeneity in Severe Asthma. *American journal of respiratory and critical care medicine* **197**, 876-884, doi:10.1164/rccm.201709-1948OC (2018).

74   Kołodziej, M., de Veer, M. J., Cholewa, M., Egan, G. F. & Thompson, B. R. Lung function imaging methods in Cystic Fibrosis pulmonary disease. *Respiratory research* **18**, 96, doi:10.1186/s12931-017-0578-x (2017).

75   Walkup, L. L. *et al.* Feasibility, tolerability and safety of pediatric hyperpolarized (129)Xe magnetic resonance imaging in healthy volunteers and children with cystic fibrosis. *Pediatr Radiol* **46**, 1651-1662, doi:10.1007/s00247-016-3672-1 (2016).

76   Moller, H. E. *et al.* MRI of the lungs using hyperpolarized noble gases. *Magn Reson Med* **47**, 1029-1051, doi:10.1002/mrm.10173 (2002).

77   Velavan, T. P. & Meyer, C. G. The COVID-19 epidemic. *Tropical medicine & international health : TM & IH* **25**, 278-280, doi:10.1111/tmi.13383 (2020).

78   Su, S. *et al.* Epidemiology, Genetic Recombination, and Pathogenesis of Coronaviruses. *Trends in microbiology* **24**, 490-502, doi:10.1016/j.tim.2016.03.003 (2016).

79   Li, H. *et al.* Damaged lung gas exchange function of discharged COVID-19 patients detected by hyperpolarized (129)Xe MRI. *Science advances* **7**, doi:10.1126/sciadv.abc8180 (2021).

80   Grist, J. T. *et al.* Hyperpolarized (129)Xe MRI Abnormalities in Dyspneic Patients 3 Months after COVID-19 Pneumonia: Preliminary Results. *Radiology* **301**, E353-e360, doi:10.1148/radiol.2021210033 (2021).

81   Dietrich, O. Detecting COVID-19-related Chronic Pulmonary Injury with (129)Xe MRI. *Radiology* **301**, E373-e374, doi:10.1148/radiol.2021211087 (2021).

82   Grist, J. T. *et al.* The Investigation of Pulmonary Abnormalities using Hyperpolarised Xenon Magnetic Resonance Imaging in Patients with Long-COVID. (2022).

83   Wild, J. M. *et al.* Understanding the burden of interstitial lung disease post-COVID-19: the UK Interstitial Lung Disease-Long COVID Study (UKILD-Long COVID). **8**, e001049 (2021).

84   Rose, A. The sensitivity performance of the human eye on an absolute scale. *Journal of the Optical Society of America* **38**, 196-208, doi:10.1364/josa.38.000196 (1948).

85   Ranota, T. K., Serrai, H., McCormack, D. G., Parraga, G. & Ouriadov, A. Feasbility of Single Breath-hold Isotropic Voxel 129Xe MRI in COVID-19 Survivors using a Key-Hole Method [abstract]. *ISMRM 30th Annual Meeting* (2021).

86   Wolber, J., Cherubini, A., Dzik-Jurasz, A. S., Leach, M. O. & Bifone, A. Spin-lattice relaxation of laser-polarized xenon in human blood. *Proc Natl Acad Sci U S A* **96**, 3664-3669 (1999).

87   Norquay, G. *et al.* in *Proc 25th Annual Meeting ISMRM, Honolulu.* 2140.

88   Ranota, T. K., Guo, F., Wu, T., Fox, M. S. & Ouriadov, A. Automated Quantification of Ventilation Defects and Heterogeneity in 3D Isotropic 129Xe MRI. *ISMRM 2022 Annual Meeting, London, England, UK* **Abstract** (2022).

89   Coleman, G. B. & Andrews, H. C. Image segmentation by clustering. *Proceedings of the IEEE* **67**, 773-785, doi:10.1109/PROC.1979.11327 (1979).

90   McInerney, T. & Terzopoulos, D. Deformable models in medical image analysis: a survey. *Med Image Anal* **1**, 91-108, doi:10.1016/s1361-8415(96)80007-7 (1996).

91   Lei, T. *et al.* Medical Image Segmentation Using Deep Learning: A Survey. (2020).

92   Litjens, G. *et al.* A survey on deep learning in medical image analysis. *Med Image Anal* **42**, 60-88, doi:10.1016/j.media.2017.07.005 (2017).

93   Ranjbarzadeh, R. *et al.* Brain tumor segmentation based on deep learning and an attention mechanism using MRI multi-modalities brain images. **11**, 1-17 (2021).

94   Zhao, T., Gao, D., Wang, J. & Yin, Z. in *2018 IEEE 15th International Symposium on Biomedical Imaging (ISBI 2018).* 505-509 (IEEE).

95   Men, K. *et al.* Fully automatic and robust segmentation of the clinical target volume for radiotherapy of breast cancer using big data and deep learning. **50**, 13-19 (2018).

96 Winther, H. B. *et al.* Deep semantic lung segmentation for tracking potential pulmonary perfusion biomarkers in chronic obstructive pulmonary disease (COPD): The multi-ethnic study of atherosclerosis COPD study. **51**, 571-579 (2020).

97 Shelhamer, E., Long, J. & Darrell, T. Fully Convolutional Networks for Semantic Segmentation. *IEEE transactions on pattern analysis and machine intelligence* **39**, 640-651, doi:10.1109/tpami.2016.2572683 (2017).

98 Ronneberger, O., Fischer, P. & Brox, T. U-Net: Convolutional Networks for Biomedical Image Segmentation. (2015).

99 Ohno, Y. *et al.* Pulmonary Functional Imaging: Part 1-State-of-the-Art Technical and Physiologic Underpinnings. *Radiology* **299**, 508-523, doi:10.1148/radiol.2021203711 (2021).

100 Park, B., Park, H., Lee, S. M., Seo, J. B. & Kim, N. Lung Segmentation on HRCT and Volumetric CT for Diffuse Interstitial Lung Disease Using Deep Convolutional Neural Networks. *Journal of digital imaging* **32**, 1019-1026, doi:10.1007/s10278-019-00254-8 (2019).

101 Duan, C. *et al.* Fast and accurate reconstruction of human lung gas MRI with deep learning. *Magnetic Resonance in Medicine* **0**, doi:10.1002/mrm.27889.

102 Westcott, A. *et al.* Chronic Obstructive Pulmonary Disease: Thoracic CT Texture Analysis and Machine Learning to Predict Pulmonary Ventilation. *Radiology* **293**, 676-684, doi:10.1148/radiol.2019190450 (2019).

103 Matheson, A. M. *et al.* Never-hospitalized patients with post-acute COVID19 syndrome: 129Xe MRI gas-exchange abnormalities. *British Medical Journal: Open Respiratory Research* (2022).

104 Ouriadov, A. *et al.* Lung morphometry using hyperpolarized (129) Xe apparent diffusion coefficient anisotropy in chronic obstructive pulmonary disease. *Magn Reson Med* **70**, 1699-1706, doi:10.1002/mrm.24595 (2013).

105 Kaushik, S. S. *et al.* Diffusion-weighted hyperpolarized 129Xe MRI in healthy volunteers and subjects with chronic obstructive pulmonary disease. *Magn Reson Med* **65**, 1154-1165, doi:10.1002/mrm.22697 (2011).

106 Niedbalski, P. J. *et al.* Mapping and correcting hyperpolarized magnetization decay with radial keyhole imaging. *Magn Reson Med* **82**, 367-376, doi:10.1002/mrm.27721 (2019).

107 Garcia-Garcia, A., Orts-Escolano, S., Oprea, S., Villena-Martinez, V. & Garcia-Rodriguez, J. J. a. p. a. A review on deep learning techniques applied to semantic segmentation. (2017).

108 Pan, S. J., Yang, Q. J. I. T. o. k. & engineering, d. A survey on transfer learning. **22**, 1345-1359 (2009).

109 Russakovsky, O. *et al.* Imagenet large scale visual recognition challenge. **115**, 211-252 (2015).

110 Hochreiter, S. J. I. J. o. U., Fuzziness & Systems, K.-B. The vanishing gradient problem during learning recurrent neural nets and problem solutions. **6**, 107-116 (1998).

111 Philipp, G., Song, D. & Carbonell, J. G. J. a. p. a. The exploding gradient problem demystified-definition, prevalence, impact, origin, tradeoffs, and solutions. (2017).

112   He, K., Zhang, X., Ren, S. & Sun, J. in *Proceedings of the IEEE conference on computer vision and pattern recognition.* 770-778.

113   Shorten, C. & Khoshgoftaar, T. M. J. J. o. b. d. A survey on image data augmentation for deep learning. **6**, 1-48 (2019).

114   Kingma, D. P. & Ba, J. J. a. p. a. Adam: A method for stochastic optimization. (2014).

115   Stanzione, A. *et al.* Detection of Extraprostatic Extension of Cancer on Biparametric MRI Combining Texture Analysis and Machine Learning: Preliminary Results. *Academic radiology* **26**, 1338-1344, doi:10.1016/j.acra.2018.12.025 (2019).

116   Fan, M. *et al.* DCE-MRI texture analysis with tumor subregion partitioning for predicting Ki-67 status of estrogen receptor-positive breast cancers. *Journal of magnetic resonance imaging : JMRI* **48**, 237-247, doi:10.1002/jmri.25921 (2018).

117   Ireland, R. H. *et al.* Feasibility of image registration and intensity-modulated radiotherapy planning with hyperpolarized helium-3 magnetic resonance imaging for non-small-cell lung cancer. *Int J Radiat Oncol Biol Phys* **68**, 273-281, doi:10.1016/j.ijrobp.2006.12.068 (2007).

118   Thomen, R. P. *et al.* Regional ventilation changes in severe asthma after bronchial thermoplasty with (3)He MR imaging and CT. *Radiology* **274**, 250-259, doi:10.1148/radiol.14140080 (2015).

119   Brock, K. K. Results of a multi-institution deformable registration accuracy study (MIDRAS). *Int J Radiat Oncol Biol Phys* **76**, 583-596, doi:10.1016/j.ijrobp.2009.06.031 (2010).

120   Couch, M. J. *et al.* Comparison of functional free-breathing pulmonary 1H and hyperpolarized 129Xe magnetic resonance imaging in pediatric cystic fibrosis. *Academic radiology* **28**, e209-e218 (2021).

121   Giavarina, D. Understanding bland altman analysis. *Biochemia medica* **25**, 141-151 (2015).

122   Zou, K. H. *et al.* Statistical validation of image segmentation quality based on a spatial overlap index1: scientific reports. *Academic radiology* **11**, 178-189 (2004).

123   Farag A, Wang J, Ouriadov A, Parraga G & G., S. Unshielded and asymmetric RF transmit coil for hyperpolarized 129Xe human lung imaging at 3.0 T. *In Proceedings of the 20th Annual Meeting of ISMRM, Melbourne, Australia*, 1233 (2012).

124   Chang, Y. V., Quirk, J. D. & Yablonskiy, D. A. In vivo lung morphometry with accelerated hyperpolarized 3He diffusion MRI: A preliminary study. *Magnetic Resonance in Medicine* **73**, 1609-1614, doi:doi:10.1002/mrm.25284 (2015).

125   Stewart, N. J., Norquay, G., Griffiths, P. D. & Wild, J. M. Feasibility of human lung ventilation imaging using highly polarized naturally abundant xenon and optimized three-dimensional steady-state free precession. *Magn Reson Med* **74**, 346-352, doi:10.1002/mrm.25732 (2015).

126   Caruana, R., Lawrence, S. & Giles, C. Overfitting in neural nets: Backpropagation, conjugate gradient, and early stopping. *Advances in neural information processing systems* **13** (2000).

127   Kirby, M. *et al.* Chronic obstructive pulmonary disease: longitudinal hyperpolarized (3)He MR imaging. *Radiology* **256**, 280-289, doi:10.1148/radiol.10091937 (2010).

Appendices

Appendix A – Feasibility of Dynamic Inhaled Gas MRI-based Measurements using Acceleration Combined with the Stretched Exponential Model

In Appendix A we demonstrated the feasibility of the SEM-based approach using retrospective under-sampling, mimicking AF=10/14 in a small-animal-cohort from the previously reported dynamic-lung studies.

The contents of this appendix have been previously submitted to NMR in Biomedicine and has been resubmitted to Magnetic Resonance Materials in Physics, Biology and Medicine. Tuneesh K Ranota, Matthew S Fox, Tanya Jaiswal, Elise Woodward, Marcus Couch, Tao Li, Iain Ball and Alexei Ouriadov.

"Feasibility of Dynamic Inhaled Gas MRI-based Measurements using Acceleration Combined with the Stretched Exponential Model"

INTRODUCTION

Inhaled gas (^{3}He/^{129}Xe/^{19}F) MRI has been proven to be useful for dynamic lung imaging [1-3]. These techniques enable acquisition of regional fractional-ventilation [4-6] measurements which are very useful as CT-alternatives for detecting gas trapping in lung diseases such as lung inflammation, fibrosis, and COPD [1]. Thus, free-breathing ^{19}F (C_3F_8 or PFP) dynamic lung imaging has been recently demonstrated in human lungs [7]. This wash-out scheme ensures the gradual wash-out ^{19}F gas within the ^{19}F MRI lung images obtained from a COPD patient for eight wash-out breaths [7].

A potential alternative for using hyperpolarized gases for functional lung MR imaging can be seen with thermally polarized fluorinated gas tracers such as sulfur hexafluoride (SF_6), hexafluoroethane (C_6F_6) and perfluoropropane (C_3F_8) [7]. Using fluorinated gases provides multiple advantages such as the ability to be mixed with O_2 to restore initial magnetization (rather than lose it), shortened imaging times, and increasingly

tolerable breath-holds for patients [8]. The feasibility and effectiveness of fluorine-19 (^{19}F) MR imaging of the human lungs has been demonstrated throughout various studies. A study by Pavlova et al. concluded that using a gas mixture of 80% octafluorocyclobutane (OFCB, C_4F_8) and 20% oxygen, they we able to capture ^{19}F lung imaging at low magnetic field strengths and at long imaging times which were tolerable due to the O_2 [9]. In addition, a similar study which used perfluorocyclobutone (PFCB, C_4F_8) as a visualized fluorinated gas, the authors were able to obtain informative (trachea and bronchi) ^{19}F-MRI images of the lungs [10]. This study showed an approach that did not use breath-holding but could still acquire ^{19}F-MRI lung images, which is important for patients with COPD or other pulmonary diseases [10]. Shepelytskyi et al. found that lung images acquired using OFCB showed higher normalized SNR and the SNR of the images were significantly higher compared to PFP, the most common gas agent used in recent preclinical literature [3]. Furthermore, studies have confirmed the feasibility of ^{19}F gas MRI using OFCB as a promising inhalable contrast agent, even at lower magnetic field strengths [9]. Gutberlet et al. used free-breathing dynamic ^{19}F gas MRI to quantify regional lung ventilation in patients with COPD and concluded that it was feasible at 1.5T [7]. Additionally, Maunder et al. demonstrated the benefits of steady-state free precession (SSFP) for ^{19}F C_3F_8 gas at 1.5T, as they were able to produce high quality lung ventilation images [11]. Furthermore, it has been shown that these methods provide decreased scan acquisition times and participant breath-hold duration for ^{19}F-MR imaging of perfluoropropane and using compressed sensing (CS) [12]. Many recent studies have used various fluorinated gases, thus serving as a backbone towards supporting our techniques and methodology to further investigate the usage of fluorine-19 MRI.

In this study, our goal was to apply the SEM combined with CS to the dynamic (^{3}He/^{129}Xe/^{19}F) MRI data previously published for normal rats [6, 13] and investigate the influence of acceleration on the accuracy of the SEM-based regional fractional-ventilation estimates. We investigated the potential of accelerated dynamic SEM-based measurements for three different cases: 1) fully-sampled k-space, 2) 90% retrospectively under-sampled k-space in the wash-in/wash-out direction, (acceleration factor (AF)=10), and 3) 93% retrospectively under-sampled (AF=14) k-space. The sparsity pattern was varied for each k-space in the wash-in/wash-out direction.

In order to generate the SEM-based regional fractional-ventilation maps, we have adapted the SEM equation [8] for fitting dynamic wash-in/wash-out data. We hypothesize that the SEM equation can be adapted for fitting the gas density dependence of the MR signal similar to fitting time or b-value dependences [14, 15].

Finally, we compared the SEM-based fractional-ventilation values we obtained to Deninger's approach-based estimates [4], in order to have independent confirmation of the accuracy of the generated fractional-ventilation estimates.

THEORY

Stretched Exponential Model (SEM):

Each new wash-out breath of air replaces some volume of the inhaled gas in lung, so the signal intensity of the resulting images was gradually attenuated (Figure 1A).
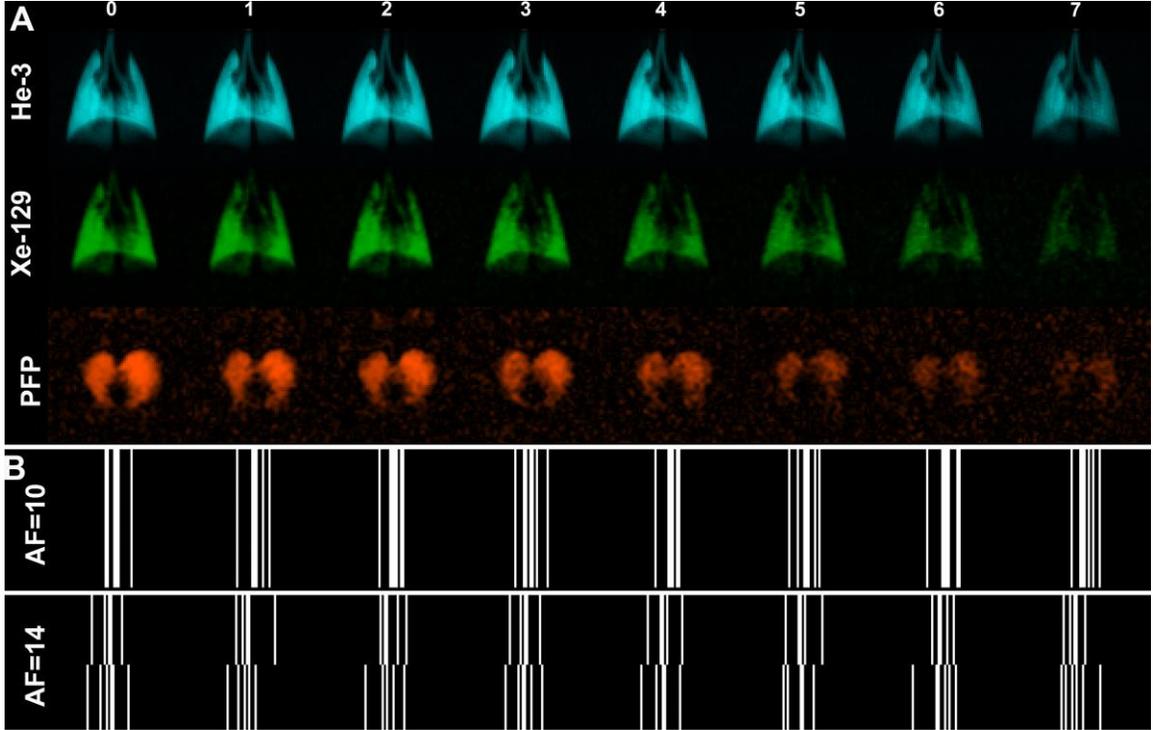
Figure 1. Wash-out ^{3}He/^{129}Xe/^{19}F MRI Images Obtained in Normal Rats.
A) depicts representative eight wash-out images obtained using ^{3}He/^{129}Xe/^{19}F. B) depicts k-space under-sampling schemes, ensuring a variety of sparsity patterns for each wash-out image (AF=10 and AF=14) that were retrospectively applied in wash-out direction.

The following equation can be fitted to the wash-out data when the MR signal does not depend on the flip angle and longitudinal relaxation time:[5]

$$S(n)=S_0(1-r)^n, \tag{1}$$

where S_0 is the initial signal, n is the breath number, $S(n)$ is the signal intensity after the nth wash-out breath and r is the fractional-ventilation parameter $(0<r<1)$.[5,13] r can be expressed as the fraction between fresh gas entering the lung and the total volume of gas within the lung (V_{total}):[5,13]

$$r = V_{new}/V_{total} \text{ or } V_{new}/(V_{new}+V_{old}) \tag{2}$$

The SEM equation can be used for fitting the gas density dependence of the MR signal (Figure 2):

$$S(n)= S_0\exp[-(n\,r'\,)^\beta],\tag{3}$$

where β is heterogeneity index $(0<\beta<1)$, n is the image number and r' is the apparent fractional-ventilation parameter.[8]
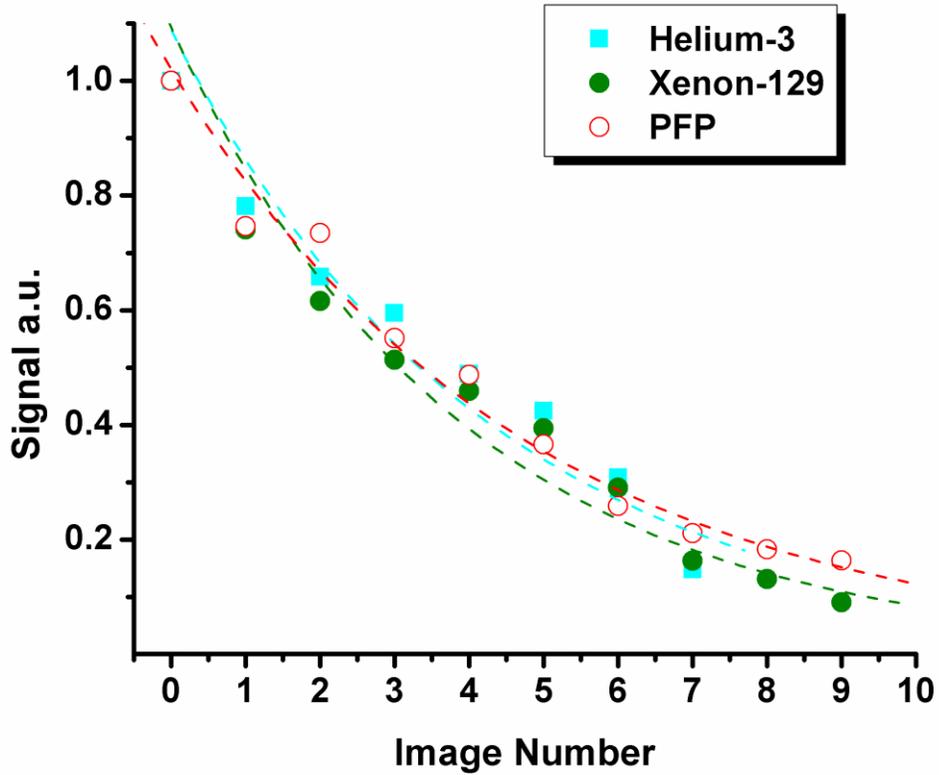
Figure 2. Bulk signal intensity dependence as a function of image number obtained from wash-out rat lung images (Figure 1A). The dashed lines show the best-fit of mono exponentials obtained from Figure 1A.

This interpretation allows us to consider the MR signal intensity variation as reflection of the underlying gas-density variation and hence, reconstruction of the under-sampled k-space using the adapted SEM equation. Lung fractional-ventilation maps can be generated using reconstructed images.

The probability density function (P) can be used to quantify the Gaussian and non-Gaussian distribution of fractional ventilation using the general signal equation:[14,16]

$$S(n) = S_0 \int_0^1 P(r)\exp(-r\cdot\bar{n})\, dr \; ; \tag{4}$$

where $\bar{n}$ is a n-value array, and $S(n)$ is the signal at a particular n (S_0 at $n=0$ and so on). The inverse Laplace transform of $S(n)$ can be used to obtain $P(r)$ for specific analytical representations of the signal attenuation.[14]

For the SEM case, the inverse Laplace transformation of Eqn. [4] yields the probability density function as previously described:[14]

$$P(r) = \frac{B/r'}{(r/r')^{(1-\beta/2)/(1-\beta)}} \exp\left(-\frac{(1-\beta)\beta^{\beta/(1-\beta)}}{(r/r')^{\beta/(1-\beta)}} \right) f(r) \; ; \tag{5}$$

where f(r) is the auxiliary function:

$$f(r) = \begin{cases} 1/[1+C(r/r')^{(0.5\beta-\beta^2/(1-\beta))}], \\ \beta \le 0.5, \\ 1+C(r/r')^{(0.5\beta-\beta^2/(1-\beta))}, \\ \beta > 0.5 \end{cases} \; ; \tag{6}$$

where parameters B and C are functions of α that can be found in previously published work.[14] r' and β maps permit the calculation of $P(r)$ distributions. The probability density function can be used to generate the SEM-based mean fractional-ventilation parameter. Figure 3 shows the probability density functions plotted for three gases.
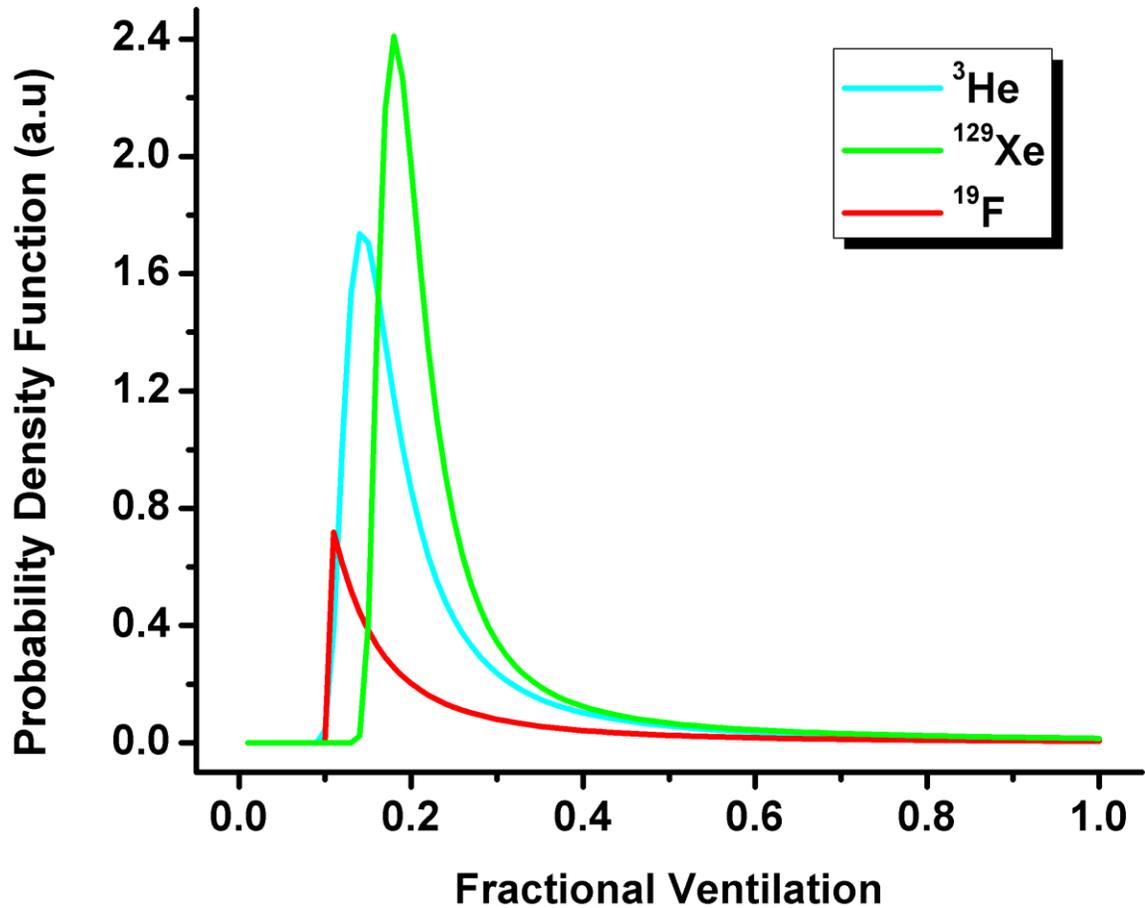
Figure 3. Regional fractional-ventilation distributions obtained for representative animals ventilated with three different gases. Bulk fractional-ventilation distributions obtained for ^{3}He (mean r′ = 0.22, mean β = 0.98, r_{SEM} = 0.26, cyan line), ^{129}Xe (mean r′ = 0.24, mean β = 0.90, r_{SEM} =0.28, dark green line) and ^{19}F (mean r′ = 0.14, mean β = 0.76, r_{SEM} = 0.24, red line) gases from three different animals. The plot shows the smallest r_{SEM} peak value for ^{19}F animal and largest r_{SEM} peak value for ^{129}Xe animal (0.11 vs 0.18 for peak values, respectively). r′ = apparent MRI fractional-ventilation estimate; β = MRI-derived heterogeneity index; r_{SEM} = MRI-derived SEM-based regional fractional-ventilation; SEM = stretched exponential model.

METHODS

Animal Preparation

  All animals were used following specific protocols approved by local ethics.

Sprague-Dawley rats were used for this study and were prepared using methods described

previously [6, 13]. The rats were anesthetized through intravenous administration, intubated with a 5-F polypropylene urinary catheter, and ventilated using a custom pneumatic ventilator suitable for MR imaging of hyperpolarized noble gases. The ventilator allowed for controlled distribution of tidal volumes [13] and a peak inspiratory pressure [5]. A detailed description of the custom ventilator system used has been discussed previously [6].

Hyperpolarized ^{3}He or ^{129}Xe gas was allocated into 300 mL Tedlar plastic bag [5, 6] and implanted into a pressured reservoir [6]. The reservoir maintained a constant pressure of 30 cm H_2O, which allowed inspiratory pressure and tidal volumes of the hyperpolarized gases to be controlled. Flow restrictors accounted for the differences of the two gas types and were determined through a representative rat with bags of (^{4}He/^{129}Xe and O_2 using of 80/20 mixture) [6]. PIPs and tidal volumes were calibrated by manometry and water displacement, respectively. Experiments using the FAVOR technique for MR imaging were repeated three times on three rats to determine measurement precision.

The delivery of inert fluorinated gas/oxygen mixture breath-holds and tidal breathing (3mL based on the average size of rats) with air/oxygen or inert fluorinated gas/oxygen mixture were controlled by the ventilator [13]. Imaging of the lungs were obtained in the beginning of the inert fluorinated gas/oxygen mixture breath-hold interval (time of breath-hold=10sec, pressure =12-15cm H_2O during breath-hold, tidal volume =8mL/kg). A washout breathing scheme was used for ^{19}F imaging and the protocol incorporated rat lungs saturated with an inert fluorinated gas oxygen gas mixture (80/20), for three minutes of continuous breathing at a rate of 60breaths/min [13]. After the three-minute mark, the fluorinated gas/O_2 mixture was stopped and a 10sec breath-hold was

conducted to collect a baseline image. To obtain the second image, we delivered one washout breath of pure O_2 followed by a 10sec breath-hold. This washout breathing technique was repeated nine successive times to ensure complete elimination of fluorinated gas from the rat lungs and to fully sample the washout curve using MR imaging. From the breath-hold durations using the ventilator, data acquisition was gathered. At the end of the experiment, all rats were euthanized through intravenous injection of 340 mg/mL of Euthansol in the tail vein (Schering Inc Canada, Point-Claire QC).

MR imaging

^{3}He, ^{129}Xe and ^{19}F MR imaging were performed using a GE 3T MR750 scanner with a high-performance gradient coil (G=50G/cm, slew rate =2000T/m/s) and the commercial rat-sized ^{3}He (97.3MHz) and ^{129}Xe (35.34MHz) transmit-receive bird-cage coils (Morris Instruments, Ottawa, Canada) as described previously [6]. Using a spin-exchange optical pumping system, ^{3}He has was polarized with a turnkey Helispin system ensuring 40% polarization after 24 hours of polarization process [6]. A Tedlar bag was rinsed three times with medical grade N_2 gas before the transfer of the hyperpolarized ^{3}He and vacuumed (100 mtorr) in order to minimize depolarization of ^{3}He gas due to interactions with paramagnetic O_2. Using a home-build continuous flow polarizer with a gas mixture of 1% Xe, 10% N_2 and 89% ^{4}He, naturally abundant Xe gas (26% ^{129}Xe) was polarized to 15%. ^{129}Xe was put into a Tedlar bag and thawed after cryogenic separation.

A variable flip angle (VFA) fast gradient-recalled echo method with Cartesian sampling was used to produce 2D projection images. The VFA trajectory was calculated following the FAVOR method [5]. 2D projection images were obtained according to the

parameters: FOV = 40x40mm^2, matrix =64x64, producing an in-plane resolution of 0.63mm [6]. Images obtained were whole-lung 2D projections because no slice selection was used. Imaging for ^{3}He used TR=3ms, TE=0.6ms and bandwidth=31kHz, while ^{129}Xe used TR=14ms, TE=2ms and bandwidth=2kHz.[6] To reduce the diffusion-induced signal attenuation caused by imaging gradients and T_2 decay, ^{3}He imaging was completed with a short echo time. The VFA RF pulse trajectory was calculated for each breath (i.e., image), as describe previously [5]. Calibration of the RF pulses occurred through adjustment of the transmitter gain until there was no measurable change in signal over 128 pulses for the entire sample, following a single ^{3}He/^{129}Xe breath. For the calibration of VFA, give to eight breaths of ^{3}He/^{129}Xe were required [6].

The ventilator switched back to air breathing for 2 min after delivering 10 sec anoxic breaths [6], after image acquisition to avoid a significant compromising of the animal's physiology. The FAVOR method was completed four times on each rat using hyperpolarized ^{129}Xe and completed again for ^{3}He. Two fractional ventilation maps were acquired for each coronal and axial plane for each of the gases.

All inert fluorinated gas in vivo measurements were performed using a 3.0T Philips Achieva scanner with maximum gradient strengths of 4G/cm. A home-built rat-sized (9cm inner diameter and 6.8cm length) quadrature transmit/receive coil tuned to the ^{19}F resonance frequency of 120.15MHz was used for multi breath ^{19}F rat lung MR imaging. 2D whole rat lung projection sulfur hexafloride (SF$_6$) and perfluoropropane (PFP, C$_3$F$_8$)) images were obtained in the axial and coronal planes using two-breath acquisitions of 2D x-centric (TE=0.54ms, TR=4ms for SF$_6$, and TR=20ms for PFP, 6x6cm^2, 64x64pixels, Ernst Angle=70^0, BW=400Hz/pixel for SF$_6$, and BW=300Hz/pixel for PFP, 60 averages for SF$_6$

and 12 averages for PFP) [13]. Measurements were performed following the breathing scheme previously describe [13]. Because only half of k-space (50.5% of the readout window) was collected in each of the 9 washout-breaths (as well as for baseline), the entire washout protocol was repeated using the opposite readout gradient polarity in order to create a fully sampled k-space data set for reconstruction [13].

Image processing and analysis

A Hann filter was applied to all ^{19}F k-space data, to maximize the signal-to-noise ratio (SNR) prior to Fourier transformation (IDL 6.4) [18]. A n=0 image was chosen to create a binary mask by using a seeded region-growing algorithm to separate the lungs from the surrounding background and to remove large airways using the custom-built IDL 6.4 algorithm. A binary mask was then applied to the seven remaining ^{3}He/^{129}Xe wash-in images or eleven remaining ^{19}F wash-out images in the series for each animal.

A fitting algorithm from Abascal et. al. [17] (MATLAB R2020a MathWorks, Natick, MA) was used to fit Eqn. [3] to the images as a function of n and to generate r' and β maps on a voxel-by-voxel basis. $P(r)$ distributions were calculated based on Eqns. [5] and [6] with r' and β computed on a voxel-by-voxel basis (MATLAB R2020a).

Two k-space masks mimicking CS-based acceleration were retrospectively applied to the fully-sampled ^{3}He/^{129}Xe/^{19}F k-space data (Figure 1a) in order to obtain under-sampled k-space data with the different AFs. Three cases were explored for two different imaging methods (FGRE (Figure 1b) and X-centric (Figure 1c)): 1) AF=1 or no acceleration, 2) AF=10, 7 k-space lines out of 64 per image using retrospective k-space under-sampling in the imaging direction employing a different under-sampling pattern for each n, and 3)

AF=14, 5 k-space lines out of 64 per image, with retrospective k-space under-sampling as (2). SEM-based full k-space reconstruction using the regularization parameters previously determined [19] and regional fractional-ventilation estimates [20] calculation were done using Abascal's algorithm as previously described [17].

Deninger's approach was used to calculate the ground truth regional fractional-ventilation estimates using Eqn. [1], as previously described [13]. The hyperpolarized gas images were not corrected for the RF pulse history and T_1 decay for simplicity and mimicking a high SNR ^{19}F MRI-based data.

Statistical Analysis

Voxel-by-voxel absolute differences between the regional fractional-ventilation maps generated from the fully sampled and retrospectively under-sampled (AF=10/AF=14) data were quantified using:

$$Absolute\ Difference = \sum_{i=1}^{N}\sum_{j=1}^{M} |[\frac{FullySampled_{ij} - UnderSampled_{ij}}{FullySampled_{ij}}]| \cdot 100\% ; \qquad (7)$$

where N and M are the corresponding image matrix sizes.

Multivariate analysis of variance (ANOVA) using SPSS Statistics, V22.0 (SPSS Inc., Chicago, IL) was performed to compare mean regional fractional-ventilation estimates obtained for the from the fully sampled and retrospectively under-sampled (AF=10/AF=14) data. In all statistical analyses, results were considered significant when the probability of making a Type I error was less than 5% ($P<0.05$).

RESULTS

Accelerated SEM-based dynamic ventilation

Figure 4, 5 and 6 show representative ^{3}He/^{129}Xe/^{19}F MRI-based fractional ventilation maps generated using the Deninger method (^{D}) and the SEM (^{S}) from normal animals using two different imaging approaches (FGRE and X-Centric). The top panel shows fractional ventilation maps calculated for the original fully-sampled k-space. The middle and bottom panels show the maps generated for the retrospectively under-sampled data mimicking AF=10 and 14 correspondently. The mean values of all ^{3}He/^{129}Xe/^{19}F MRI-based fraction ventilation parameters are summarized in Table 1, 2 and 3 correspondently. The spatial distributions of all fraction ventilation parameters for both imaging methods and three acceleration factors were relatively homogeneous for all gases. Mean fractional ventilation values generated for the fully-sampled k-space case using the Deninger method were not significantly different from the other fractional ventilation values generated for the non-accelerated/accelerated data using both Deninger and SEM methods (*P*>0.05 for all cases/gases).
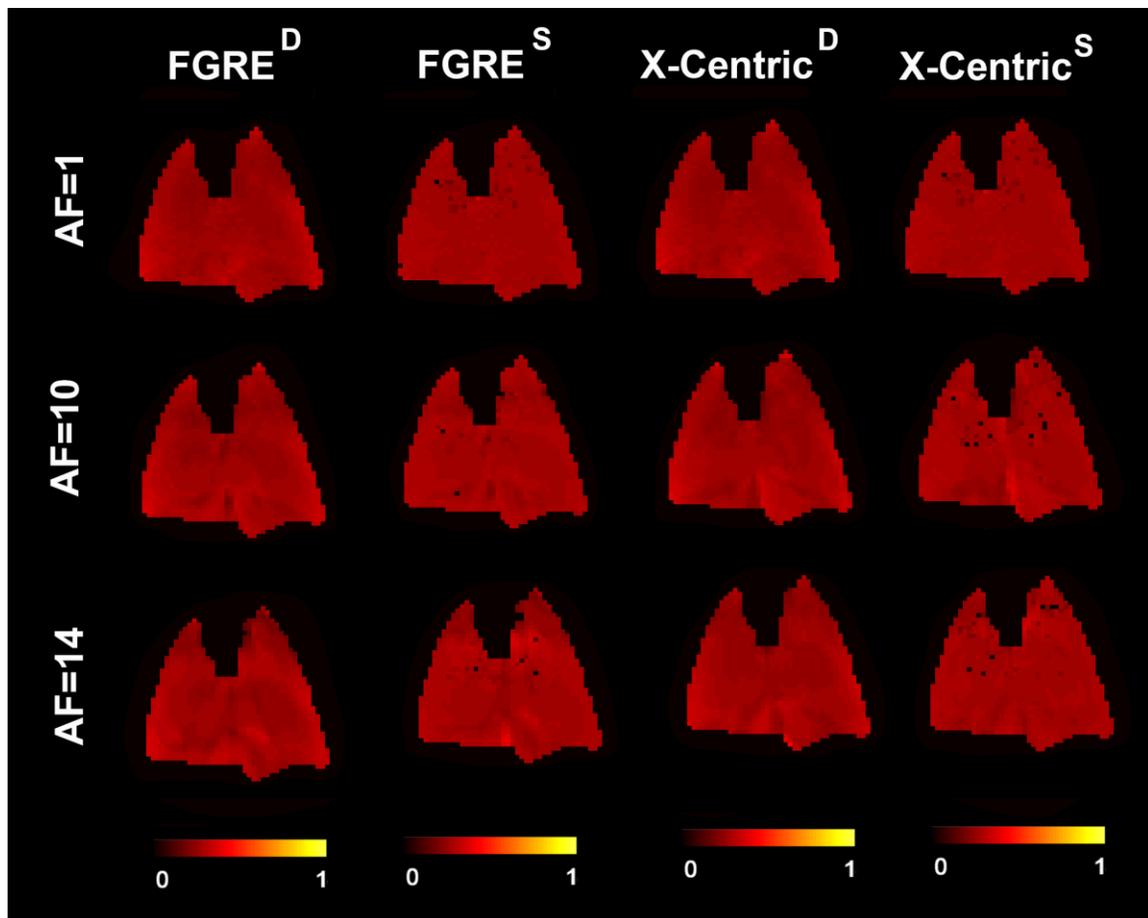
Figure 4. Representative ^{3}He MRI-based fractional ventilation maps generated with using the Deninger method (^{D}) and the SEM (^{S}) from normal animal using two different imaging approaches (FGRE and X-Centric). The top panel shows fractional ventilation maps calculated for the original fully-sampled k-space. The middle and bottom panels show the maps generated for the retrospectively under-sampled data mimicking AF=10 and 14 correspondently.
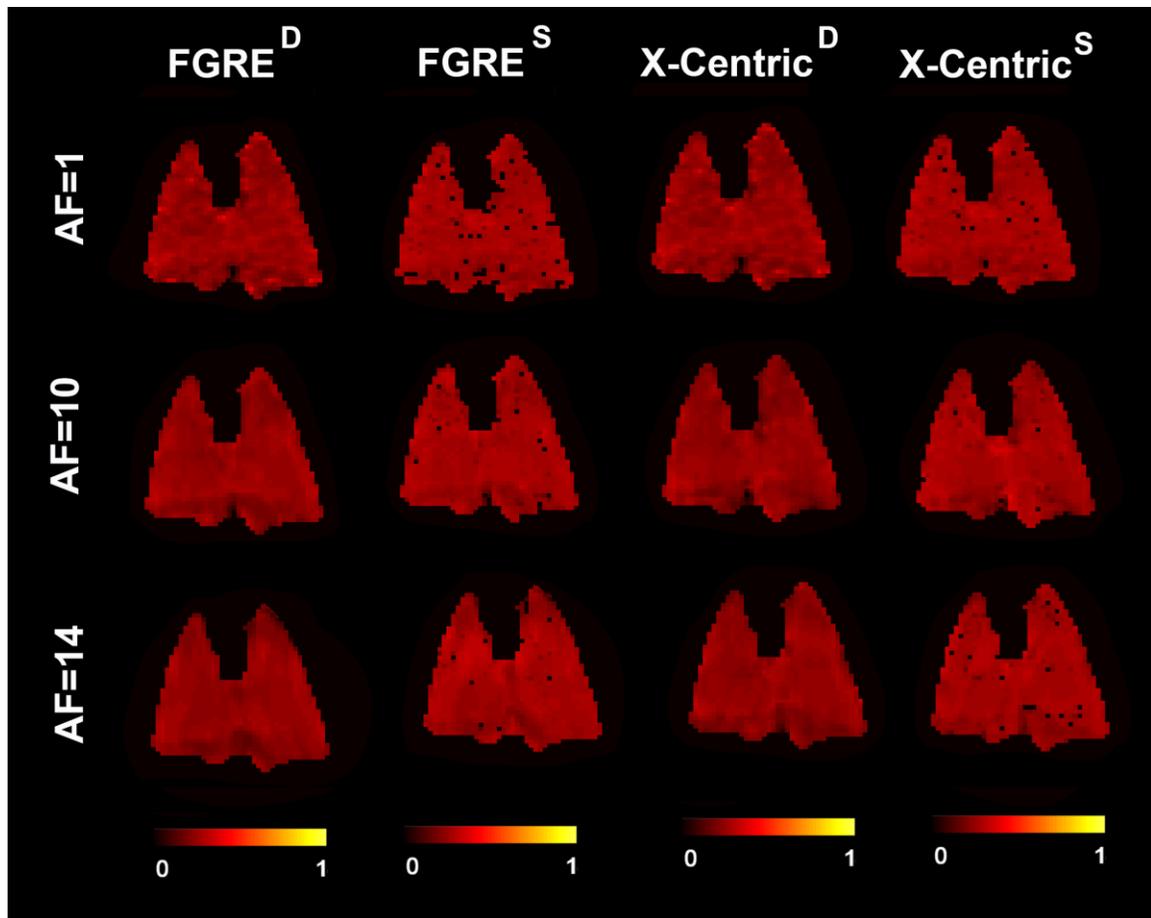
Figure 5. Representative [129]Xe MRI-based fractional ventilation maps generated with using the Deninger method ([D]) and the SEM ([S]) from normal animal using two different imaging approaches (FGRE and X-Centric). The top panel shows fractional ventilation maps calculated for the original fully-sampled k-space. The middle and bottom panels show the maps generated for the retrospectively under-sampled data mimicking AF=10 and 14 correspondently.
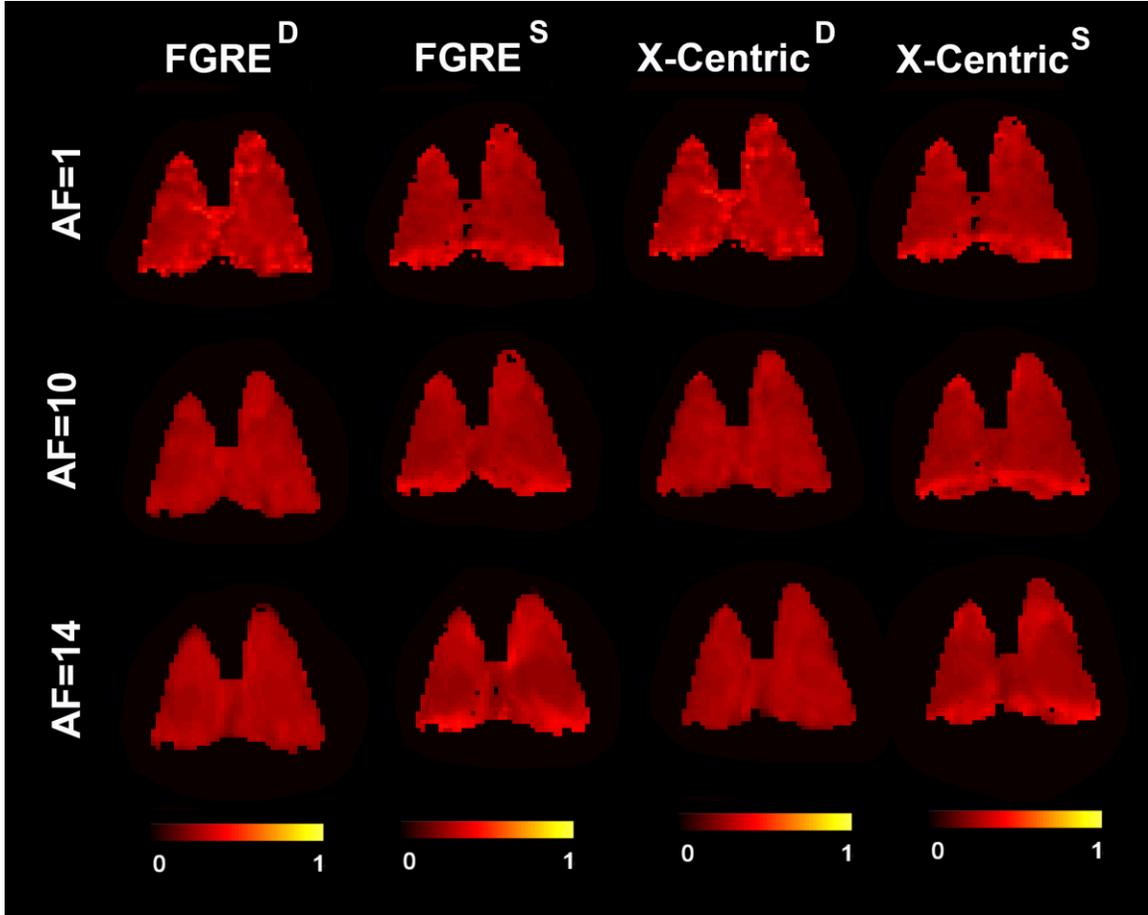
Figure 6. Representative ^{19}F MRI-based fractional ventilation maps generated with using the Deninger method (^{D}) and the SEM (^{S}) from normal animal using two different imaging approaches (FGRE and X-Centric). The top panel shows fractional ventilation maps calculated for the original fully-sampled k-space. The middle and bottom panels show the maps generated for the retrospectively under-sampled data mimicking AF=10 and 14 correspondently.

For the ^{3}He FGRE case the mean absolute differences (Eqn. [7]) of 5.0%/(6.5%) and 5.0%/(7.0%) were observed between AF=1 and AF=10/(AF=14) for the fractional ventilation values calculated with the Deninger method and the estimates calculated with SEM (Table 1). The mean absolute differences of 4.5%/(7.5%) were observed between AF=1 and AF=10/(AF=14) for the fractional ventilation values calculated with the Deninger method for the fully-sampled and under-sampled k-space data (Table 1). The mean absolute differences of 4.0%/(6.0%) were observed between AF=1 and

AF=10/(AF=14) for the fractional ventilation values calculated with SEM for the fully-sampled and under-sampled k-space data (Table 1).

Table 1. ^{3}He MRI-based Fractional-Ventilation Measurements

	FGRE					X-Centric				
	r	r_{sem}	$r - r_{sem}$	$r - r^A$	$r_{sem} - r_{sem}^A$	r	r_{sem}	$r - r_{sem}$	$r - r^A$	$r_{sem} - r_{sem}^A$
AF=1	0.22(.011)	0.20(.006)	5.0%	-	-	0.22(.011)	0.20(.006)	5.0%	-	-
AF=10	0.22(.013)	0.20(.007)	6.5%	4.5%	4.0%	0.22(.013)	0.20(.008)	7.5%	4.5%	4.0%
AF=14	0.22(.013)	0.20(.014)	7.0%	7.5%	6.0%	0.22(.011)	0.20(.007)	8.0%	5.0%	4.0%

r = MRI mean fractional ventilation estimate obtained with the Deninger method using fully-sampled data; r_{sem} = MRI mean fractional ventilation estimate obtained with SEM using fully-sampled data; r^A= MRI mean fractional ventilation estimate obtained with the Deninger method using accelerated data; r_{sem}^A = MRI mean fractional ventilation estimate obtained with SEM using accelerated data; $r - r^A/r - r_{sem}/r_{sem} - r_{sem}^A/$ = pixel-by-pixel deference between the fractional ventilation maps; SEM = stretched exponential model; AF=acceleration factor.

For the ^{3}He X-Centric case the mean absolute differences (Eqn. [7]) of 5.0%/(7.5%) and 5.0%/(8.0%) were observed between AF=1 and AF=10/(AF=14) for the fractional ventilation values calculated with the Deninger method and the estimates calculated with SEM (Table 1). The mean absolute differences of 4.5%/(5.0%) were observed between AF=1 and AF=10/(AF=14) for the fractional ventilation values calculated with the Deninger method for the fully-sampled and under-sampled k-space data (Table 1). The mean absolute differences of 4.0%/(4.0%) were observed between AF=1 and

AF=10/(AF=14) for the fractional ventilation values calculated with SEM for the fully-sampled and under-sampled k-space data (Table 1).

Table 1S shows the ^{3}He MRI-based fractional ventilation values obtained all rats with Deninger method and SEM for three acceleration factors and two sampling schemes (p>0.5 for all cases/gases).

Table 1S. ^{3}He MRI-based Fractional-Ventilation Measurements

FGRE AF10	r	r_{sem}	r^A	r_{sem}^A	$r - r^A$	$r - r_{sem}$	$r_{sem} - r^A$	$r^A - r_{sem}^A$
Rat 1	0.22(.03)	0.21(.01)	0.22(.03)	0.21(.02)	4%	1%	5%	9%
Rat 2	0.23(.02)	0.21(.01)	0.23(.02)	0.21(.01)	4%	6%	4%	6%
Rat 3	0.21(.02)	0.19(.01)	0.21(.03)	0.19(.01)	4%	5%	4%	5%
Rat 4	0.21(.02)	0.19(.01)	0.21(.03)	0.19(.01)	4%	5%	4%	5%
Rat 5	0.21(.03)	0.18(.02)	0.21(.03)	0.18(.02)	5%	7%	6%	8%
FGRE AF14								
Rat 1	0.22(.03)	0.21(.01)	0.22(.03)	0.21(.04)	2%	1%	9%	11%
Rat 2	0.23(.02)	0.21(.01)	0.23(.03)	0.21(.03)	7%	6%	6%	6%
Rat 3	0.21(.02)	0.19(.01)	0.21(.03)	0.19(.03)	7%	6%	7%	6%
Rat 4	0.21(.02)	0.19(.01)	0.21(.03)	0.19(.03)	7%	6%	7%	6%
Rat 5	0.21(.03)	0.18(.02)	0.21(.03)	0.18(.02)	6%	7%	8%	7%
XC AF10								
Rat 1	0.22(.03)	0.21(.01)	0.22(.03)	0.21(.02)	4%	1%	5%	10%
Rat 2	0.23(.02)	0.21(.01)	0.23(.02)	0.21(.02)	6%	6%	4%	7%
Rat 3	0.21(.02)	0.19(.01)	0.21(.03)	0.19(.02)	4%	6%	4%	6%
Rat 4	0.21(.02)	0.19(.01)	0.21(.03)	0.19(.02)	4%	6%	4%	6%
Rat 5	0.21(.03)	0.18(.02)	0.21(.03)	0.18(.01)	3%	7%	5%	8%
XC AF14								
Rat 1	0.22(.03)	0.21(.01)	0.22(.03)	0.21(.02)	3%	1%	5%	10%
Rat 2	0.23(.02)	0.21(.01)	0.23(.02)	0.21(.01)	5%	6%	4%	7%
Rat 3	0.21(.02)	0.19(.01)	0.21(.02)	0.19(.01)	4%	6%	5%	7%
Rat 4	0.21(.02)	0.19(.01)	0.21(.02)	0.19(.01)	4%	6%	5%	7%
Rat 5	0.21(.03)	0.18(.02)	0.21(.03)	0.18(.02)	4%	7%	5%	8%

r = MRI mean fractional ventilation estimate obtained with the Deninger method using fully-sampled data; r_{sem} = MRI mean fractional ventilation estimate obtained with SEM using fully-sampled data; r^A= MRI mean fractional ventilation estimate obtained with the Deninger method using accelerated data; r_{sem}^A = MRI mean fractional ventilation estimate obtained with SEM using accelerated data; $r - r^A/r - r_{sem}/r_{sem} - r^A/ r^A - r_{sem}^A/$ = pixel-by-

pixel deference between the fractional ventilation maps; SEM = stretched exponential model; AF=acceleration factor; FGRE=Fast Gradient Recall Echo; XC=x-Centric.

For the ^{129}Xe FGRE case the mean absolute differences (Eqn. [7]) of 6.5%/(12.0%) and 6.5%/(13.0%) were observed between AF=1 and AF10/(AF=14) for the fractional ventilation values obtained with the Deninger method and the estimates calculated with SEM (Table 2). The mean absolute differences of 7.0%/(10.0%) were observed between AF=1 and AF=10/(AF=14) for the fractional ventilation values obtained using the Deninger method for the fully-sampled and under-sampled k-space data (Table 2). The absolute mean differences of 4.5%/(7.0%) were observed between AF=1 and AF=10/(AF=14) for the fractional ventilation values calculated with SEM for the fully-sampled and under-sampled k-space data (Table 2). Table 1S shows the ^{3}He MRI-based fractional ventilation values obtained with the Deninger method and SEM for three acceleration factors all rats (p>0.5 for all cases/gases).

Table 2. ^{129}Xe MRI-based Fractional-Ventilation Measurements

	FGRE					X-Centric				
	r	r_{sem}	r-r_{sem}	r-r^A	r_{sem}-r_{sem}^A	r	r_{sem}	r-r_{sem}	r-r^A	r_{sem}-r_{sem}^A
AF=1	0.22(.01)	0.22(.01)	6.5%	-	-	0.22(.01)	0.22(.01)	6.4%	-	-
AF=10	0.22(.01)	0.22(.01)	12.0%	7.0%	4.5%	0.21(.01)	0.22(.01)	13%	7.5%	6.0%
AF=14	0.21(.01)	0.22(.01)	13.0%	10.0%	7.0%	0.21(.01)	0.21(.01)	13%	8.0%	5.0%

r = MRI mean fractional ventilation estimate obtained with the Deninger method using fully-sampled data; r_{sem} = MRI mean fractional ventilation estimate obtained with SEM using fully-sampled data; r^A= MRI mean fractional ventilation estimate obtained with the Deninger method using accelerated data; r_{sem}^A = MRI mean fractional ventilation estimate

obtained with SEM using accelerated data; $r - r^A/r - r_{sem}/r_{sem} - r_{sem}^A/ =$ pixel-by-pixel deference between the fractional ventilation maps; SEM = stretched exponential model; AF=acceleration factor.

For the ^{129}Xe X-Centric case, the mean absolute differences (Eqn. [7]) of 6.4%(13%) and 6.4%/(13%) were observed between AF=1 and AF10/(AF=14) for the fractional ventilation values obtained with the Deninger method and the estimates calculated with SEM (Table 2). The mean absolute differences of 7.5%/(8.0%) were observed between AF=1 and AF=10/(AF=14) for the fractional ventilation values calculated using the Deninger method for the fully-sampled and under sampled k-space data (Table 2). The mean absolute differences of 6.0%(5.0%) were observed between AF=1 and AF=10/(AF=14) for the fractional ventilation values calculated with SEM for the fully-sampled and under-sampled k-space data (Table 2). Table 1S shows the ^{3}He MRI-based fractional ventilation values obtained for all rats.

Table 2S shows the ^{129}Xe MRI-based fractional ventilation values obtained all rats with Deninger method and SEM for three acceleration factors and two sampling schemes (p>0.5 for all cases).

Table 2S. ^{129}Xe MRI-based Fractional-Ventilation Measurements

FGRE AF10	r	r_{sem}	r^A	r_{sem}^A	$r - r^A$	$r - r_{sem}$	$r_{sem} - r^A$	$r^A - r_{sem}^A$
Rat 1	0.25(.02)	0.24(.02)	0.24(.02)	0.24(.02)	7%	7%	7%	8%
Rat 2	0.20(.03)	0.21(.03)	0.20(.02)	0.21(.02)	3%	9%	7%	16%
Rat 3	0.21(.04)	0.21(.04)	0.20(.03)	0.21(.03)	4%	9%	8%	14%
Rat 4	0.22(.02)	0.22(.02)	0.22(.02)	0.22(.02)	1%	3%	6%	13%
Rat 5	0.22(.02)	0.22(.02)	0.22(.02)	0.22(.02)	4%	1%	6%	11%
Rat 6	0.22(.02)	0.22(.01)	0.22(.02)	0.22(.02)	7%	8%	7%	12%
Rat 7	0.21(.03)	0.21(.02)	0.21(.02)	0.21(.02)	6%	1%	7%	11%
FGRE AF14								
Rat 1	0.25(.02)	0.24(.02)	0.24(.02)	0.24(.02)	13%	7%	10%	10%
Rat 2	0.20(.03)	0.21(.03)	0.20(.03)	0.21(.03)	6%	10%	9%	17%

	r	r_{sem}	r^A	r_{sem}^A				
Rat 3	0.21(.04)	0.21(.04)	0.20(.03)	0.20(.03)	7%	9%	9%	14%
Rat 4	0.22(.02)	0.22(.02)	0.21(.02)	0.22(.03)	7%	3%	9%	11%
Rat 5	0.22(.02)	0.22(.02)	0.22(.02)	0.22(.03)	1%	.04%	10%	12%
Rat 6	0.22(.02)	0.22(.01)	0.21(.02)	0.22(.02)	8%	6%	10%	13%
Rat 7	0.21(.03)	0.21(.02)	0.20(.03)	0.20(.03)	9%	10%	10%	14%
XC								
AF10								
Rat 1	0.25(.02)	0.24(.02)	0.24(.02)	0.24(.02)	6%	7%	7%	9%
Rat 2	0.20(.03)	0.21(.03)	0.20(.03)	0.21(.03)	5%	9%	8%	17%
Rat 3	0.21(.04)	0.21(.04)	0.20(.03)	0.20(.03)	4%	9%	6%	15%
Rat 4	0.22(.02)	0.22(.02)	0.21(.02)	0.22(.03)	8%	3%	8%	13%
Rat 5	0.22(.02)	0.22(.02)	0.22(.02)	0.22(.03)	5%	.03%	7%	13%
Rat 6	0.22(.02)	0.22(.01)	0.21(.02)	0.22(.02)	4%	6%	7%	12%
Rat 7	0.21(.03)	0.21(.02)	0.20(.03)	0.20(.03)	8%	10%	9%	13%
XC								
AF14								
Rat 1	0.25(.02)	0.24(.02)	0.24(.02)	0.24(.02)	7%	7%	7%	9%
Rat 2	0.20(.03)	0.21(.03)	0.20(.02)	0.20(.02)	4%	9%	9%	16%
Rat 3	0.21(.04)	0.21(.04)	0.20(.03)	0.20(.03)	5%	9%	8%	13%
Rat 4	0.22(.02)	0.22(.02)	0.21(.02)	0.22(.02)	7%	3%	7%	13%
Rat 5	0.22(.02)	0.22(.02)	0.21(.02)	0.21(.02)	.02%	.06%	7%	12%
Rat 6	0.22(.02)	0.22(.01)	0.21(.02)	0.21(.02)	5%	6%	8%	13%
Rat 7	0.21(.03)	0.21(.02)	0.20(.02)	0.20(.02)	7%	10%	9%	13%

r = MRI mean fractional ventilation estimate obtained with the Deninger method using fully-sampled data; r_{sem} = MRI mean fractional ventilation estimate obtained with SEM using fully-sampled data; r^A= MRI mean fractional ventilation estimate obtained with the Deninger method using accelerated data; r_{sem}^A = MRI mean fractional ventilation estimate obtained with SEM using accelerated data; $r - r^A/r - r_{sem}/r_{sem} - r^A/ r^A - r_{sem}^A/$ = pixel-by-pixel deference between the fractional ventilation maps; SEM = stretched exponential model; AF=acceleration factor; FGRE=Fast Gradient Recall Echo; XC=x-Centric.

For the ^{19}F FGRE case the mean absolute differences (Eqn. [7]) of 15%/(16%) and 15%/(10%) were observed between AF=1 and AF=10/(AF=14) for the fractional ventilation values calculated with the Deninger method and the estimates calculated with SEM (Table 3). The mean absolute differences of 12.5%/(14%) were observed between AF=1 and AF=10/(AF=14) for the fractional ventilation values calculate with the Deninger method for the fully-sampled and under-sampled k-space data (Table 3). The mean

absolute differences of 8%(12%) were observed between AF=1 and AF=10/(AF=14) for the fractional ventilation values calculated with SEM for the fully-sampled and under-sampled k-space data (Table 3).

Table 3. ^{19}F MRI-based Fractional-Ventilation Measurements

	FGRE					X-Centric				
	r	r_{sem}	$r-r_{sem}$	$r-r^A$	$r_{sem}-r_{sem}^A$	r	r_{sem}	$r-r_{sem}$	$r-r^A$	$r_{sem}-r_{sem}^A$
AF=1	0.24(.02)	0.24(.04)	15%	-	-	0.24(.02)	0.24(.04)	15%	-	-
AF=10	0.22(.02)	0.22(.04)	16%	12.5%	8%	0.22(.013)	0.20(.008)	12.5%	14.0%	9%
AF=14	0.21(.02)	0.22(.04)	10%	14%	12%	0.22(.011)	0.20(.007)	14.0%	15.0%	9%

r = MRI mean fractional ventilation estimate obtained with the Deninger method using fully-sampled data; r_{sem} = MRI mean fractional ventilation estimate obtained with SEM using fully-sampled data; r^A= MRI mean fractional ventilation estimate obtained with the Deninger method using accelerated data; r_{sem}^A = MRI mean fractional ventilation estimate obtained with SEM using accelerated data; r - r^A/r - r_{sem}/r_{sem} - r_{sem}^A/ = pixel-by-pixel deference between the fractional ventilation maps; SEM = stretched exponential model; AF=acceleration factor.

For the ^{19}F X-Centric case the mean absolute differences (Eqn. [7]) of 15%/(12.5%) and 15%/(14%) were observed between AF=1 and AF=10/(AF=14) for the fractional ventilation values calculated with the Deninger method and the estimates calculated with SEM (Table 3). The mean absolute differences of 14.0%/(15.0%) were observed between AF=1 and AF=10/(AF=14) for the fractional ventilation values calculated with the Deninger method for the fully-sampled and under-sampled k-space data (Table 3). The mean absolute differences of 9%/(9%) were observed between AF=1 and AF=10/(AF=14)

for the fractional ventilation values calculated with SEM for the fully-sampled and under-sampled k-space data (Table 3).

Table 3S shows the ^{19}F MRI-based fractional ventilation values obtained all rats with Deninger method and SEM for three acceleration factors and two sampling schemes ($p>0.5$ for all cases/gases).

Table 3S. [19]F MRI-based Fractional-Ventilation Measurements

FGRE AF10	r	r_{sem}	r^A	r_{sem}^A	$r - r^A$	$r - r_{sem}$	$r_{sem} - r^A$	$r^A - r_{sem}^A$
Rat 1	0.26(.04)	0.25(.09)	0.24(.02)	0.24(.10)	5%	13%	9%	11%
Rat 2	0.26(.05)	0.25(.09)	0.23(.03)	0.24(.06)	18%	16%	14%	15%
Rat 3	0.23(.05)	0.23(.08)	0.21(.04)	0.21(.06)	4%	16%	13%	18%
Rat 4	0.19(.07)	0.20(.09)	0.16(.05)	0.17(.06)	6%	19%	17%	87%
Rat 5	0.07(.05)	0.09(.07)	0.04(.02)	0.03(.02)	36%	15%	38%	50%
Rat 6	0.26(.04)	0.25(.09)	0.24(.02)	0.24(.10)	5%	13%	9%	11%
FGRE AF14								
Rat 1	0.26(.04)	0.25(.09)	0.24(.03)	0.24(.10)	10%	13%	10%	12%
Rat 2	0.26(.05)	0.25(.09)	0.22(.04)	0.24(.09)	21%	16%	16%	13%
Rat 3	0.23(.05)	0.23(.08)	0.20(.04)	0.21(.09)	8%	16%	18%	10%
Rat 4	0.19(.07)	0.20(.09)	0.16(.05)	0.19(.09)	10%	20%	15%	4%
Rat 5	0.07(.05)	0.09(.07)	0.04(.02)	0.02(.02)	35%	9%	20%	135%
Rat 6	0.26(.04)	0.25(.09)	0.24(.03)	0.24(.10)	10%	12%	10%	12%
XC AF10								
Rat 1	0.26(.04)	0.25(.09)	0.24(.02)	0.23(.08)	6%	13%	10%	12%
Rat 2	0.26(.05)	0.25(.09)	0.22(.04)	0.23(.05)	17%	15%	16%	11%
Rat 3	0.23(.05)	0.23(.08)	0.20(.04)	0.21(.07)	7%	16%	16%	17%
Rat 4	0.19(.07)	0.20(.09)	0.15(.05)	0.18(.09)	9%	19%	17%	11%
Rat 5	0.07(.05)	0.09(.07)	0.04(.03)	0.03(.03)	37%	15%	6%	206%

	r	r_sem	r^A	r_{sem}^A				
Rat 6	0.26(.04)	0.25(.09)	0.24(.02)	0.24(.08)	6%	13%	10%	11%
XC								
AF14								
Rat 1	0.26(.04)	0.25(.09)	0.24(.02)	0.24(.08)	7%	13%	11%	13%
Rat 2	0.26(.05)	0.25(.09)	0.22(.04)	0.23(.06)	20%	15%	17%	11%
Rat 3	0.23(.05)	0.23(.08)	0.20(.04)	0.21(.08)	6%	16%	16%	20%
Rat 4	0.19(.07)	0.20(.09)	0.15(.05)	0.18(.10)	5%	19%	18%	14%
Rat 5	0.07(.05)	0.09(.07)	0.04(.03)	0.03(.03)	35%	20%	.06%	133%
Rat 6	0.26(.04)	0.25(.09)	0.24(.02)	0.24(.08)	7%	13%	11%	13%

r = MRI mean fractional ventilation estimate obtained with the Deninger method using fully-sampled data; r_{sem} = MRI mean fractional ventilation estimate obtained with SEM using fully-sampled data; r^A= MRI mean fractional ventilation estimate obtained with the Deninger method using accelerated data; r_{sem}^A = MRI mean fractional ventilation estimate obtained with SEM using accelerated data; $r - r^A/r - r_{sem}/r_{sem} - r^A/ r^A - r_{sem}^A/$ = pixel-by-pixel deference between the fractional ventilation maps; SEM = stretched exponential model; AF=acceleration factor; FGRE=Fast Gradient Recall Echo; XC=x-Centric. Rat 5 had low SNR and demonstrates the worst absolute mean difference between the r values generated from the original data sets and retrospectively under-sampled/reconstructed datasets.

DISCUSSION

In this work we studied the combination of CS with an extended stretched-exponential model (SEM) to analyze dynamic ^{3}He/^{129}Xe/^{19}F images in order to accelerate dynamic ventilation in the rat lung and made a number of important findings including: i) for the first time we demonstrated the feasibility of the inhaled gas SEM-based accelerated dynamic ventilation with AF=10 and 14 in small animals. ii) SEM-based regional fractional ventilation parameters were found to be similar (not significantly different) to those calculated using Eq. [1] or the traditional method iii) to the best of our knowledge

this is the first attempt to generate SEM-based fractional ventilation parameters for three different gases and two different under-sampling patterns (FGRE and X-Centric). iv) no significant difference was found between the fractional ventilation estimates generated from the accelerated full-echo and half-echo imaging methods and therefor, X-Centric can be safely used for dynamic ventilation imaging of the short T_2* gases like SF_6.

To our knowledge, this is the first demonstration of small animal lung fractional ventilation measurements generated using an alternative to the Deninger method. In this study, we demonstrated the feasibility of SEM-based accelerated ^{3}He/^{129}Xe/^{19}F dynamic ventilation measurements with AF=10 and 14 using examples of normal animals. A pixel-by-pixel comparison of the Deninger's approach and SEM-derived fractional-ventilation-estimates obtained for AF=10 and 14 (≤16% difference) has confirmed that even at AF=14 the accuracy of the estimates is high enough to consider this method for prospective measurements. This is a promising result for potential clinical translation of the ^{19}F stretched-exponential model, which is ideally performed in a single breath-hold 3D isotropic voxel multi wash-out breath ^{19}F MRI measurement. Note, that retrospective under-sampling is certainly a limitation of this work, but it is not expected to be a limitation going forward to prospective studies in future keeping in mind that the 3D k-space sampling will require very sensitive RF coils [21-25] to ensure sufficient SNR of the 3D ^{19}F lung images.

The probability density function (Figure 3) was used to generate the SEM-based mean fractional-ventilation parameter. The shape of this function is consistent with the previously published probability density function obtained for the diffusivity distributions [26]. Unsurprisingly, the fractional-ventilation values were similar between Deninger

method based and SEM-based (0.22±.011 vs 0.20±.006; $p>0.05$; ^{3}He, Table 1) similar to the accelerated (x-Centric, AF=14) case (0.22±.011 vs 0.20±.007; $p>0.05$; ^{3}He, Table 1). The overall mean SEM r estimates generated for the ^{19}F MRI lung data were reasonably similar to the previously reported estimates [13].

There are a number of limitations of this work. First of all, the ^{3}He/^{129}Xe MRI wash-in dynamic lung images were considered as the wash-out images and they did not normalize on the RF pulse "history" and oxygen-induced decay, thus the generated fractional ventilation estimates were lower than the previously reported [5, 6]. We tried to mimic the ^{19}F wash-out data using high quality ^{3}He/^{129}Xe dynamic ventilation images to understand how SNR affects the accuracy of the regional estimates (r) and that is why the ^{3}He/^{129}Xe MRI wash-in dynamic lung images were not corrected. Unsurprisingly, the dynamic ^{3}He/^{129}Xe/^{19}F images had a different SNR level, which affected the pixel-by-pixel difference showing the larger difference for the lower SNR images (Table 3). Nevertheless, the lowest SNR (5) for the highest number of wash-out breath was still sufficient to yield reasonable fractional ventilation values. However, we must admit that rat-5 dynamic ventilation images (^{19}F study) had very low SNR and as a result, it is likely the reason for the worst absolute mean difference between the r values generated from the original data sets and retrospectively under-sampled/reconstructed datasets (Table 3S). Tables 1S and 2S show that the high SNR data demonstrates the smallest absolute mean difference (>10% for ^{3}He data and >16% for ^{129}Xe data), while the ^{19}F data had a wide distribution of the absolute mean differences. This is important result showing a limitation of the proposed approach, specifically the SNR limitation.

Secondly, we used normal animals in this work, so the homogeneous distribution of the fractional ventilation estimates across lung was expected. This result is not specific to normal animals as a recent study of the rat models of inflammation and fibrosis disease [1] has suggested that the fractional ventilation maps obtained for the sick animals can be homogeneous as well (Ref 1, Figure 4). We have to admit, that a lack of any animal disease models is a study limitation.

Another important question is an influence of the significant k-space under-sampling on the image resolution. We would like to emphasize that the small number of the acquired k-space lines did not restrict us from the sampling the high frequency line or the edge of k-space, moreover that the sparsity pattern varied from one image to another. The image reconstruction used all acquired dynamic ventilation images and prior knowledge about system through the SEM equation. This approach permitted us to ensure the nominal image resolution and therefore, all generated fractional ventilation maps had the expected nominal resolution as well. The recent resolution phantom study has demonstrated that the significantly accelerated (AF=10 and 14) dynamic ventilation measurement using the CS combined with SEM reconstruction did not lead to the image resolution degradation [27]. It also shown the benefit of the signal averaging when the prior knowledge approach combined with the CS-based reconstruction. Basically, the significant acceleration, normally leading to the image resolution degradation when reconstruct each image independently, was compensated by the large number of wash-out images acquired with varied sparsity pattern used for the group reconstruction powered by the prior knowledge SEM approach.

Finally, Eqn. [3] was not obtained analytically, so an analytical solution may be possible in order to correlate the Deninger method based and SEM-based fractional ventilation estimates.

Imaging strategies using parallel imaging [22] using the phased receive arrays [28] and CS have permitted lung morphometry measurements that overcome the slower diffusion of xenon compared to helium and enable whole lung [129]Xe multi-b diffusion-weighted measurements in a single breath-hold [29-33]. It has been recently shown, that the combination of SEM with CS [17] ([129]Xe clinical study, one healthy subject) permitted under-sampling in both spatial and diffusion-sensitizing directions and therefore, achieving imaging AF=10 while still providing accurate morphometry estimates [34]. Furthermore, the feasibility of SEM-based accelerated [129]Xe morphometry with AF=10 and 14 has been prospectively demonstrated in a small cohort of normal and irradiated rats [29].

In summary, SEM-based dynamic ventilation measurements can be significantly accelerated (up to 14x) without compromising the quality of generated biomarkers such as the fractional ventilation values. Both accelerated and unaccelerated dynamic ventilation (r_{SEM} values) using SEM with ^{19}F MRI in normal rats agree well to previously published fractional ventilation estimates. This suggests that the SEM may be used as an alternative to the Deninger method in cases of the normal animals and potentially for a number of other small animal lung disease models such as inflammation and fibrosis [35]. Finally, CS combined with the SEM permits to significantly accelerate scan time for the [3]He/[129]Xe/^{19}F dynamic ventilation measurements and therefore should be considered for the characterization of lung function, especially in human subjects where breath-hold durations may be limited due to the lung disease including the COVID-19 lung damage

[36]. High quality ^{3}He and ^{129}Xe data suggest that the highly accelerated dynamic

ventilation measurements still ensure the accurate fractional ventilation estimates.

References

1.   Couch MJ, Fox MS, Viel C, Gajawada G, Li T, Ouriadov AV, et al. Fractional ventilation mapping using inert fluorinated gas MRI in rat models of inflammation and fibrosis. NMR Biomed. 2016;29(5):545-52.

2.   Couch MJ, Ouriadov AV, Albert MS. Chapter 18 - Pulmonary Imaging Using 19F MRI of Inert Fluorinated Gases. Hyperpolarized and Inert Gas MRI. Boston: Academic Press; 2017. p. 279-92.

3.   Shepelytskyi Y, Li T, Grynko V, Newman C, Hane FT, Albert MS. Evaluation of fluorine-19 magnetic resonance imaging of the lungs using octafluorocyclobutane in a rat model. Magn Reson Med. 2021;85(2):987-94.

4.   Deninger AJ, Månsson S, Petersson JS, Pettersson G, Magnusson P, Svensson J, et al. Quantitative measurement of regional lung ventilation using 3He MRI. Magnetic Resonance in Medicine. 2002;48(2):223-32.

5.   Santyr GE, Lam WW, Ouriadov A. Rapid and efficient mapping of regional ventilation in the rat lung using hyperpolarized 3He with Flip Angle Variation for Offset of RF and Relaxation (FAVOR). Magn Reson Med. 2008;59(6):1304-10.

6.   Couch MJ, Ouriadov A, Santyr GE. Regional ventilation mapping of the rat lung using hyperpolarized (1)(2)(9)Xe magnetic resonance imaging. Magn Reson Med. 2012;68(5):1623-31.

7.   Gutberlet M, Kaireit TF, Voskrebenzev A, Lasch F, Freise J, Welte T, et al. Free-breathing Dynamic (19)F Gas MR Imaging for Mapping of Regional Lung Ventilation in Patients with COPD. Radiology. 2018;286(3):1040-51.

8.   Fox M, Ouriadov A. High Resolution 3He Pulmonary MRI. In: Manchev APL, editor. Magnetic Resonance Imaging. London, UK: IntechOpen Limited; 2019.

9.   Pavlova OS, Anisimov NV, Gervits LL, Gulyaev MV, Semenova VN, Pirogov YA, et al. (19) F MRI of human lungs at 0.5 Tesla using octafluorocyclobutane. Magn Reson Med. 2020;84(4):2117-23.

10.   Semenova V, Pavlova O, Pirogov Y. Magnetic resonance imaging of lungs using fluorinated gas. Journal of Physics: Conference Series. 2020;1439:012043.

11.   Maunder A, Rao M, Robb F, Wild JM. Optimization of steady-state free precession MRI for lung ventilation imaging with (19) F C3 F8 at 1.5T and 3T. Magn Reson Med. 2019;81(2):1130-42.

12.   Neal MA, Pippard BJ, Hollingsworth KG, Maunder A, Dutta P, Simpson AJ, et al. Optimized and accelerated (19) F-MRI of inhaled perfluoropropane to assess regional pulmonary ventilation. Magn Reson Med. 2019;0(0).

13.   Ouriadov AV, Fox MS, Couch MJ, Li T, Ball IK, Albert MS. In vivo regional ventilation mapping using fluorinated gas MRI with an x-centric FGRE method. Magn Reson Med. 2015;74(2):550-7.

14.   Berberan-Santos MN, Bodunov EN, Valeur B. Mathematical functions for the analysis of luminescence decays with underlying distributions 1. Kohlrausch decay function (stretched exponential). Chemical Physics. 2005;315(1-2):171-82.

15.   Parra-Robles J, Marshall H, Wild JM. Characterization of 3He Diffusion in Lungs using a Stretched Exponential Model [abstract]. ISMRM 21st Annual Meeting. 2013:0820.

16.   Parra-Robles J, Marshall H, Hartley RA, Brightling CE, Wild JM. Quantification of lung microstructure in asthma using a 3He fractional diffusion approach [abstract]. ISMRM 22nd Annual Meeting. 2014:3529.

17.   Abascal J, Desco M, Parra-Robles J. Incorporation of Prior Knowledge of Signal Behavior Into the Reconstruction to Accelerate the Acquisition of Diffusion MRI Data. IEEE Trans Med Imaging. 2018;37(2):547-56.

18.   Fox MS, Ouriadov A, Santyr GE. Comparison of hyperpolarized (3)He and (129)Xe MRI for the measurement of absolute ventilated lung volume in rats. Magn Reson Med. 2014;71(3):1130-6.

19.   Goldstein T, Osher S. The Split Bregman Method for L1-Regularized Problems. SIAM J Imaging Sci. 2009;2(2):323-43.

20.   Fox MS, Woodward E, Couch M, Li T, Ball I, Ouriadov A. Feasibility of the Inhaled Gas MRI-based Dynamic Measurements with Acceleration Factors of 10 and 14 [abstract]. ISMRM 2020 Annual Scientific Meeting Sydney, Australia. 2020:7208

21.   Dregely I, Ruset IC, Wiggins G, Mareyam A, Mugler JP, 3rd, Altes TA, et al. 32-channel phased-array receive with asymmetric birdcage transmit coil for hyperpolarized xenon-129 lung imaging. Magn Reson Med. 2013;70(2):576-83.

22.   Chang YV, Quirk JD, Yablonskiy DA. In vivo lung morphometry with accelerated hyperpolarized 3He diffusion MRI: A preliminary study. Magnetic Resonance in Medicine. 2015;73(4):1609-14.

23.   De Zanche N, Chhina N, Teh K, Randell C, Pruessmann KP, Wild JM. Asymmetric quadrature split birdcage coil for hyperpolarized 3He lung MRI at 1.5T. Magn Reson Med. 2008;60(2):431-8.

24.   Zanette B, Santyr G. Accelerated interleaved spiral-IDEAL imaging of hyperpolarized (129) Xe for parametric gas exchange mapping in humans. Magn Reson Med. 2019;82(3):1113-9.

25.   Doganay O, Thind K, Wade T, Ouriadov A, Santyr GE. Transmit-only/receive-only radiofrequency coil configuration for hyperpolarized129Xe MRI of rat lungs. Concepts in Magnetic Resonance Part B: Magnetic Resonance Engineering. 2015;45(3):115-24.

26.   Ouriadov AV, Fox MS, Lindenmaier AA, Stirrat E, Serrai H, Santyr G. Application of a stretched-exponential model for morphometric analysis of accelerated diffusion-weighted 129Xe MRI of the rat lung. MAGMA. 2021;34(1):73-84.

27.   Perron S, M F, Serrai H, A O, editors. Feasibility of a Novel Sampling/Reconstruction Method Ensuring a SNR Benefit Over the Traditional Sampling Approach. In Proceedings of the 2021 Annual Meeting of ISMRM; 2021; Vancouver, Canada, Online.

28.   Maunder A, Rao M, Robb F, Wild JM. An 8-element Tx/Rx array utilizing MEMS detuning combined with 6 Rx loops for (19) F and (1) H lung imaging at 1.5T. Magn Reson Med. 2020;n/a(n/a).

29.   Ouriadov A, Guo F, McCormack DG, Parraga G. Accelerated 129Xe MRI morphometry of terminal airspace enlargement: Feasibility in volunteers and those with alpha-1 antitrypsin deficiency. Magnetic Resonance in Medicine. 2020;84(1):416-26.

30.   Chan HF, Stewart NJ, Parra-Robles J, Collier GJ, Wild JM. Whole lung morphometry with 3D multiple b-value hyperpolarized gas MRI and compressed sensing. Magn Reson Med. 2017;77(5):1916-25.

31.   Chan HF, Collier GJ, Weatherley ND, Wild JM. Comparison of in vivo lung morphometry models from 3D multiple b-value (3) He and (129) Xe diffusion-weighted MRI. Magn Reson Med. 2019;81(5):2959-71.

32.   Chan HF, Stewart NJ, Norquay G, Collier GJ, Wild JM. 3D diffusion-weighted (129) Xe MRI for whole lung morphometry. Magn Reson Med. 2018;79(6):2986-95.

33.   Zhang H, Xie J, Xiao S, Zhao X, Zhang M, Shi L, et al. Lung morphometry using hyperpolarized (129) Xe multi-b diffusion MRI with compressed sensing in healthy subjects and patients with COPD. Med Phys. 2018;45(7):3097-108.

34.   Ouriadov A, Westcott A, McCormack DG, Parraga G. Feasibility of 129Xe MRI Morphometry Measurements with Acceleration Factors of 7 and 10. ISMRM 27th Annual Meeting, Montreal, Quebec, Canada. 2019([abstract]):3518.

35.   Couch MJ, Ball IK, Li T, Fox MS, Ouriadov AV, Biman B, et al. Inert fluorinated gas MRI: a new pulmonary imaging modality. NMR Biomed. 2014;27(12):1525-34.

36.   Li M, Lei P, Zeng B, Li Z, Yu P, Fan B, et al. Coronavirus Disease (COVID-19): Spectrum of CT Findings and Temporal Progression of the Disease. Acad Radiol. 2020.

Appendix B – Permission for Reproduction of Scientific Articles

June 6, 2022

Alexei Ouriadov
1151 Richmond Street
London
Ontario
Canada N6A 3K7

Dear Alexei Ouriadov:

The Radiological Society of North America (RSNA®) is pleased to grant you permission to reproduce the following figure in print and electronic format for reuse in thesis, provided you give full credit to the authors of the original publication.

Figure 1b 2b
Watz H, Breithecker A, Rau W S, et al. Micro-CT of the Human Lung: Imaging of Alveoli and Virtual Endoscopy of an Alveolar Duct in a Normal Lung and in a Lung with Centrilobular Emphysema—Initial Observations[1]. *Radiology* 2005;236:1053–1058.

This permission is a one-time, non-exclusive grant for English-language use and is exclusively limited to the usage stated and underlined above. The requestor guarantees to reproduce the material as originally published. Permission is granted under the condition that a full credit line is prominently placed (i.e. author name(s), journal name, copyright year, volume #, inclusive pages and copyright holder).

This permission becomes effective upon receipt of this signed contract. Please sign a copy of this agreement, return a signed copy to me and retain a copy for your files. Thank you for your interest in our publication.

[Print Name]:   Alexei Ouriadov

SIGNATURE: _____   Date: June 6, 2022

Sincerely,
LaShundra Carson
Coordinator, Journal Business
Publications

Phone: 630-571-7833
Fax: 630-590-7724
E-mail: *permissions@rsna.org*

Thank you for your order!

Dear Dr. Alexei Ouriadov,
Thank you for placing your order through Copyright Clearance Center's
RightsLink® service.

Order Summary

Licensee:	Dr. Alexei Ouriadov
Order Date:	Jun 5, 2022
Order Number:	5322781213478
Publication:	Academic Radiology
Title:	Hyperpolarized 3He Magnetic Resonance Functional Imaging Semiautomated Segmentation
Type of Use:	reuse in a thesis/dissertation
Order Total:	0.00 CAD

View or print complete details of your order and the publisher's terms and
conditions.

Sincerely,

Copyright Clearance Center

CCC   RightsLink®

SPRINGER NATURE

Thank you for your order!

Dear Dr. Alexei Ouriadov,
Thank you for placing your order through Copyright Clearance Center's
RightsLink® service.

Order Summary

Licensee:	Dr. Alexei Ouriadov
Order Date:	Jun 5, 2022
Order Number:	5322781472444
Publication:	Springer eBook
Title:	U-Net: Convolutional Networks for Biomedical Image Segmentation
Type of Use:	Thesis/Dissertation
Order Total:	0.00 CAD

View or print complete details of your order and the publisher's terms and
conditions.

Sincerely,

Copyright Clearance Center

CCC   RightsLink®

SPRINGER NATURE

Thank you for your order!

Dear Dr. Alexei Ouriadov,
Thank you for placing your order through Copyright Clearance Center's
RightsLink® service.

Order Summary

Licensee:	Dr. Alexei Ouriadov
Order Date:	Jun 5, 2022
Order Number:	5322790129007
Publication:	Springer eBook
Title:	UNet : A Nested U-Net Architecture for Medical Image Segmentation
Type of Use:	Thesis/Dissertation
Order Total:	0.00 CAD

View or print complete details of your order and the publisher's terms and
conditions.

Sincerely,

Copyright Clearance Center

CCC RightsLink®

Appendix C – Curriculum Vitae

Tuneesh Kaur Ranota
June 2022

Education

2020-Present	Master of Engineering Science, Biomedical Engineering *The University of Western Ontario, London, Ontario, Canada*
2016-2020	Bachelors of Science, Honours Life Sciences *McMaster University, Hamilton, Ontario, Canada*

Training

2020   **3T MRI Safety Training**
Completed under the supervision of Mr. Dave Reese

2021   **Semi-Automated VDP Calculation Training**
Completed under the supervision of Dr. Grace Parraga

Presentations (5):

1. **Ranota T**, Guo F, Wu T, Fox M, McCormack D, Parraga G and Ouriadov A. Automatic Quantification of Ventilation Defects in 3D isotropic ^{129}Xe MRI in COVID-19 Survivors. International Society of Magnetic Resonance in Medicine. May 2022. London, England, United Kingdom. Presented virtually.
2. **Ranota T**, Guo F, Wu T, Fox M, McCormack D, Parraga G and Ouriadov A. The Use of 3D Hyperpolarized ^{129}Xe Lung MRI for Deep-Learning-Based Automated Quantification of Ventilation Defects and Heterogeneity. Imaging Network Ontario Symposium. March 2022. Virtual.
3. **Ranota T**, Serrai H, Parraga G, McCormack D, and Ouriadov A. The Use of Hyper-Polarized ^{129}Xe Pulmonary MRI for Study of the Lung Damage in COVID-19 Survivors, Preliminary Results. American Thoracic Society International Conference. May 2021. Virtual.
4. **Ranota T**, Serrai H, Parraga G, McCormack D, and Ouriadov A. Feasibility of Single Breath-hold Isotropic Voxel ^{129}Xe MRI in COVID-19 Survivors using a Key-Hole Method. International Society of Magnetic Resonance in Medicine. May 2021. Vancouver, BC, Canada. Presented virtually.
5. **Ranota T**, Serrai H, Parraga G, McCormack D, and Ouriadov A. The Feasibility of Hyperpolarized ^{129}Xe MRI for lung damage in COVID-19 Survivors using a Key-Hole Method. Imaging Network Ontario Symposium. March 2021. Virtual.

Publications

1. **Ranota TK,** MS Fox, T Jaiswal, E Woodward, M Couch, T Li, I Ball, A Ouriadov. *Feasibility of Dynamic Inhaled Gas MRI-based Measurements using Acceleration Combined with the Stretched Exponential Model. Submitted to MAGMA, 2022.*

1. **Ranota TK**, F Guo, R Babaeipour, T Wu, MS Fox, DG McCormack, G Parraga, and A Ouriadov. The Use of 3D Isotropic Hyperpolarized 129Xe Lung MRI for Deep-Learning-Based Automated Quantification of Ventilation Defects and Heterogeneity. *Submitted to JMRI, 2022.*

Professional Societies

2020-Present	American Thoracic Society International Conference *Student Member*
2020- Present	Imaging Network Ontario Symposium *Student Member*
2020- Present	International Society of Magnetic Resonance in Medicine *Student Member*

Honours and Awards

2022	International Society of Magnetic Resonance in Medicine *Educational Stipend $475 USD*
2021	International Society of Magnetic Resonance in Medicine *Educational Stipend $250 USD*
2021	Imaging Network Ontario Symposium *First Place Pitch Presentation Award in the Contrast Agents II Session*
2020-2022	Western Graduate Research Scholarship *Department of Biomedical Engineering, Western University* *$1,700 per term*
2016-2020	McMaster University General Bursary *$1000 CAD Scholarship per year*
2016	Roy Foss Leadership Award *$250 CAD Scholarship*